Low-Threshold Indium Gallium Nitride Quantum Dot Microcavity Lasers

Dissertation Advisor: Evelyn Hu Alexander J. Woolf

Low-threshold indium gallium nitride quantum dot microcavity lasers

Abstract

Gallium nitride (GaN) microcavities with embedded optical emitters have long been sought after as visible light sources as well as platforms for cavity quantum electrodynamics (cavity QED) experiments. Specifically, materials containing indium gallium nitride (InGaN) quantum dots (QDs) offer an outstanding platform to study light matter interactions and realize practical devices, such as on-chip light emitting diodes and nanolasers. Inherent advantages of nitride-based microcavities include low surface recombination velocities, enhanced room-temperature performance (due to their high exciton binding energy, as high as 67 meV for InGaN QDs), and emission wavelengths in the blue region of the visible spectrum. In spite of these advantages, several challenges must be overcome in order to capitalize on the potential of this material system. Such difficulties include the processing of GaN into high-quality devices due to the chemical inertness of the material, low material quality as a result of strain-induced defects, reduced carrier recombination efficiencies due to internal fields, and a lack of characterization of the InGaN QDs themselves due to the difficulty of their growth and therefore lack of development relative to other semiconductor QDs. In this thesis we seek to understand

and address such issues by investigating the interaction of light coupled to InGaN QDs via a GaN microcavity resonator. Such coupling led us to the demonstration of the first InGaN QD microcavity laser, whose performance offers insights into the properties and current limitations of the nitride materials and their emitters.

This work is organized into three main sections. Part I outlines the key advantages and challenges regarding indium gallium nitride (InGaN) emitters embedded within gallium nitride (GaN) optical microcavities. Previous work is also discussed which establishes context for the work presented here. Part II includes the fundamentals related to laser operation, including the derivation and analysis of the laser rate equations. A thorough examination of the rate equations serves as a natural motivation for QDs and high-quality factor low-modal volume resonators as an optimal laser gain medium and cavity, respectively. The combination of the two theoretically yields the most efficient semiconductor laser device possible. Part III describes in detail the design, growth, fabrication and characterization of the first InGaN QD microcavity laser. Additional experiments are also conducted in order to conclusively prove that the InGaN QDs serve as the gain medium and facilitate laser oscillation within the microdisk cavities. Part III continues with work related towards the development of the next generation of nitride light emitting devices. This includes the realization of photonic crystal cavity (PCC) fragmented quantum well (FQW) lasers that exhibit record low lasing thresholds of 9.1 $\mu J/cm^2$, comparable to the best devices in other III-V material systems. Part III also discusses cavity QED experiments on InGaN QDs embedded within GaN PCCs in order to quantify the degree of light-matter interaction. The lack of experimental evidence for weak or strong coupling, in the form of the Purcell Effect or cavity-mode anti-crossing respectively, naturally motivates the question of what mechanism is limiting the device

performance. Part III concludes with cathodoluminesence and tapered fiber measurements in order to identify the limiting factor towards achieving strong coupling between InGaN QDs and GaN microcavities.

Contents

List of Figures

Acknowledgements

I always envisioned that upon completing the text of my thesis and finally having the opportunity to thank those who made it possible, I would feel emotions of satisfaction and relief. Instead, I must admit that I feel sadness. The primary reason is that my time working with Professor Evelyn Hu is approaching its end. It is Evelyn who I would like to first acknowledge, for without her none of the work presented here would have come to fruition. I could easily write a text equal in length to the entirety of the work presented below, describing why I feel such respect and admiration for Evelyn, however instead I will offer a few vignettes. Those not acquainted with Evelyn may recognize her for her numerous scientific achievements and accolades. In addition to her success as a scientist and mentor, it is her warmth and kindness that I cherish above all else. Graduate school can be a daunting and lonely experience at times, yet Evelyn's numerous acts of friendship such as cakes and songs for every birthday have made the lab feel like a second home. Scientifically, she resembled a magician at times, seemingly pulling solutions to arduous problems out of thin air. I would like to clarify that when I directly acknowledge her as leading the Harvard team below, that was in an active rather than passive role. She was truly in the trenches throughout the entirety of this work and was critical in identifying many of the key insights described below. She has served as my mentor for more than seven years, beginning with my time as an undergraduate at UC Santa Barbara. Since then, I have grown from a young man to a man and my hope going forward is that I will emulate her qualities of professionalism, empathy and passion for life throughout my own career and interaction with others.

The next person I would like to acknowledge is Professor Federico Capasso. While I have chosen not to discuss the work I conducted in his lab in this thesis, it was a joy and an honor to be an adjunct Capasso group member. If Evelyn is the magician, then Federico is the juggler, effortlessly balancing a multitude of projects across tenuously related fields. I can't count the number of times just a quick conversation with Federico would leave me thinking, "Why didn't I think of that!" His enthusiasm for science and chocolate is infectious. One can't help smiling in the presence of Federico, as a heated scientific discussion will turn to laughter in a matter of moments. I would like to thank him for encouraging me to conduct seemingly impossible experiments in his lab while spending a small fortune in the process.

Just as two paths of light combine together to form an interferogram, my joint experiences in the Hu and Capasso lab have offered me a unique and holistic perspective of how science is practiced. I would like to thank them once again for their mentorship and friendship.

The contribution of many others was essential to this work. All of the material fabricated and measured in this work was grown in Professor Rachel Oliver's lab at the University of Cambridge. Dr. Tongtong Zhu and Dr. Menno Kappers spent countless days and sleepless nights working hard to realize the best material possible. Rachel's command of the GaN material system was pivotal towards the results and insights provided below. I had the great fortune to work directly with Tim Puchtler from Prof. Oliver's lab. Over the course of the two trips he made to Cambridge, we fabricated and measured a multitude samples. We also spent a lot of time scratching our heads and conversing about life and science, especially during the impromptu drive to New Hampshire to replace a broken cryostat window. Not many people have experienced

standing in a dark room and shouting power meter readings and CCD intensity counts from micron-sized lasers, back and forth, for hours on end. I wouldn't have wanted to share that experience with anyone else but Tim. I also greatly enjoyed my time with Dr. Haitham El-Ella during his visit to Harvard. Although we did not directly work together, he was gracious enough to spend a lot of time explaining the intricacies of GaN to me.

Hu Group postdocs Dr. Kasey Russell and Dr. Igor Aharonovich were indispensable to me, and I would like to thank them for their patience and willingness to field any question I had. They are both work horses in the lab and served as excellent examples of how to succeed in science. I would also like to thank the following Hu group members who I directly worked including: Danqing Wang, Nan Niu, Dr. Fabian Rol, Dr. Tsung-li Liu, Dr. Johnathon Lee, Dr. John Joo, David Bracher and Xingyu Zhang. Thank you as well to all the other Hu group members, both past and present whom I was able to spend my time in the lab with. We bonded as a family would over the years and I will cherish the friendships I have made with all of you.

I would like to acknowledge Capasso lab members Profesor Alejandro Rodriguez, Dr. David Woolf and Lulu Liu with whom I collaborated on the optical force experiments with. It was a pleasure to build the optical force setup from scratch with Lulu while refining our 90's alternative playlist to somewhat of an art form. Lulu was my partner in crime against the likes of Alex Bubko and the sales technician who quoted us a thickness in units of grams of gold per 1000 square sheets. I thoroughly enjoyed discussing science and life both in the lab and at lunch with Dr. Mikhail Kats, Dr. Patrice Genevet, Tony Mansuripur, Dr. Stefan Kalchmair, Balthasar Mueller, and Daniel Wintz. I loved debating the fundamentals of lasers operation with hard core QCL laser dudes Toby and Stefan. Lengthy discussions with both of them greatly assisted me in interpreting my lasing measurements.

I would like to thank Professor Marko Loncar for serving on my qualifying and defense committeeS as well as his lab for loaning me equipment, all of which I promise I have returned.

I had the honor of mentoring high school students Richard Cheng, Eric Roxlo and Philip Frick, In addition to undergraduates Jon Snyder and Aun Zaidi. I feel I learned more from each of them than vice versa and I would like to acknowledge all of their hard work and general enthusiasm in the lab.

I must mention my graduate student drinking buddies including: Daniel, Oliver Hauser, Toby, Balthasar, Ben Franta, Michael Burek, Haig Atikian, Jess Crossno and Dogus Cubuk. They provided much a needed outlet to bemoan arduous experiments and kept me sane throughout grad school.

Thank you to my parents Jim and Laurel Woolf, who have encouraged and supported me both emotionally and financially every step of the way. The combination of laughter and face palms in their presence has always brought me great joy. I love you both very much. I would also like to acknowledge my other immediate family members including my sister Julia and brothers Anthony and his wife Rhonda, David and his wife Monica, and Donald as well as their respective families. Finally, thank you to my grandparents David and Evelyn Kunz who have been married for more than 68 years and instilled a love of learning and compassion to others within me.

My last acknowledgment is to my wife Sylvie. No one has sacrificed more throughout this entire process then her. Thank you for moving to Boston, persevering four winters as well as the roller coaster ride of schedules and emotions. I consider this work equal part hers because none of it would have been possible without her support. For these reasons and many more it is her I dedicate this work to. I love you.

For my wife Sylvie. We did it!

Chapter 1

Introduction

1.1 Overview

Next generation technology requires next generation materials and devices. Much like past innovations that led to the stone age, bronze age, iron age, etc., the invention of the transistor in 1947 followed by the integrated circuit in 1958 has led to a "silicon age" which has reaped innumerable benefits for mankind. At some point, however, mankind's imagination outpaces his or her tools and new technological innovations are required. We are quickly approaching the limit of silicon's capabilities. While Moore's law (the fact that the number of transistors in a dense integrated circuit doubles approximately every 2 years) [26] has held since 1958, exponential growth is unsustainable [27]. There are disputes as to when Moore's law will end, with one highly cited report from Intel predicting that at current rates the trend will continue until 2029, at which point a new computing architecture will be necessary to realize further advancements in processing power [28]. Solid state quantum computers offer one potential solution but in order to realize such a device, a quantum bit (or qubit) must be optically addressed in order to

read, write and manipulate the quantum state. Furthermore, one additional requirement is that the qubit design must be scalable. This necessitates devices of small sizes. Achieving light-matter interaction within nanoscale systems is therefore critical towards realizing a quantum computer.

Similarly, lighting technology such as incandescence bulbs, have fundamental energy consumption constraints, as they operate on the principle of blackbody emission. The tungsten wire has to reach a critical temperature in order to emit appreciable amounts of visible light. It takes a certain amount of energy to heat the device to this temperature. Even CFL bulbs have minimum energy consumption requirements as a certain amount of electrical current is required to stimulate light emission from the argon and mercury gases inside. Lighting currently consumes twelve percent of our electrical consumption in the United States and the worldwide demand will only increase as the standard of living in emergeng economies progresses [29]. A new lighting architecture is therefore necessary and in fact well underway in the form of GaN light emitting diodes (LEDs). However, there are still many open questions regarding the materials that make up LEDs. How are the devices, which are riddled with dislocations and impurities, so efficient? How can we overcome "droop," an observed decrease in LED efficiency as injection currents are increased? Fundamental studies of the light emitters themselves are necessary to answer such questions.

Even lasers, which falsely seem like a rarely used technology, must evolve in the near future to prevent a bottleneck in computing power. As the number of processors increases, so does the data transfer rates. This in turn leads to deleterious heating of electrical circuits, compromising computing performance. The replacement of electrical circuits with optical circuits offers one solution to this problem, due to the high bandwidth and low power consumption of optical waveguides. However, a coherent source

is required to generate the light that propagates in such waveguides. Tabletop or even millimeter-sized conventional lasers will not be sufficient, due to the lack of on-chip scalability. Therefore, new laser sources which are on the micrometer or even nanometer scale are necessary.

Gallium nitride (GaN) and its alloy, indium gallium nitride (InGaN), has the potential to address all of these technological bottlenecks. The material's efficient emission of light spanning the visible spectrum in conjunction with its enhanced room temperature performance, compared to other semiconductor materials, make it an ideal candidate for next-generation devices. But, as with the development of any new technology, there are challenges towards realizing such devices. As we will see in Parts I and II the motivations or *why*, is often readily apparent from GaN's material properties, however the *how* is often obfuscated. This thesis is a work of *how.* How do we get an artificial atom in the form of a quantum dot to interact with a photon? How can we use this interaction to learn about the properties of the material itself? How do we make a nanoscale light source that consumes low amounts of power?

1.2 Methodology

The approach we have taken in this work is to fabricate nanoscale GaN optical cavities with embedded indium gallium nitride (InGaN) QDs. This system serves as an ideal platform for the study of light-matter interactions and allows for the realization of efficient laser devices. This work offers a significant advancement for the GaN-based materials, as it demonstrates that the performance of GaN lasers is now comparable to the best arsenide or phosphide devices. This thesis also emphasizes that while lasers are one potential application of this work, they are by no means the only ultimate goal. In

fact, novel light emitters such as exciton-polariton lasers offer the potential for coherent light emission *without* the requirement of carrier inversion. Exciton-polartion lasers may well replace conventional diode lasers; however in order to realize such devices significant light-matter interaction between the exciton and cavity mode is necessary. To date, polariton lasing has not been observed in GaN-based microcavities, such as microdisks or photonic crystal cavities. However, this work serves as a critical stepping stone towards the realization of such next generation technology. In fact, in the investigation of our laser devices we have identified a new gain material known as a fragmented quantum well (FQW). FQW is a type of hybrid between a quantum dot and a quantum well and offers advantages over both, such as enhanced carrier capture cross section and carrier confinement.

Interestingly, the *hows* of this work have led back to questions of *why.* Why does a microcavity that appears flawless still have lower photon lifetimes when compared to similar arsenides or phosphide devices? Why don't we see evidence of weak or strong coupling in cavity quantum electrodynamics experiments? We provide experiments that suggest possible answers to these questions, which should serve as the foundation towards the next generation of GaN-based microcavity devices.

Part I

InGaN QDs in GaN microcavities

Chapter 2

Microcavities with embedded indium gallium nitride emitters (motivation and previous work)

2.1 Introduction

In this chapter we discuss key advantages and challenges regarding indium gallium nitride (InGaN) emitters embedded within gallium nitride (GaN) optical microcavities. In short, the main advantage of InGaN emitters relate to the materials' wide bandgap (up to 3.4eV) and high exciton binding energy (up to 67 meV for non-polar InGaN QDs), which allow for light emission across the entire visible spectrum as well as enhanced room temperature performance compared to other III-V emitters [30]. The challenges regarding nitride microcavities are vast and often not well defined or understood. A few specific challenges include the lack of a wet chemical undercut for device processing due the inertness of the nitrides, and the lack of controlled and reproducible means of QD

formation. This makes the emitters more difficult to grow than in other III-V materials [31, 32]. A major focus of the work presented in this thesis is identifying and overcoming such challenges. The chapter concludes with work conducted before the onset of this thesis in order to highlight specific milestones in the field while providing a broader context for the work presented in the next chapter. There are many excellent recourses available regarding photonic microcavites and the nitride family of emitters highlighted in this chapter. Specific works include Dr. R. Johne's PhD thesis (Universite Blaise Pascal, 2009)[33], Dr. Haitham El-Ella's PhD thesis (Cambridge University, 2012)[2], Dr. Anas Jarjour's PhD thesis (Oxford University, 2007)[34], Dr. Kevin Hennesey's PhD thesis (UCSB, 2006)[7], and *Microcavities* by Dr. Alexey Kavokin et al.[5], among others.

2.2 Advantages of InGaN emitters embedded within GaN

2.2.1 Light emitting diodes and lasers

The advantages of InGaN-based light emitting devices compared to other semiconductor materials is readily apparent in a few simple plots. Figure 2.1 is one such graph, showing the band gap and corresponding wavelength of emission for a variety of semiconductors.

In Figure 2.1 we see that $In_xGa_{1-x}N$ is the only ternary alloy with a band gap spanning the entire visible spectrum (as the indium composition is varied from zero to one). This is, in large part, because the lattice constant varies between 0.319 nm and 0.353 nm for GaN an InN, respectively. These values of the $In_xGa_{1-x}N$ lattice constant are considerably smaller than other III-V materials, excluding $Al_{1-x}Ga_xN$[35].

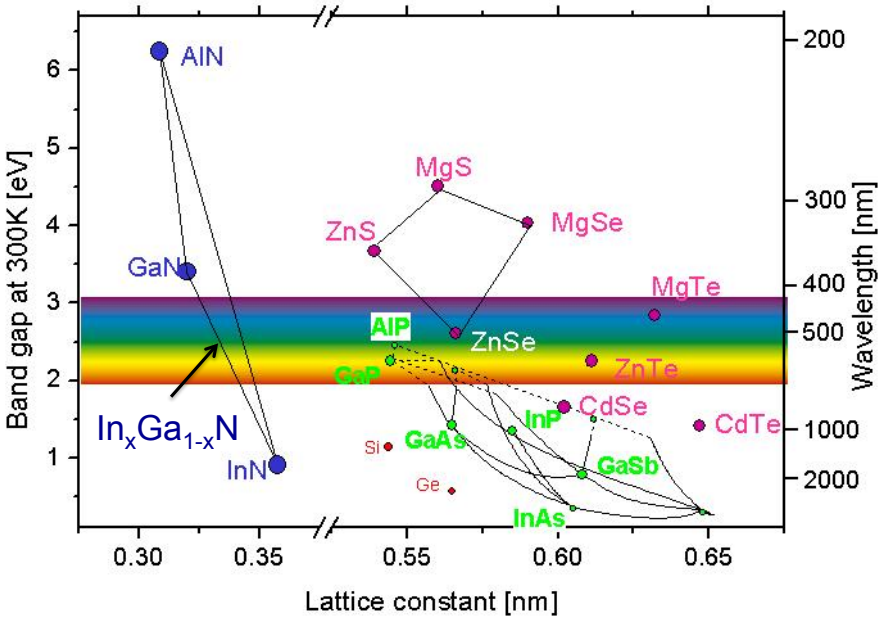

FIGURE 2.1: Graph of the band gap and wavelength of various material systems at 300K versus lattice constant, adapted from[1]. $In_xGa_{1-x}N$ is the only alloy that covers the whole visible spectrum as x varies from zero to one.

All of the experiments conducted in this work were done using c-plane in the Wurzite phase, shown in Figure 2.2a. Furthermore, Figure 2.2b illustrates that the band structure of the GaN possesses a direct band gap in the Γ valley, which makes it an inherently efficient light emitter, compared to indirect band gap semiconductors like silicon.

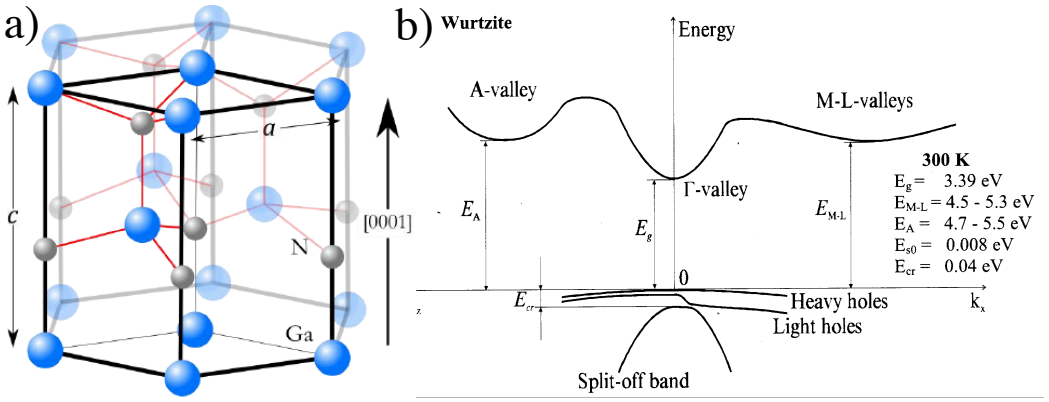

FIGURE 2.2: a) Wurzite phase GaN where the c plane is perpendicular to the [0001] direction, from [2]. b) Bandstructure of GaN which shows the presence of a direct band gap at the Γ valley [3].

From a device perspective, the possibility of a single semiconductor platform emitting light at any wavelength in the visible spectrum is exhilarating. One report outlines

the specific advantages of GaN-based LEDs as the following, "They contain no harmful substances, consume less energy and, with a lifetime of between 15,000 and 30,000 hours, last longer than conventional light sources. They also work at full brightness as soon as you flick the switch." [36] Due to the enormous potential of GaN as a light source, GaN-based LEDs emitting in the blue were demonstrated immediately following the first demonstration of a high-quality GaN film with output powers 10 times greater than SiC based blue LEDs [37, 38]. Advancement of the material since 1991 has led to GaN LED based lightbulbs that are commercially available through Soraa® (product MR16) for $32.99. They consume 75% less power and run 10 times longer than 60 Watt incandescents. The commercial impact of GaN-based LEDs is vast, with a current market size of $12.9b (as of 2014). Current studies predict that GaN-based LEDs will capture between 88 and 90 percent of the lighting market by 2020 [36, 39].

As this work focuses on the design and fabrication of GaN-based lasers, it is important to note that GaN-based laser diodes also have great potential as light sources. The laser based automobile headlights in the 2015 BMW i8 is one such example [4]. Figure 2.3 demonstrates the two-fold enhancement in road visibility provided by GaN laser diode based headlamps, compared to LED models. Furthermore, the laser diode also consumes half of the power and has a light emitting surface 100 times smaller than its LED counterpart [4]. Specific advantages of GaN-based laser diodes include: their peak efficiency occurs at operating currents up to 2,000 times greater than that of LEDs, they do not experience droop (a rapid decline in efficiency as the current is increases), light emission is within very tight beam angles that permit long throw, and the emission areas are up to 10,000 times smaller than LEDs [40].

While the lighting applications presented here may seem somewhat removed from GaN-based optical microcavities it is important to note that due to their small size,

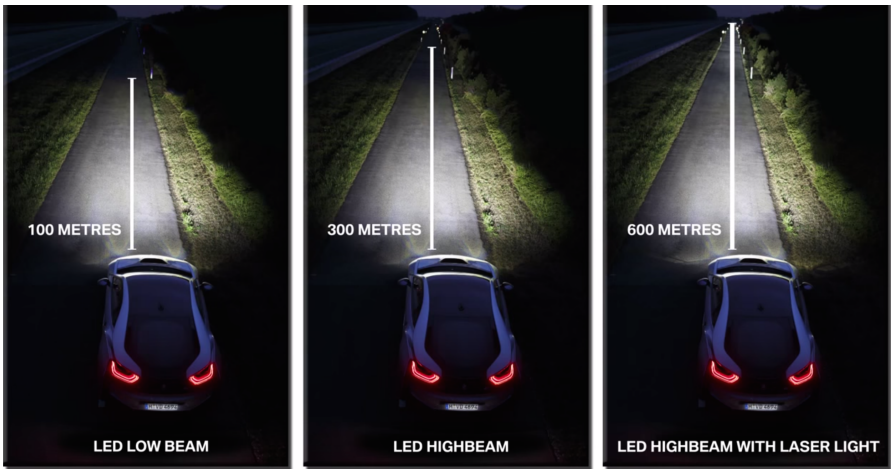

FIGURE 2.3: Schematic of the enhanced visibility from a GaN laser diode based headlamp compared to a GaN LED headlamp [4]. This provides one example where laser diode based sources are desirable over LEDs.

GaN-based microcavities, serve as an excellent platform to study the fundamental material properties of InGaN emitters. Experimental results presented later in this work are obtained with laser devices that contain as few as zero dislocations and statistically less than five QDs that are coupled to the lasing mode. As mentioned previously, the light emitted from the laser device serves as an excellent probe as it contains information regarding the material properties. The feedback loop between device performance, understanding the physical system, and material growth is a reoccurring theme and motivating principle throughout this work. It is schematically represented in Figure 2.5. It is also important to note that while not discussed in this work, other GaN-based devices, such as solars cells and High Electron Mobility Transistors (HEMTs) can also greatly benefit from an enhanced understanding of the operating principles behind GaN and its alloys.

Aside from the broader implications of this work toward improving the understanding and performance of InGaN emitters, there are very direct applications which make InGaN QDs embedded in GaN microcavities an exciting platform to study. The first

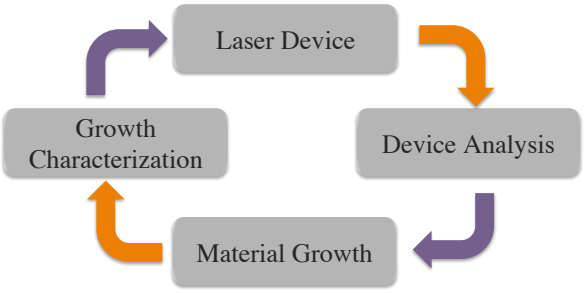

FIGURE 2.4: The process flow implemented in this work in order to improve the growth of nitride materials and the performance of the fabricated laser devices.

advantage of nitrides over other other III-V materials is the materials' high exciton binding energy. A simple modification of the Bohr model which accounts for the different permittivity and effective electron mass in semiconductors yields Eq. 2.1.

$$E_b(n) = \frac{m_e^*}{m_e}\frac{1}{\epsilon_r^2} \cdot \frac{13.6eV}{n^2} \tag{2.1}$$

A high exciton binding energy is desirable, as it reduces the possibility of thermal decomposition of the elecron-hole pair, and hence leads to improved performance at high temperatures and high powers. Interestingly, the binding energy is correlated to the band gap, as wide band gaps often have higher effective masses for the electron and light-hole, compared to narrow band gap semiconductors [41]. Inserting the respective values of ϵ_r (12.9, 8.9) and m_e^* ($0.063m_e$, $0.2m_e$) for GaAs and GaN into Eq. 2.1, one obtains binding energies of 4 meV and 34 meV, respectively. As the thermal energy at room temperature is approximately 25 meV, GaN and its alloys are expected to have greatly enhanced performance at room temperature compared to other III-V emitters [31]. Furthermore, one can increase the exciton binding energy even further than the bulk value by employing an additional confinement potential in the form of a quantum well (QW) or quantum dot (QD). This additional potential causes a further reduction in the Bohr radius compared to the bulk value, which in turn increases the binding energy.

Calculations give binding energies as high as 50 meV and 67 meV for non-polar QWs and QDs, respectively [42, 43]. It is important to note that the presence of an internal field reduces the binding energy somewhat as the electron-hole wave function overlap is reduced. This leads to an increase in the spontaneous emission lifetime of carriers and contributes to increased lasing thresholds as is discussed in Section 3.4.

Another useful implementation of InGaN QDs within GaN microcavities is the promise of on-demand single photon sources operating at room temperature. Such a source has been realized at 4 K using InAs QDs within a GaAs microdisk. It is of considerable interest as "an essential element of secure key distribution in quantum cryptography is an optical source emitting a train of pulses that contain one and only one photon." [44] Recent results have demonstrated GaN QD single photon sources operating near or above room temperature [45–47]. One could also conceive of semiconductor quantum qubits operating at room temperature, as the InGaN QD is mathematically equivalent to an atomic system in terms of the confined electrons wave functions and energy levels. Thus the QD coupled to a cavity mode is equivalent to an atom coupled to a cavity mode, which has been shown to be an effective quantum computing platform [48, 49]. In moving towards this goal, experiments have demonstrated strong coupling between a single QD and a microcavity in the arsenide material system. However, to-date, there have been no reports of strong coupling of a GaN-based QD and microcavity resonators [50, 51]. Recent results have demonstrated Rabi oscillations in a non-polar InGaN QD, which serve as a critical first step towards quantum information processing in GaN [52]. Other methods of quantum computation rely on cooling the system to cryogenic temperatures in order to cross the Curie temperature and make a material superconducting or to stably trap cold ions within an optical lattice [53, 54]. Furthemore, as the QDs are embedded within the optical cavity once the device is fabricated,

it is extremely robust. An example of this is a GaAs photonic crystal device with an embedded InAs QD that was fabricated in 2006 still being utilized as of 2012 [7, 55]. As GaN possess significantly higher material hardness (5GPa) than other III-V materials, devices fabricated out of GaN promise to be even more robust than their arsenide-based counterparts [56, 57].

2.2.2 Exciton-polariton lasers

Another advantage of InGaN QDs relates to their use as the active medium in exciton-polariton lasers. Exciton-polariton lasers operate on the principle of strongly coupling an optical cavity to an emitter. A system is considered strongly coupled in this context when the coupling rate between the exciton and cavity photon (g_0) exceeds the exciton (γ_0) loss rate and cavity loss rate (γ_c). Qualitatively, this means that the photon is more likely to interact with an exciton before the exciton decays or the photon escapes the cavity. For a cavity with parabolic dispersion strongly coupled to an exciton there exists an anti-crossing of the two states which upon diagonalization of the Hamiltonian leads to the formation of two new hybrid states. These are known as the upper and lower polariton branches. Mathematically, one can derive the polariton states by first considering the Hamiltonian of the uncoupled exciton and photon system as given in Eq. 2.2.

$$\begin{aligned} \hat{H} &= \sum_k E_X(k)\hat{b_k}^\dagger\hat{b_k} + E_{cav}(k)\hat{a_k}^\dagger\hat{a_k} \\ E_X(k) &= E_X(0) + \frac{\hbar^2}{2m_X} - \frac{i\hbar}{2}\gamma_X(k) \\ E_{cav}(k) &= \sqrt{(\frac{hc}{\lambda_0})^2 + (\frac{\hbar ck}{n_{cav}})^2} - \frac{i\hbar}{2}\gamma_{cav}(k) \end{aligned} \tag{2.2}$$

Where $\hat{H}$ is the Hamiltonian of the uncoupled system, $E_X(k)$ and $E_{cav}(k)$ are the energy as a function of momentum for the exciton and photon, respectively. $E_X(0)$ is the exciton binding energy, $\hat{a}^\dagger$ ($\hat{b}^\dagger$) and $\hat{a}$ ($\hat{b}$) are the photon (exciton) creation and annihilation operators, respectively. m_x is the exciton mass, γ_X is the exciton decay rate, γ_{cav} is the cavity photon decay rate, n_{cav} and λ_0 are the index refraction and wavelength of the cavity, respectively. If we now consider the situation where the exciton-photon coupling strength (defined as Ω) is large one has the interaction Hamiltonian ($\hat{H}_{int}$) and therefore coupled Hamiltonian given ($\hat{H}_{X-cav}$) in Eq. 2.3 [5, 33, 58].

$$\begin{aligned} \hat{H}_{int} &= \hbar\Omega\hat{a}^\dagger\hat{b} + \hbar\Omega\hat{b}^\dagger\hat{a} \\ \hat{H}_{X-cav} &= \begin{pmatrix} E_X(k) & \hbar\Omega \\ \hbar\Omega & E_{cav}(k) \end{pmatrix} \end{aligned} \tag{2.3}$$

Upon diagonalizing the coupled Hamiltonian, described by the matrix $\hat{H}_{X-cav}$, one finds the two new eigenstates. These are referred to as the lower and upper polariton state. Figure 2.5 shows the dispersion of the cavity mode and exction, as well as the upper and lower polariton branches, from [5].

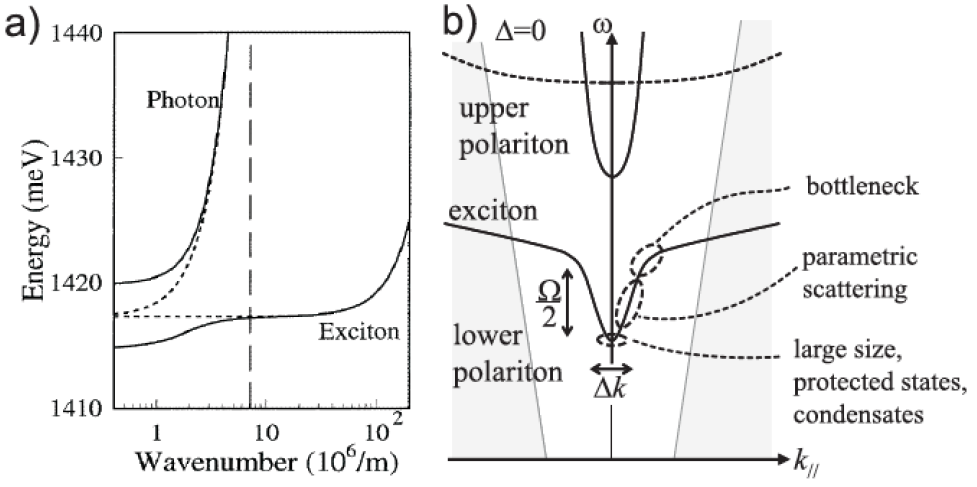

FIGURE 2.5: a) (Solid line) dispersion of the upper and lower polariton branches that are obtained by strongly coupling a DBR cavity mode with an exciton (dashed-lines). b) Zoomed-in image of the lower polariton branch, showing that the dispersion leads to protected states where polaritons can condense. Both images are from [5].

Interestingly, because the exciton-polaritons are bosons they can form a Bose-Einstein Condensate (BEC) at the minimum of the lower polariton branch. When a polariton in the BEC decays, the exciton is destroyed and a *coherent* photon is emitted from the cavity. The coherent light emission has been shown to be thresholdless, as population inversion is not required to form a BEC in the potential well. Such a device is referred to as a "polariton laser" and is of immense scientific interest. Recent progress includes an electrical injectied polariton laser [59–61]. For a more detailed discussion of the operating principles behind a polariton laser, please refer to reference [5].

In Figure 2.5 the depth of the potential energy well in the lower polariton branch is given by $\Omega/2$. This is of great importance because if the thermal energy of the bosons (kT) is greater than $\Omega/2$, then the bosons can escape the potential well or disintegrate due to the thermally induced recombination of the exciton. Thus, it does not form a condensate. It is therefore desirable to utilize materials with high exciton-photon coupling strengths, which is defined by Eq. 2.4 [62].

$$\begin{aligned} \Omega &= 2\sqrt{g_0^2 - \left(\frac{\delta\omega_0 - \delta\omega_c}{4}\right)^2} \\ g_0^2 &= \left|\langle \vec{d} \cdot \vec{E} \rangle\right| = \frac{q^2 f}{4\epsilon m_0 V} \end{aligned} \tag{2.4}$$

Where a Lorentzian lineshape is assumed for the exciton and cavity mode with $\delta\omega_0$ and $\delta\omega_c$ representing the full width at half maximum (FWHM) of the exciton and cavity, respectively. $\vec{d}$ is the dipole moment of the exciton, ϵ is the dielectric constant of the material, $\vec{E}$ is the electric field of the cavity mode, f is the exciton oscillator strength, m_0 is the free electron mass, and V is the modal volume of the cavity mode. The second term under the square root in Eq. 2.4 accounts for the decrease in exction-photon coupling due to the lack of overlap of the Lorentzian lineshapes. From Eq. 2.4, one can

see that a small modal volume and high oscillator strength is desirable to increase the exciton-photon coupling strength. Furthermore, one can represent the exciton oscillator strength in terms of the exciton lifetime (τ_0) and emission frequency (ω_0), as given by Eq. 2.5 [63].

$$f = \frac{1}{\tau_0} \cdot \frac{6\pi\epsilon_0 m_0 c^3}{nq^2\omega_0^2} \cdot \left(\frac{a_b}{a}\right)^3 \tag{2.5}$$

Where a is the unit cell length and a_b is the exciton Bohr radius. Section 5.1 discusses how one can decrease the exciton lifetime by utilizing a confinement potential such as a QW or QD. Due to their small size, QDs provide the highest localization of excitons and therefore highest achievable oscillator strengths. Furthermore, by utilizing wide band gap semiconductors such as InGaN with small unit cell lengths (a), one can increase the oscillator strength, compared to other III-V materials shown in Figure 2.1 [64]. Full calculations of the polariton dynamics, shown in Figure 2.6 confirm our results, as the critical temperature in order to form a BEC is below 60K and 500K for GaAs and GaN, respectively.

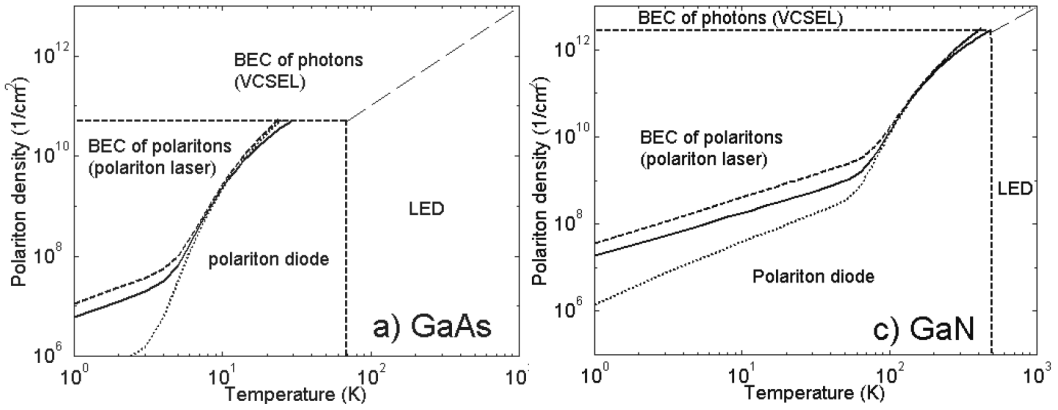

FIGURE 2.6: "Phase diagrams for GaAs and GaN-based microcavities at zero detuning. Vertical and horizontal dashed lines show the limits of the strong-coupling regime imposed by the exciton thermal broadening and screening, respectively. Solid lines show the critical concentration Nc versus temperature of the polariton KT phase transition. Dotted and dashed lines show the critical concentration Nc for quasi condensation in a 100 nm and in a one meter lateral size systems, respectively. The thin dashed line (upper right) symbolizes the limit between vertical cavity surface emitting laser (VCSEL) and light-emitting diode regimes," adapted from [5].

As an additional note, the cavity dispersion depends on the optical cavity design. In the case described above a distributed Bragg reflector (DBR), and is not parabolic for PCCs or microdisks. The polariton dispersion of microcavities, such as micropillars, has been shown to reduce the momentum conservation constraints for polaritons to condense into the protected state [65, 66]. In fact, polariton lasing has been demonstrated between a single InAs QD embedded within a GaAs photonic crystal cavity [67]. These findings serve as an additional motivation for the realization of microcavity structures.

2.3 Challenges with InGaN emitters embedded in GaN optical microcavities

As mentioned previously, there are substantial difficulties inherent to the nitride family of semiconductors which must be addressed in order to realize the next generation of GaN-based devices. In this section, we introduce these challenges as well as potential solutions implemented throughout this work.

2.3.1 Internal fields

One of the most striking features of Wurtzite phase GaN and its alloys, is the presence of internal fields in the [0001] direction, parallel to the c-axis. The fields originate due to the presence of a spontaneous and piezoelectric polarization within the material, referred to as $\vec{P}_{sp}$ and $\vec{P}_{pz}$, respectively. Once the polarization is known, one can calculate the charge density (ρ) and therefore electric fields within the material using Eq. 2.6.

$$\rho = -\vec{\nabla} \cdot \left(\vec{P}_{sp} + \vec{P}_{pz} \right) \tag{2.6}$$

The origin of the polarization within the GaN and its alloys stems from the arrangement of the gallium (or indium) and nitrogen atoms in the non-centrosymmetric Wurzite crystal. The higher electronegativity of the nitrogen atoms, compared to the gallium or indium atoms causes the electrons in the crystal to be more localized near the nitrogen atoms. This gives rise to a spontaneous polarization. Figure 2.7 shows the tetrahedral arrangement of the gallium and nitrogen atoms that gives rise to the spontaneous polarization in c-plane GaN and its alloys. The [0001] and [000$\bar{1}$] directions have opposite terminating charges, leading to polarization charges at the boundaries of the GaN layer.

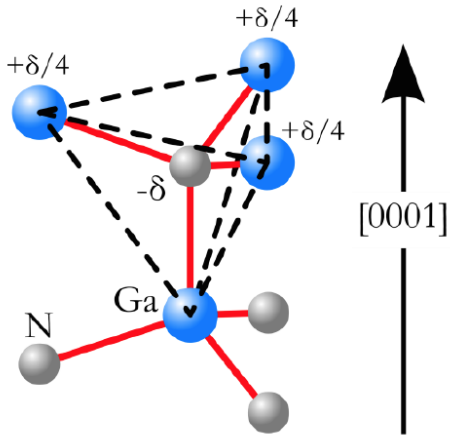

FIGURE 2.7: Unit cell of GaN showing that the arrangement of the gallium and nitrogen atoms gives rise to a inhomogeneous charge distribution, which in turn leads to internal fields in the c-plane, adapted from [6].

The piezoelectric polarization is somewhat self-explanatory as it arises from the deformation of the GaN crystal structure. This in turn displaces the gallium, or indium, and nitrogen atoms. Depending on the exact form of the deformation, the piezoelectric polarization can either contribute to or cancel the inherent spontaneous polarization within the material. For the purpose of this work, there is never any external pressure applied to the structure. Therefore the entirety of the piezoelectric polarization is due to internal strain within the material. One can mathematically calculate $\vec{P}_{pz}$ using the

piezoelectric (d_{ijk}) and strain tensors (σ_{ij}), as given in Eq. 2.7.

$$P_k^{pz} = d_{ijk}\sigma_{ij} \tag{2.7}$$

The consequence of the polarization within c-plane GaN is that internal fields bend the electronic bands for any c-plane heterostructure device, such as a QW or QD. As the electron and hole have different charges, this leads to a delocalization of the exciton and therefore a reduction of the spontaneous emission rate, oscillator strength and cavity photon-coupling rate. Mathematically, this is due to the reduction of the wave function overlap between the electron and hole, given in Eq. 3.39. Figure 2.8 shows a band structure calculation (simulated using nextnano3) of the electron and hole wave function overlap within a 4nm $In_{0.3}Ga_{0.7}N$ QW sandwiched between GaN.

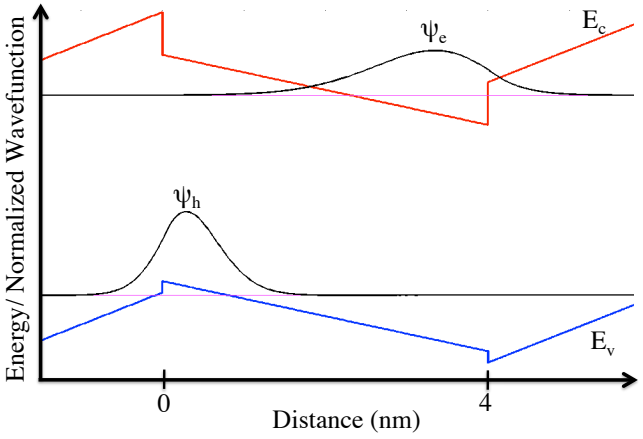

FIGURE 2.8: Bandstructure of a 4nm $In_{0.3}Ga_{0.7}N$ QW between GaN. The energy levels (pink lines) as well as wave functions of the electron and hole (black line) are numerically solved using a Schrödinger-Poisson solver (nextnano3).

From Figure 2.8, one can see that the electron-hole wave function overlap is significantly reduced as a result of the electron and hole being spatially localized in different regions of the QW. Interestingly, there are at least two possible solutions in order to

overcome this undesired effect. The first is the most obvious and involves the use of non-polar Wurzite phase GaN. There are multiple such planes of GaN that are non-polar. The most popular is the m-plane and a-plane. However, the growth of a-plane and m-plane GaN is significantly more difficult than c-plane GaN due to the lack of lattice matched substrates. Natural-non polar substrates such as m-plane SiC or $LiAlO_2$ lead to "dislocation densities on the order of $10^{10}cm^{-2}$, and basal plane stacking fault densities on the order of 10^5cm^{-2}. Extended defects, namely threading dislocations, act as non-radiative recombination centers and subsequently lead to low efficiencies and low output powers when their density is high." [68] To overcome the substrate problem, c-plane wafers are often precisely diced along non-polar planes. This is laborious and wasteful of material. Significant progress has been made with recent achievements including the demonstration of non-polar and epitaxial lateral overgrowth (ELOG) (discussed in Figure 2.18) LEDs, laser diodes, vertical-cavity surface-emitting lasers (VCSELs) and microdisk cavities, as well as InGaN QDs [69–73].

The other method to eliminate the effect of the internal fields involves applying an external bias across the GaN structure. The magnitude and polarity of the bias can be adjusted to precisely cancel the internal fields and therefore increase the oscillator strength. This approach was first demonstrated by Jarjour et al. (2007) and has been confirmed in this work [74]. Figure 2.9 illustrates the tuning of the wavelength, and therefore oscillator strength, of a QD exciton through the application of an external bias.

The data in Figure 2.9 was obtained using a micro-photoluminesence (μ-PL) setup with an integrated current source to facilitate electrical tuning. It is schematically shown in Figure 2.10. This setup is used for all of the optical measurements throughout

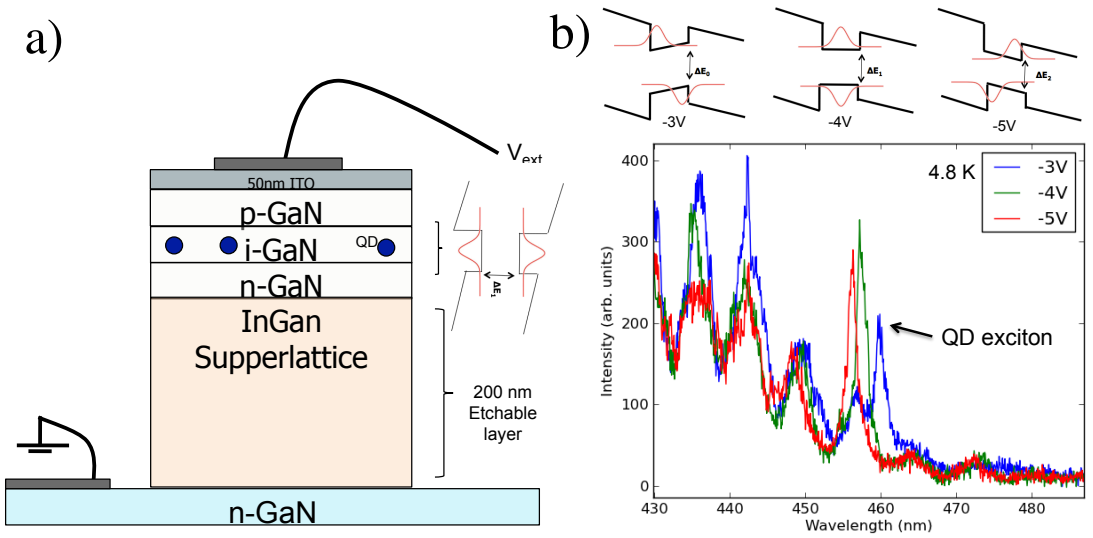

FIGURE 2.9: a) Schematic of the material structure with embedded InGaN QDs. b) Measurement of the exciton wavelength vs. external bias. The tuning is completely reversible as there are no hysteresis observed. Dr. Kasey Russell contributed equally to this work.

this work and has the ability to measure spectrums, emitter lifetimes and second order correlation functions (when a second APD is utilized).

While the cancellation of the internal fields in polar GaN is promising, several challenges still remain before this technique can be implemented in a photonic device. First, a metallic contact layer is required on top of the photonic crystal device in order to efficiently inject carriers. This layer must be transparent in order to collect the photoluminescence signal from the QDs, but it poses a challenge in fabricating a high Q photonic crystal or microdisk cavity, as even small absorption in the indium tin oxide (ITO) layer can dramatically lower the cavity photon lifetimes. However, if such difficulties are overcome, one could envision a QD-cavity system where the QD is electrically tuned into resonance with the cavity mode. Such a device would be of great practical importance as it could compensate for slight fabrication errors that can detune a cavity mode from its intended wavelength, leaving the QD-cavity system uncoupled.

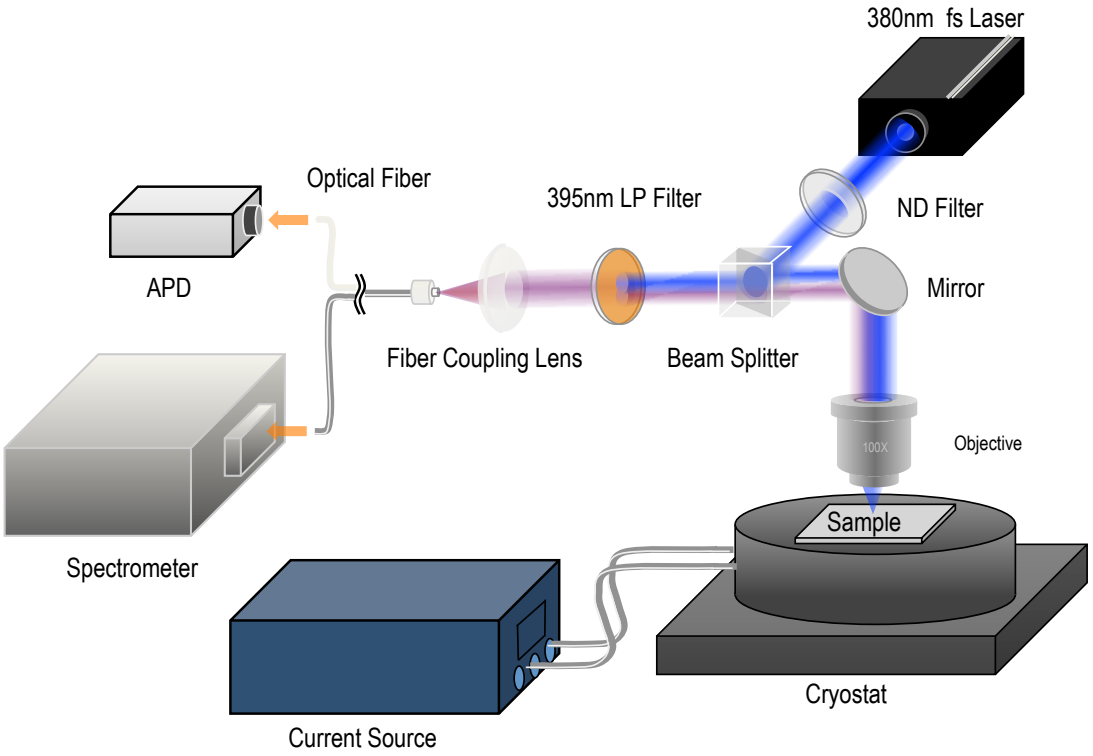

FIGURE 2.10: μ-PL setup used for all the optical data collection presented in this work. Thank you to Dr. Tsung-li Liu for his assistance in creating this figure.

2.3.2 Chemical inertness

While the chemical inertness of a material may initially seem like a desirable parameter, as it means the material is resistant to corrosion, it greatly complicates the fabrication of photonic cavities. Many photonic microcavity devices, such as PCCs and microdisks, rely on chemically etching a sacrificial layer in order to surround the cavity membrane in the vertical dimension with air. Similar to our discussion of in-plane confinement of modes within the microdisk, the high index contrast between air (n=1) in comparison to GaN (n=2.48 @ λ = 450nm) allows waveguiding in the vertical dimension. Figure 2.11 shows the electric field intensity in the vertical dimension of a 450 nm photon in a 120 nm GaN membrane surrounded by air. The electric field can be solved analytically by directly mapping the Maxwell boundary conditions to a quantum finite potential well. The mode shown in Figure 2.11 is the analogue of a ground state wavefunction. Thank

you to Aun Zaidi for his help developing the eigenmode solver.

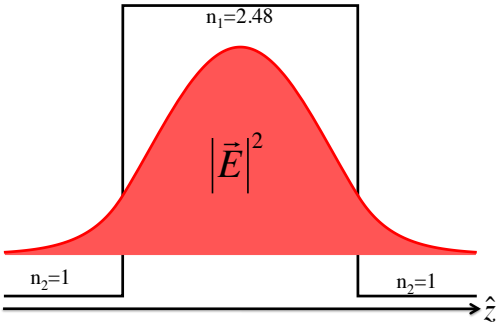

FIGURE 2.11: Electric field profile in the $\hat{z}$ direction for a 120nm GaN membrane. A single mode is clearly confined within the membrane.

For GaAs membranes, the sacrificial layer is usually $Al_xGa_{1-x}As$, where x is approximately 0.3. This layer can easily be removed in a dilute hydrofluoric (HF) acid etch and produces beautiful undercut structures, such as the PCC shown in Figure 2.12, adapted from [7].

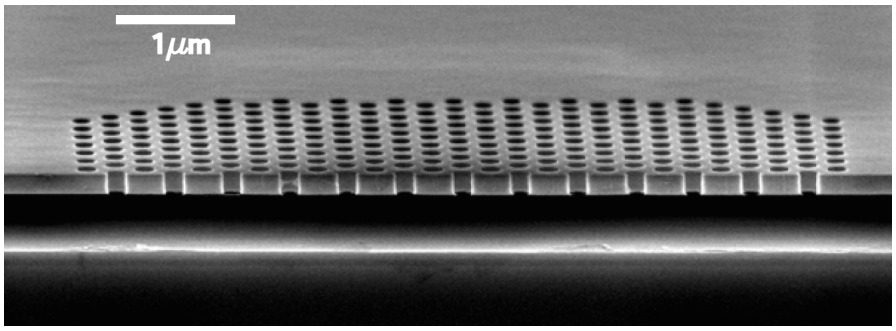

FIGURE 2.12: Cross section perspective SEM image of an undercut GaAs PCC where an $Al_{0.3}Ga_{0.7}As$ layer was removed with diluted HF. The lack of residual material left on the bottom of the GaAs membrane contributes to the high Q of the device as there is minimal photon scattering from the membrane [7].

As there is no effective selective room-temperature wet chemical etch for GaN or its alloys, a variety of techniques have been developed to fabricate suspended membranes. Specific methods to create an undercut structure include: the growth of GaN on Si (etched in potassium hydroxide (KOH)), selective oxidation and etching of AlInN in nitric acid, and photoelectrochemcial (PEC) etching (exclusively used in this work) [75–79]. PEC etching is a selective etching process that relies on the band gap mismatch

between a sacrificial $In_xGa_{1-x}N$ layer and the surrounding GaN [8, 79]. The process flow is as follows. A dry etch is used to define a cylinder of GaN. A cathode is then placed to allow the electrons to be swept away and chemically reduce the diluted HCl solution the sample is immersed in. This process is mediated by incident photons that are spectrally filtered such that electron-hole pairs are only generated in the narrow band gap sacrificial layer. The remaining holes are then swept to the surface where they oxidize the sacrificial layer. The InGaN oxide complex is then etchable in HCl, allowing for the removal of the sacrificial layer. Figure 2.13 shows a simplified schematic of the PEC etch process, adapted from [8].

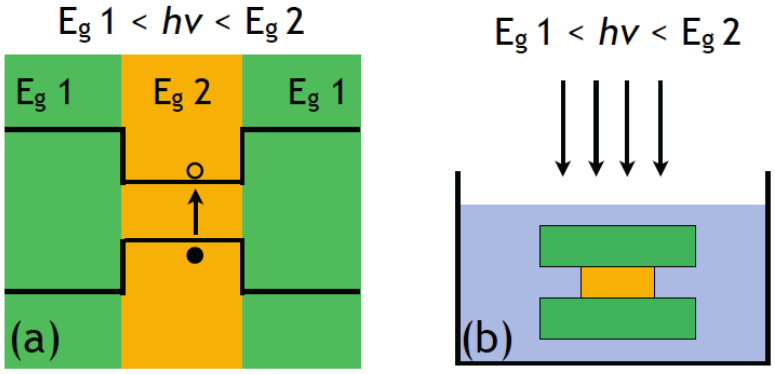

FIGURE 2.13: Simplified schematic of the PEC etching process, allowing for the removal of a sacrificial layer (yellow) and therefore realization of a suspended cavity membrane [8].

A detailed schematic of the PEC etching process utilized in this work is given in Figure 2.14 from [6].

For the devices fabricated in this work, we utilized a .004M HCl solution, 1000W xenon lamp and 5 nm/50 nm : Ti/Au cathode. Initial investigations found no significant improvement of the undercut in the presence of a 20 nm nickel anode in the center of the top surface of the microdisk, as was done in reference [8]. Under the proper conditions the PEC technique can be very effective in creating undercut devices. Figure 2.15 shows

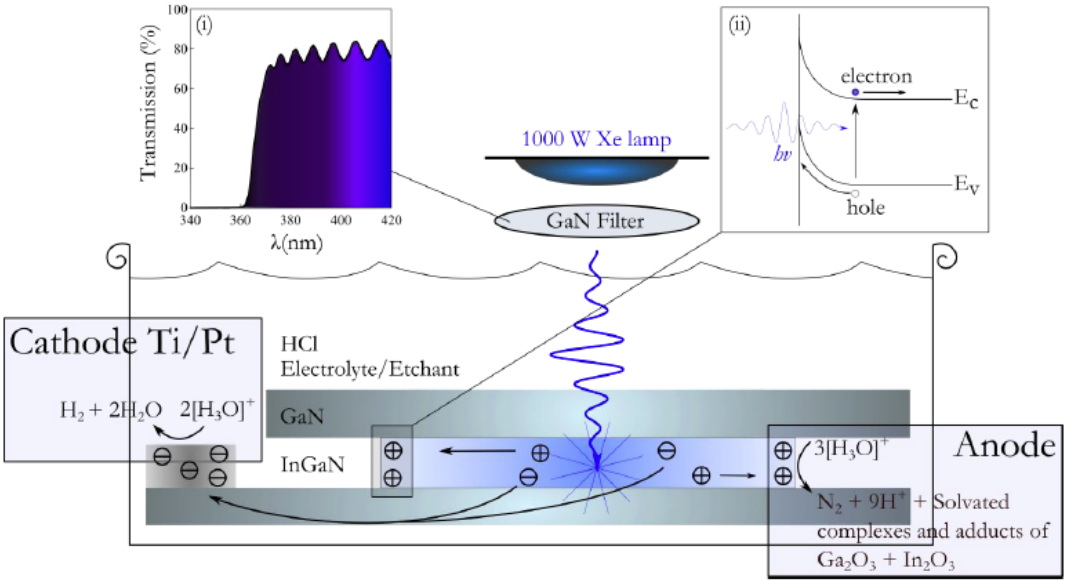

FIGURE 2.14: Detailed schematic of the PEC etching process utilized in this work, from [6].

an example of an undercut microdisk cavity fabricated using the conditions described above.

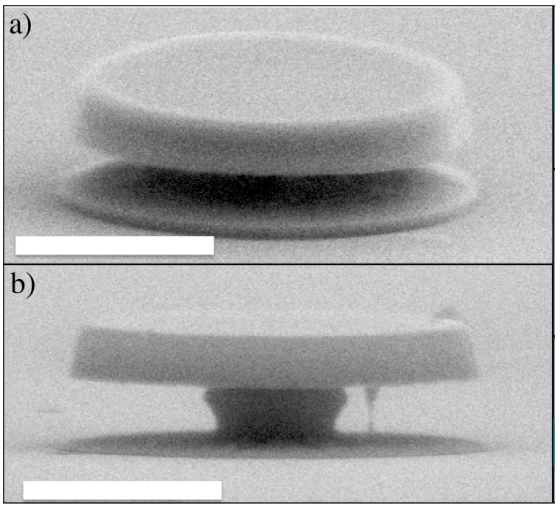

FIGURE 2.15: Perspective and side view of a 1 μm GaN microdisk. Both the sacrificial and membrane layers have a thickness of 200nm. The scale bar is 500nm in width.

A variety of problems can occur during the PEC etching, leading to poor membrane undercuts. This can be due to a variety of reasons including high contact resistance of the cathode and threading dislocations within the sacrificial superlattice which act as electrically resistive pathways that inhibit etching. Surface damage incurred during

the chlorine based inductively coupled plasma (ICP) dry etch can also lead to reduced efficacy of the PEC technique [80]. We return to a more in-depth discussion of the precise mechanism for a non-ideal PEC undercut in Section 7.4. Figure 2.16 shows one example of a poorly undercut microdisk device.

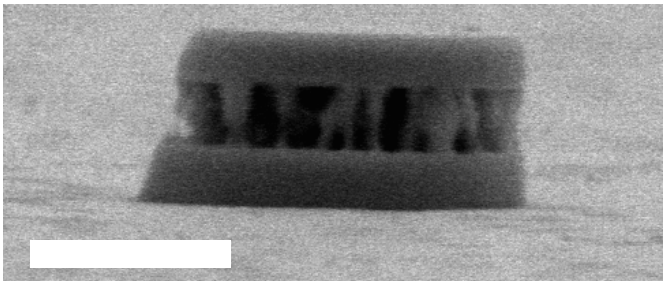

FIGURE 2.16: A 1 μm Microdisk cavity with a poor undercut. Such a device will have short photon lifetimes (Q≈200) due to the presence of light leakage and scattering from the membrane. The scale bar is 500nm in width.

2.3.3 Threading dislocations

Threading dislocations have been ubiquitous within GaN devices since the material grown on sapphire substrates was first successfully demonstrated. The origin of threading dislocations is a result of poor matching in the lattice parameter and thermal expansion coefficients between GaN and the sapphire substrates on which it is commonly grown [81, 82]. This leads to typical dislocation densities on the order of 10^8 to 10^{10}cm^{-2}. These correspond to between 1 and 100 dislocations within each 1μm diameter microdisk. "As a comparison, homoepitaxially grown GaAs exhibits 10^2 to 10^4 dislocation cm^{-2}, and homoepitaxial Si almost 0." [9] Threading dislocations pose a number of challenges for GaN based devices because they act as electron scattering and non-radiative recombination centers [83, 84]. For the purposes of this work, they compromise the efficacy of the PEC undercut as the high resistivity of the threading dislocations prevents the removal of electrons and subsequent etching of the dislocation region. Such defects may also compromise the electrical or photonic behavior of the device. This leads to the

formation of "whiskers" on the underside of the microdisk or PCC which in turn have been shown to lower the quality factor of the photonic device as they strongly scatter light [2]. Figure 2.17 shows an example of a $1\mu m$ diameter microdisk with a whisker.

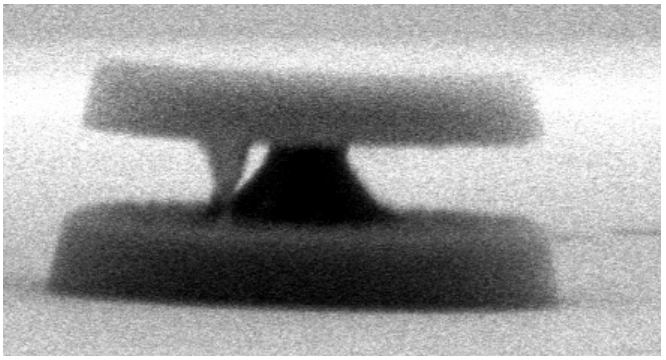

FIGURE 2.17: A $1\mu m$ microdisk cavity with a "whisker" caused by the presence of a threading dislocation near the periphery of the disk. Such whiskers act as a scattering mechanism for light and lower the device Q.

Currently, several techniques are implemented to reduce the threading dislocations densities in GaN. The first involves growth of GaN on GaN substrates. This leads to threading dislocations densities as low as 10^6 cm^{-2} [85]. However, such substrates are currently in limited quantities and cost-prohibitive. Another method involves patterning stripes of SiO_2 or SiN on the GaN surface. This method is known as epitaxial lateral overgrowth (ELOG). It can reduce the threading dislocation density below 10^7 cm^{-2}. As threading dislocations cannot bend sideways, there are low dislocation density regions of GaN above the oxide stripe [9]. Figure 2.18 is a schematic of the ELOG growth technique adapted from reference [9].

In an effort to improve device performance, growth on GaN substrates as well as ELOG is implemented for microdisk devices and is discussed in Section 7.4. Therefore we return to a more detailed discussion of threading dislocations later in this work.

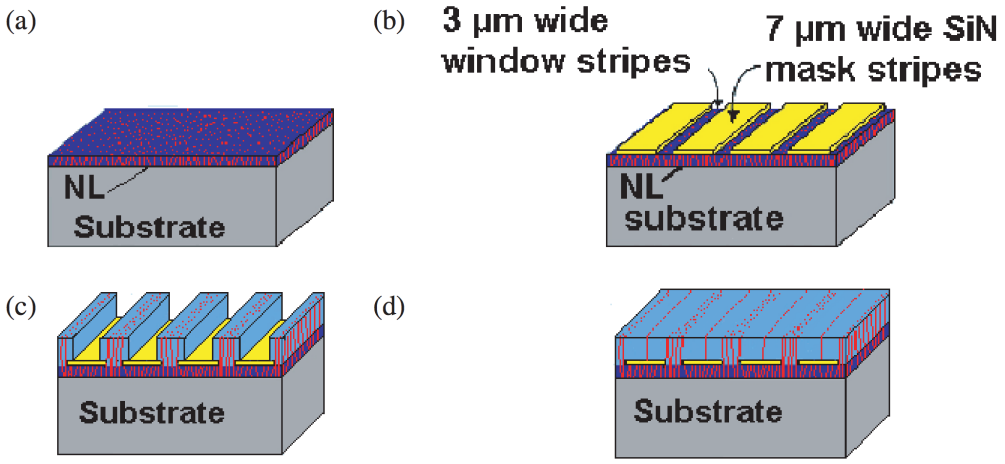

FIGURE 2.18: Process flow for the growth of ELOG GaN, adapted from [9]. This leads to regions of low dislocation density GaN above the oxide stipe. The dislocations and GaN are colored in red and light blue, respectively.

2.3.4 InGaN QD growth

All devices presented in this work were grown in the Dr. Rachel Oliver group at Cambridge University via metalorganic vapor phase expitaxy (MOVPE). While MOVPE is one of the most widely utilized industrial growth methods for GaN-based materials, InGaN QD growth via MOVPE is arduous. This is due to the lack of a lattice mismatch and therefore strain between InGaN and GaN, in addition to the presence of residual and unwanted hydrogen during the growth. These effects inhibit QD formation via the Stranski-Krastanov (SK) mechanism. This is used to form arsenide and phosphide based QDs [86–88]. The hydrogen inhibits SK growth by passivating the GaN c-plane. In turn, this lowers the surface energy of the c-plane below the point necessary for facilitating the SK growth mechanism. This challenge was overcome by Oliver et al. (2003) by utilizing a technique known as Modified Droplet Epitaxy (MDE). The full details of the MDE technique are described in references [2, 32], however, in brief an InGaN QW is first grown and then annealed in nitrogen. This induces the formation of indium rich regions. These indium rich regions can partially evaporate and then coalesce on the

surface to form indium droplets. Finally, a GaN capping layer is grown causing the indium rich droplets to become InGaN QDs embedded in GaN.

For the purpose of this work the MDE method of InGaN QD growth poses several challenges in terms of realizing microcavity devices. First, the QD density can vary by as much as an order of magnitude ($2.8\pm0.1 \times10^{10}$ to $2.5 \pm0.1 \times10^{9}$ cm^{-2}) between growth runs, with nominally the same growth conditions. This can lead to confusion as certain wafers will exhibit higher performance than others, even though the devices were grown and processed identically. This work employes statistical measurements in order to overcome variations between (and even within) wafers, which by nature necessitates the fabrication and measurement of many devices. The second challenge relates to the presence of a unique InGaN layer, known as fragmented quantum well (FQW). In addition to forming QDs, the MDE growth mechanism also creates a "broken" InGaN QW layer that also luminesceses. Deconvolving the emission from the QD and FQW can be difficult and was only conclusively demonstrated in this work when the luminescence of the FQW and QDs were spectrally separated. Figure 2.19 is a schematic of a QW, FQW and QD+FQW active layer, respectively, as well as an AFM image of the QD+FQW layer after the QD formation step but before the growth of the GaN capping layer. Only these three active regions are utilized throughout this work, with the vast majority of experiments being conducted on the QD+FQW samples. Furthermore, the QDs themselves suffer from spectral diffusion due to charge transfer with the surrounding GaN matrix. This leads to linewidth broadening and "hopping" of the exciton energy in time [89].

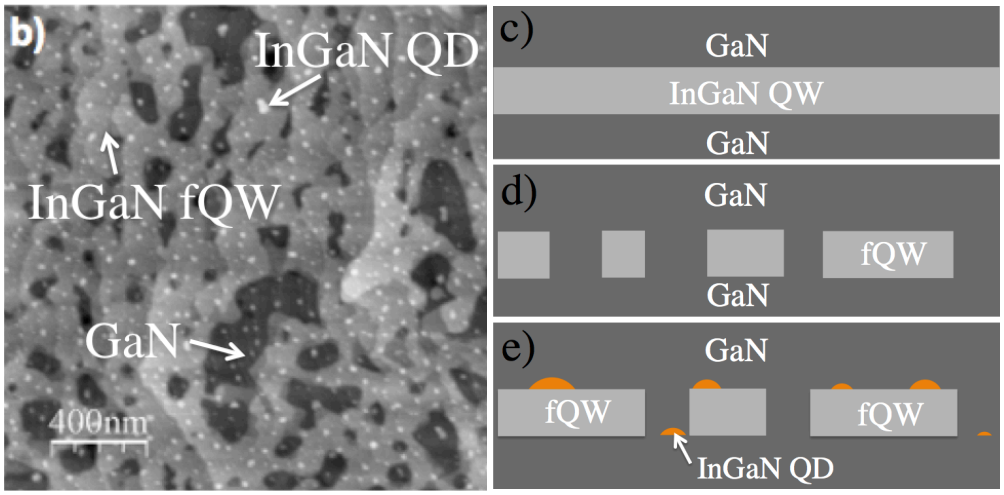

FIGURE 2.19: b) AFM image of the QD+FQW active layer with arrows denoting GaN (dark regions) FQW (gray regions), and QDs (white dots). c), d), e) Are schematics of one QW, FQW and QD+FQW active layers, respectively.

2.4 Previous work on InGaN emitters embedded in GaN optical microcavities

The development of a new semiconductor laser material often follows a very similar trajectory. Essentially the device thresholds take two steps forward and one step back. The first laser devices for a new material system usually utilize the bulk or a double heterostructure form of the gain medium. The thresholds steadily decrease over time. However, eventually there are diminishing returns as the gain of the material becomes the limiting factor towards realizing lower thresholds. At this point higher gain active regions such as QWs are investigated. The first of these devices invariably have higher thresholds then the optimized devices from the previous generation. However, as the gain media is improved, the performance far surpasses that of the previous generation. At this point, the cycle begins anew with the transition from QWs to QDs. Figure 2.20 is a plot of the threshold current density per year for GaAs based lasers, which visualizes the pattern [10].

The InGaN system is no different. While this work has broader impacts for GaN

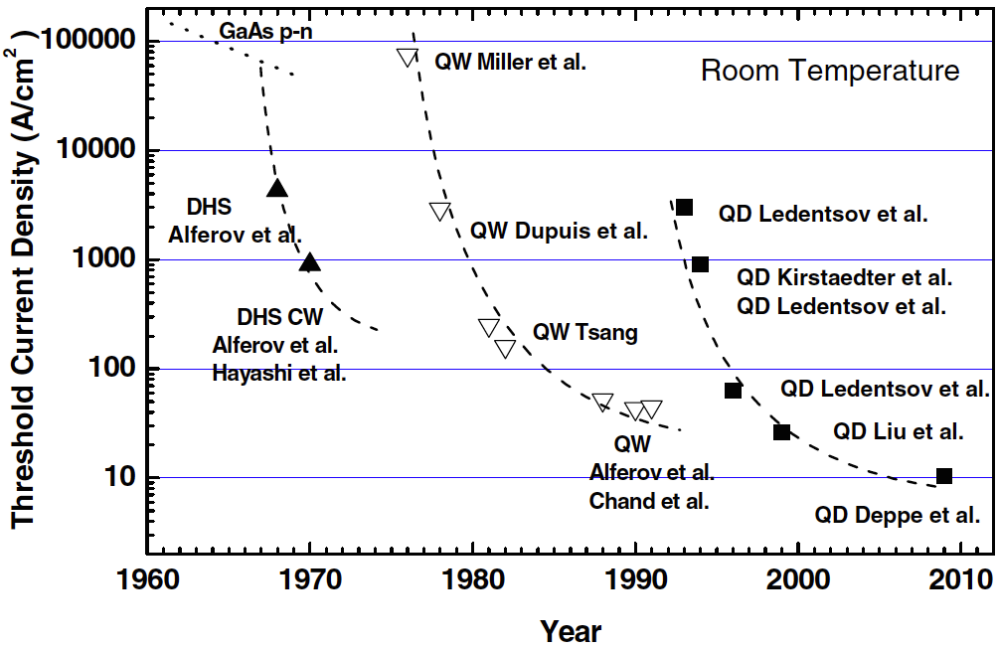

FIGURE 2.20: Lasing threshold of GaAs based lasers vs time. Each new form of the gain medium initially has ahigher lasing threshold than its predecessor but eventually exhbits increased performance over time. [10]

based devices (discussed in Section 8.2), in short, the work presented here details the push forward from InGaN QW to InGaN QD active layers. Furthermore, within each gain medium, devices are usually optically pumped with a pulsed laser first in order to reduce the effects of heating. Next, the device is improved to exhibit lasing to under continuous wave (CW) excitation and finally electrical injection. For all the devices in this work we will excite with a frequency double titanium sapphire laser (76 MHz repetition rate, 200 ps pulse length).

Previous to this work, the lowest threshold InGaN based laser to date had a CW lasing threshold of 300 W/cm^2 at room temperature and was achieved using 5 QW layers embedded in a 1.2 μm microdisk cavity [11]. Figure 2.21 shows an SEM of the completed device as well as a Light in-Light out (L-L) lasing curve which shows a clear kink indicative of lasing.

The first microdisk devices with embedded InGaN QDs were developed by Dr.

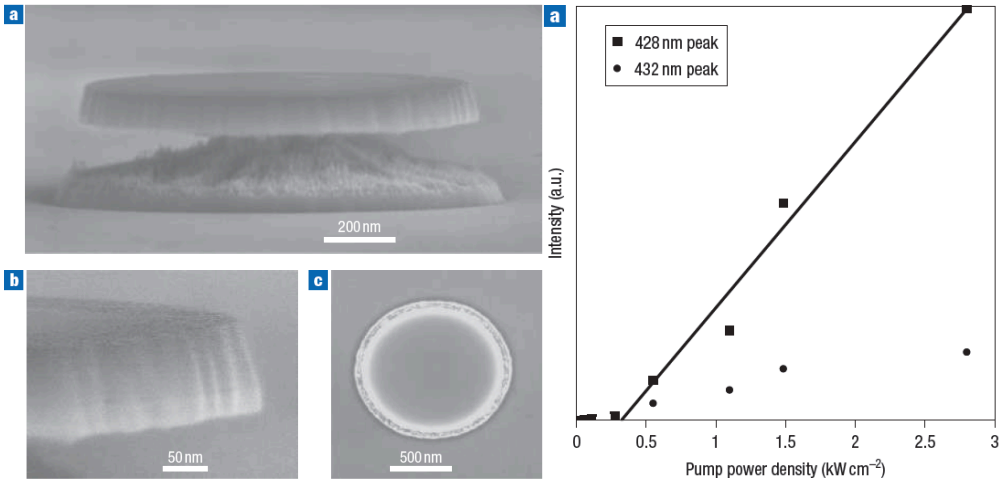

FIGURE 2.21: InGaN QW microdisk laser, which before this work had the lowest lasing threshold of any InGaN device to date [11].

Fabian Rol in Evelyn Hu's lab at Harvard University. Despite obtaining Qs as high as 6000, which represented a significant improvement compared to the highest Qs obtained by Dr. Adele Tamboli of 3,700, lasing was never observed from these devices. Figure 2.22 shows an SEM and PL spectrum of a microdisk with one layer of InGaN QDs fabricated by Dr. Rol.

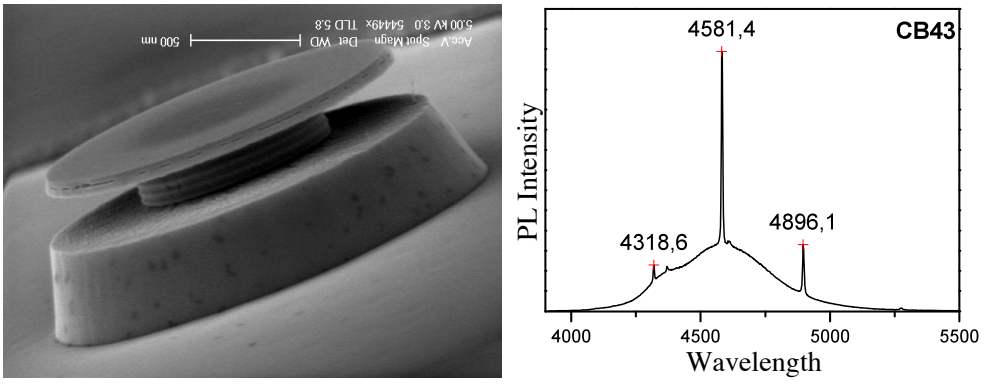

FIGURE 2.22: SEM and PL spectrum of an approximately 2μm microdisk cavity with one layer of embedded QDs fabricated by Dr. Fabian Rol.

These previous results led to several questions regarding the devices which were a driving motivation of the work completed in this thesis. A short list includes:

1. **Why did the InGaN QD devices not exhibit lasing?**

2. **Is it possible to increase the Q above 6000?**

3. **Are the InGaN QDs serving as an effective gain media?**

2.4.1 Conclusion

Part I discussed the advantages and challenges of GaN microcavites with embedded InGaN QDs. We also introduced previous work on GaN microcavities which motivated questions that this work has attempted to answer. We now conclude Part I and refer the reader to the experimental results section of this work in Part III, where we detail the effort to answer the above questions as well as future challenges that naturally arose throughout this work. Before doing so however, we focus on the underlying principles governing QD microcavity lasers in Part II.

Part II

QD microcavity lasers: Theory

Chapter 3

Quantum dots in microcavities: the ideal low-threshold laser

3.1 Introduction

In this section we derive the laser rate equations, which fully describe the properties of laser operation. Doing so offers insight into how a semiconductor laser device works, while identifying the key parameters toward optimizing its performance. In later sections we demonstrate that QDs theoretically have the highest gain of any known emitter and by placing them in a high quality factor low-modal volume microcavity, we can theoretically realize nearly thresholdless lasers.

3.2 Derivation of the Laser rate equations

A laser operates on the fundamental coupling between light and matter. While this effect may sound obscure, evidence of light-matter interaction is ubiquitous in our lives.

For example, the light emitted from the sun or a lightbulb can be detected by our eyes or with excess power even burn our skin. The origin of such phenomenon is due to the fact that photons and electrons have an intimate inter-relationship, if certain criterian are met. In certain circumstances this interaction can lead to light amplification by the stimulated emission of radiation otherwise known as a laser.

3.2.1 Carrier rate equation

Let us first consider a simple toy model consisting of a two-level system for which electrons can occupy either of the two states E_1 or E_2. The number of electrons in the state E_1 or E_2 will be denoted as n_1 or n_2, respectively. We will assume the total number of electrons n is conserved and satisfies the relationship $n = n_1 + n_2$. We will consider the process by which an electron can make the transition from E_1 to E_2 or vice versa via the absorption or emission of a photon, respectively. The optical excitation of carriers via the process of photo absorption is described by Eq. 3.1.

$$\left(\frac{dn_1}{dt}\right) = \frac{-1}{4\pi} B_{12} n_1 I(\lambda) \tag{3.1}$$

Here $I(\lambda)$ is the spectral radiance, or quantity of radiation within a given solid angle in a specified direction, of the light source and B_{12} is the probability per unit time per spectral radiance of the light source that an electron will absorb a photon and make a transition from from E_1 to E_2. In order for energy to be conserved, Eq. 3.1 is only valid for a two-level system if the energy of the photon is greater than or equal to the spacing between the two energy levels $\Delta E \equiv E_2 - E_1$.

$$E_p \geq \Delta E \tag{3.2}$$

The energy of the photon is $E_p = hc/\lambda$, c is the speed of light, and h is Planck's constant. We also assume if $E_p > \Delta E$ that the electron can relax into state E_2 via losing its extra energy, which in the case of semiconductors is typically mediated by phonon coupling. Because the absorption of a photon excites an electron from the lower energy level, to the upper energy level the population of electrons in the excited state must also vary. For simplicity it is more convenient to reformulate Eq. 3.1 in terms of the upper state population n_2 and a photon to electron conversion efficiency η which yields the first term in the laser rate equation Eq. 3.3.

$$\left(\frac{dn_2}{dt}\right) = \frac{\eta P_{in}}{Vh\upsilon} \tag{3.3}$$

Where η is the internal quantum efficiency, V is the volume of the active region and υ is the frequency of incident light, and P_{in} is the power of the incident photons.

The next factor to consider is the decay of n_2. An electron will not remain in E_2 indefinitely. Instead, the electric fields from vacuum fluctuations couple to the dipole moment of the electron-hole pair and cause spontaneous emission events, where the electron relaxes down to the E_1 level, destroying the e-h pair and releasing a photon. This term is described by an Einstein coefficient A_{21} in Eq. 3.4, which is the probability per unit time that an electron will make the transition from E_2 to E_1.

$$\left(\frac{dn_2}{dt}\right) = \frac{-1}{4\pi} A_{21} n_2 \tag{3.4}$$

However, there can also be non-radiative forms of recombination, where the electron relaxes to E_1 without emitting a photon. This can be recombination at defects in the material, recombination with surface states Auger recombination, etc. For convenience and ease of experimental measurement, it is common to represent both the radiative

and non-radiative losses as lifetimes, which is done in Eq. 3.5.

$$\left(\frac{dn_2}{dt}\right) = -\frac{n_2}{\tau}$$
$$\frac{1}{\tau} = \frac{1}{\tau_{sp}} + \frac{1}{\tau_{nr}} \tag{3.5}$$

Where τ_{sp} is the spontaneous emission lifetime and τ_{nr} is the non-radiative lifetime of the carrier. Another common and equivalent representation of Eq. 3.5 is to replace n_2/τ with the polynomial $An_2 + Bn_2^2 + Cn_2^3$ where A, B and C represent defect, spontaneous and Auger recombination, respectively. Eq. 3.6 represents this.

$$\left(\frac{dn_2}{dt}\right) = -(An_2 + Bn_2^2 + Cn_2^3) \tag{3.6}$$

We will later show that the laser rate equations containing the A, B and C model can be used in order to evaluate which types of non-radiative recombination are present in a laser device. An alternative but equivalent expression for surface recombination is shown in Eq. 3.7.

$$An_2 = \frac{a_s v_s}{V} n_2 \tag{3.7}$$

Where a_s is the exposed surface area of the laser, V is the volume of the active region, and v_s is the surface recombination velocity. By fitting a laser device with the rate equation model in terms of Eq. 3.7, one can extract a surface recombination velocity, which is often quoted as a figure of merit for laser performance and is also intrinsically related to the material of the laser cavity.

The final term to consider for the carrier rate equation is gain. If the intensity of photons on the material is high enough (given Eq. 3.2 is satisfied) one can invert the population of electrons, denoted as $n_2 > n_1$. It should be noted that a two-level system

under continuous excitation will eventually reach thermal equilibrium. A Boltzmann distribution consideration yields Eq. 3.8, which dictates that $n_2 \leq n_1$.

$$\frac{n_2}{n_1} = e^{-(E_2-E_1)/kT} \tag{3.8}$$

Therefore in order to invert the electron population, one must utilize a non-equilibrium pumping mechanism of electrons into E_2.[1] In this work we will assume that electrons are pumped from E_1 into an upper energy level E_3 which instantly depopulates into E_2. Such a system is referred to as a "three-level laser system." In the case of population inversion the absorption coefficient can become negative, leading to a net increase in the number of photons in the gain material. As the number of photons in the device increases, the likelihood of a stimulated emission event also (which also decreases n_2) increases. Stimulated emission is described by an Einstein coefficient B_{21} in Eq. 3.9, which is the probability per unit time per spectral radiance of the light source that an electron will transition from E_2 to E_1 and release a photon with energy ΔE.

$$\left(\frac{dn_2}{dt}\right) = \frac{-1}{4\pi} B_{21} n_2 I(\lambda) \tag{3.9}$$

For simplicity it is more convenient to reformulate Eq. 3.9 in terms of the absorption coefficient α. One can determine how n_2 relates to gain by using the fact that the absorption is governed by the Beer-Lambert law given in Eq. 3.10.

$$X + \Delta X = X e^{\alpha l} \tag{3.10}$$

Where X is the number of photons per unit volume, α is the absorption coefficient, and

[1] There are schemes where laser oscillation can be realized without population inversion. Exciton-polariton are one example which are discussed in Section 2.2.2.

l is the length of a segment of the semiconductor. For small lengths one can make a Taylor expansion of the right hand side of Eq. 3.10 which gives Eq. 3.11.

$$X + \Delta X = X(1 + \alpha l) \tag{3.11}$$

Thus $\Delta X = X\alpha l$, and instead of dealing with the cumbersome Einstein coefficients, one can use Eq. 3.12 to relate n_2 to X.

$$\left(\frac{dn_2}{dt}\right) = \alpha X \tag{3.12}$$

Where α is a negative number. Equivalently it is common to replace α with -G (where G is a positive number), because stimulated emission only becomes a significant fraction of the overall emission when α is negative. We will discuss α in more detail later in the text, where it will serve as a motivation for quantum dots as the ideal gain medium to achieve low-threshold lasers.

Combining our equations we now arrive at Eq. 3.13, the rate equation for carriers in the semiconductor, the first of the two laser rate equations.

$$\left(\frac{dn_2}{dt}\right) = \frac{\eta P_{in}}{Vh\upsilon} - \frac{n_2}{\tau} - GX \tag{3.13}$$

Fig. 3.1 illustrates the processes of absorption, spontaneous emission and absorption which were used to derive Eq. 3.13.

3.2.2 Photon rate equation

While important factors of laser operation such as the Einstein coefficients have already been discussed, it is important to consider the rate of photon generation in addition to

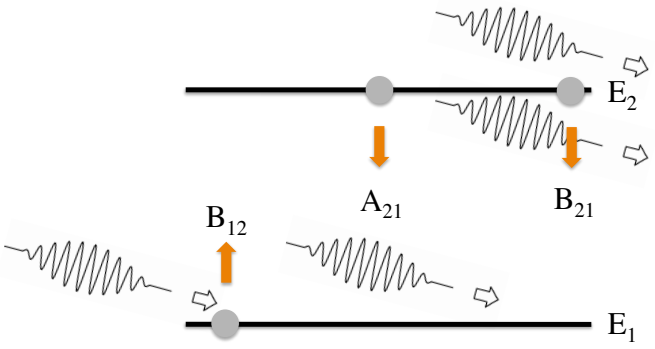

FIGURE 3.1: Schematic of photon absorption, spontaneous emission and stimulated emission denoted by B_{12}, A_{21}, and B_{21} from left to right, respectively

carrier concentration. All laser devices considered in this work operate within an optical cavity. The details related to the cavity will be discussed later, however one may consider that the cavity acts as a photon recycler. Increasing the interaction time, or effective cross section, of the photons with the gain medium greatly increases the probability of a stimulated emission event. This leads to an increase in the overall efficiency of the device.

The photons which are created by carriers which recombine via stimulated emission are the first contribution to the photon rate equations, as was discussed in Eq. 3.9. Each time a stimulated emission event occurs, an additional photon is generated. It is important to note that the volume the photon mode occupies in the cavity does not necessarily overlap entirely with the volume occupied by the gain medium. In fact, all dielectric microcavity lasers have some field which evanescently leaks out of the cavity and therefore does not interact with the gain medium. Similarly, the gain medium might not occupy the entire volume of the cavity itself. The overlap of the active region V with the volume of the optical mode V_m is known as the confinement factor Γ which has a maximum value of one and is given in Eq. 3.15.

$$\Gamma = \frac{\iiint \left|\vec{E}(\vec{r})\right|^2 \epsilon(\vec{r}) dV_{activeregion}}{\iiint \left|\vec{E}(\vec{r})\right|^2 \epsilon(\vec{r}) dV} = \frac{V}{V_m} \tag{3.14}$$

For example, Figure 3.2 is FDTD simulation of the mode profile in a GaN microdisk membrane with an active region denoted by the horizontal pink line. Here Γ is equal to the integral of the mode over the pink region divided by the total volume of the mode.

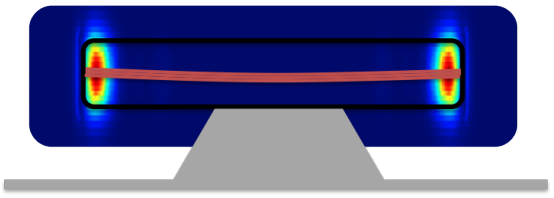

FIGURE 3.2: Side view of a GaN microdisk (outlined in black) showing that the modal volume of cavity (where red is the region of highest intensity) does not perfectly overlap with gain region (denoted in pink). Mode profile was simulated using Finite Difference Time Domain (FDTD).

For a stimulated emission event there is a one-to-one correspondence between the annihilation of an upper state electron of n_2 and the creation of a photon. Therefore we can reformulate Eq. 3.12 in terms of the rate of photon generation per unit time with an additional term representing the confinement factor. As previously described, the confinement factor is necessary in Eq. 3.15 because photons in the cavity mode have a finite overlap with the gain medium and therefore a reduced probability of triggering a stimulated emission event.

$$\left(\frac{dX}{dt}\right) = \Gamma G X \tag{3.15}$$

The next contribution to consider is that of spontaneous emission. Using Fermi's Golden Rule we know the rate at which an electron decays from E_2 to E_1 is dependent on both the spatial and spectral overlap of its dipole moment within a photon state, as demonstrated in Eq. 3.16.

$$\tau^{-1} = \frac{\left|\langle E_2|\, \vec{E}\cdot\vec{d}\,|E_1\rangle\right|^2}{\hbar^2}\rho(\omega) \tag{3.16}$$

Where τ is the spontaneous emission lifetime, $\rho(\omega)$ is the density of photon states,

$\vec{E}$ is the electric field, and $\vec{d}$ is the dipole moment of the electron-hole pair. The ability to control the spontaneous emission lifetime by modifying the density of states is critical for the realization of low-threshold lasers. This is because only the photons emitted into the desired cavity mode (the lasing mode), as opposed to other cavity modes or extended free space states, contribute to lasing. We will return to an in-depth discussion of spontaneous emission later in the text, but a principal is that the careful design of the laser cavity can tailor the density of states of the cavity mode to be much greater than other emission channels. This, in turn, increases the rate of spontaneous emission into the desired cavity mode versus other states and dramatically lowers the laser threshold. The fraction of spontaneous emission emitted into the lasing mode versus other channels is known as β, the spontaneous emission factor and is given in Eq. 3.17.

$$\beta = \frac{\tau_0^{-1}}{\tau_{sp}^{-1}} = \frac{\tau_0^{-1}}{\tau_0^{-1} + \sum\limits_{i \neq 0} \tau_i^{-1} + \tau_{ex}^{-1}} \tag{3.17}$$

Where τ_0, τ_i and τ_{ex} represent the spontaneous emission lifetimes of carriers which emit photons into the lasing mode, the i_{th} cavity mode, and into extended states, respectively. Similarly, τ_{sp} is the total spontaneous emission lifetimes, considering all pathways. When we take into account the photons which are emitted into the lasing cavity mode due to spontaneous emission one has Eq. 3.18.

$$\left(\frac{dX}{dt}\right) = \frac{\beta n_2}{\tau_{sp}} \tag{3.18}$$

One can also write Eq. 3.18 in terms of the B coefficent from Eq. 3.6.

$$\left(\frac{dX}{dt}\right) = \beta B n_2^2 \tag{3.19}$$

The final contribution arises from the loss of photons by the optical cavity. Up to this point we have considered the cavity as being perfect, that is having reflectivity equal to one. A reflectivity of unity would mean that photons would never be able to leave the cavity environment as they would always be reflected at the interface. Such a situation must be unphysical because if one were to continuously excite the system, the energy in the cavity would build up indefinitely. Furthermore, such an idealized device would be useless as it would never emit light, the principal function of a laser. While the specifics of the loss mechanism, including the directionality of the emitted light, depend highly on the cavity geometry, for now we can represent the cavity losses by a photon lifetime τ_{cav}. We will return to discuss cavity loss in more detail later in the text where we will look specifically at microdisk and photonic crystal cavity optical resonators. As an aside, it is important to note that τ_{cav} incorporates all photon loss mechanisms. Therefore material mediated absorption, commonly referred to as waveguide losses, should also be taken into account when calculating τ_{cav}. Thus the photon rate equation for cavity loss is given in Eq. 3.20.

$$\left(\frac{dX}{dt}\right) = \frac{-X}{\tau_{cav}} \tag{3.20}$$

Combining all the terms one has the photon rate equation given in Eq. 3.21.

$$\left(\frac{dX}{dt}\right) = \Gamma G X + \frac{\beta n_2}{\tau_{sp}} - \frac{X}{\tau_{cav}} \tag{3.21}$$

In the next section we will derive and examine the solution to the laser rate equations and elucidate key aspects of laser operation.

3.2.3 Solutions to the laser rate equations

In the previous sections we derived the laser rate equations for carrier and photon density, depicted by Eq. 3.22 and Eq. 3.23, respectively.

$$\left(\frac{dn_2}{dt}\right) = \frac{\eta P_{in}}{Vh\upsilon} - \frac{n_2}{\tau_{sp}} - \frac{n_2}{\tau_{nr}} - GX \tag{3.22}$$

$$\left(\frac{dX}{dt}\right) = \Gamma GX + \frac{\beta n_2}{\tau_{sp}} - \frac{X}{\tau_{cav}} \tag{3.23}$$

For clarity, both the description and units of the parameters in the laser rate equations are given in Table: 6.1.

Parameter	**Symbol**	**Units**
carrier density	n_2	$1/m^3$
photon-electron conversion efficiency	η	1
incident pump power	P_{in}	W
frequency of pump laser	ν	1/s
spontaneous emission lifetime	τ_{sp}	s
non-radiative recombination lifetime	τ_{nr}	s
gain of the active medium	G	1/s
mode confinement factor	Γ	1
cavity lifetime	τ_{cav}	s

TABLE 3.1: Definition and units of parameters in laser rate equations.

We will now solve these equations in the steady state condition $\frac{dX}{dt} = \frac{dn_2}{dt} = 0$. This condition physically corresponds to time-independent excitation of the laser device, such as through a continuous wave (CW) laser or direct current (DC) electrical injection. The first step toward solving the laser rate equations is to define the dependence of the gain (G) on the carrier density n_2. Experiments have shown a logarithmic gain dependence for the type of semiconductor material considered in this work, however it is also common to see a linear gain model used in the rate equations. The linear gain model is commonly used because it allows for a closed-form analytical solutions of the rate equations and it closely approaches the solution of the logarithmic model near the threshold. Eq.

3.24 and 3.25 are the expressions for gain, considering a linear and logarithmic model, respectively.

$$G = G_0(n_2 - n_{th}) \tag{3.24}$$

$$G = G_0 ln(\frac{n_2}{n_{th}}) \tag{3.25}$$

Where G_0 is the gain coefficient in units of $[m^3/\text{s}]$ for Eq. 3.24 or $[1/\text{s}]$ for Eq. 3.24 and n_{th} is the threshold current density in units of $[1/m^3]$. The fact that G_0 has different units depending on which model is used can lead to confusion. For linearly dependent gain, G_0 is often represented in another form where $G_0 = v_g\sigma_g$, and v_g is the group velocity [m/s] of light in the cavity and σ_g is the cross sectional area $[m^2]$ for an excited-state electron to create a stimulated emission event with a photon in the cavity. To further complicate matters, when a logarithmic model is used, the gain coefficient is also represented as $G_0 = v_g g_m$ where g_m has units of [1/m] and $g_m = \frac{\sigma_g}{V}$. When G_0 is in units of [1/s] it represents the rate of a stimulated emission event with a single electron in the cavity. As the cross section of the electron increases the gain increases. If the light is moving at a higher velocity in the cavity, it has more opportunities to scatter with any single electron in a given amount of time. Finally, the total gain in the cavity G gives us the rate of spontaneous emission events in the cavity. These must increase with the number of excited state electrons (carriers) in the cavity.

We are now able to solve for the photon number density X versus P_{in}. For convenience we define the variable $\zeta = \frac{\eta}{h\nu}$. The easiest way to solve the rate equations is slightly counterintuitive: because P_{in} is the independent variable. It is natural for one to first isolate $n_2(P_{in})$ using Eq. 3.22 and then substitute this expression into the Eq. 3.23 to find $X(P_{in})$. This can be done analytically for the approximation of a linear gain dependence, however it is not the easiest way to solve the equations and is not

extendable to situations with logarithmic gain or significant non-radiative recombination without using heavy numerical techniques. The easy way is to find X(n_2) using Eq. 3.23 and then substitute this expression into Eq. 3.22 to find $P_{in}(n_2, X)$. Once the relationsip between P_{in}, n_2 and X is known, one can then plot $X(P_{in})$. Upon carrying out this procedure one can obtain expressions for the photon density given in Eq. 3.26 and 3.27, which are for linear and logarithmic gain, respectively.

$$X = \frac{\beta B n_2^2}{\tau_{cav}^{-1} - \Gamma G_0 (n_2 - n_{th})} \tag{3.26}$$

$$X = \frac{\beta B n_2^2}{\tau_{cav}^{-1} - \Gamma G_0 ln\,(n_2/n_{th})} \tag{3.27}$$

From the denominator of Eq. 3.26 and 3.27, one can see that if X is to remain positive, which is necessary to describe our physical system, the photon generation rate from stimulated emission cannot exceed the cavity loss rate. This places a constraint on the maximum value of n_2, known as the carrier saturation density n_{sat}, given in Eq. 3.28 and Eq. 3.29 for linear and logarithmic gain, respectively.

$$n_{sat} = n_{th} + \frac{1}{\Gamma * G_0 * \tau_{cav}} \tag{3.28}$$

$$n_{sat} = n_{th} exp(1/(\Gamma * G_0 * \tau_{cav})) \tag{3.29}$$

This phenomenon is commonly known as 'population clamping' or 'gain pinning' because n_2 ceases to increase with increasing pump power and instead is clamped at the maximum values of n_{sat}. Similarly, as the gain is dependent on n_2, it also ceases to increase with pump power and instead remains at its maximum values of G(n_{sat}). For the logarithmic gain model, n_2 asymptotically approaches n_{sat} and therefore the gain G also asymptotically approaches G(n_{sat}). Physically, the effect occur because as the

photon density increases the lifetime of a carrier in an excited state will decrease, due to stimulated emission events. Eventually an equilibrium is reached in which the carrier concentration equals or asymptotically approaches n_{sat} (depending on the model) with increasing pump power. As devices in this work are analyzed using a logarithmic gain model, from this point forward we will use that formalism in the text. Figure 3.3 is a plot of the carrier density versus pump power which demonstrates that n_2 asymptotically approaches n_{sat} rather than n_{th}.

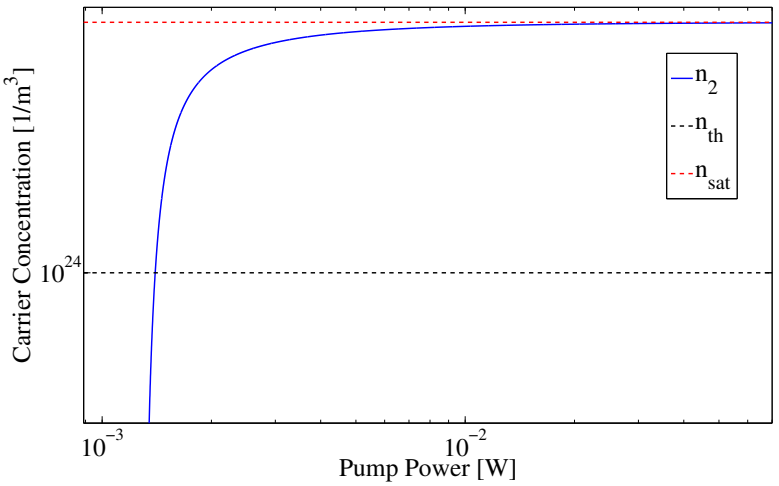

FIGURE 3.3: Log-log plot of the carrier concentration vs. laser pump power simulated using the laser rate equations

Before we introduce the solution for the photon density in the laser device, it is important that we generalize our analysis from a two-level model to a multi-level model. For most semiconductor gain media, there is a continuum of energy levels (or at least multiple discrete levels, as in the case of a QD) as opposed to just the two levels E_1 and E_2 we considered in the derivation of the laser rate equations. The multiple energy levels cause the light emission to have a spectrum of wavelengths whose limits depend on the maximum and minimum energy separation of the electrons and holes. Figure 3.4 a) and b) are representations of a semiconductor gain medium inside an optical cavity and its corresponding emission spectrum, respectively. In order to mathematically describe

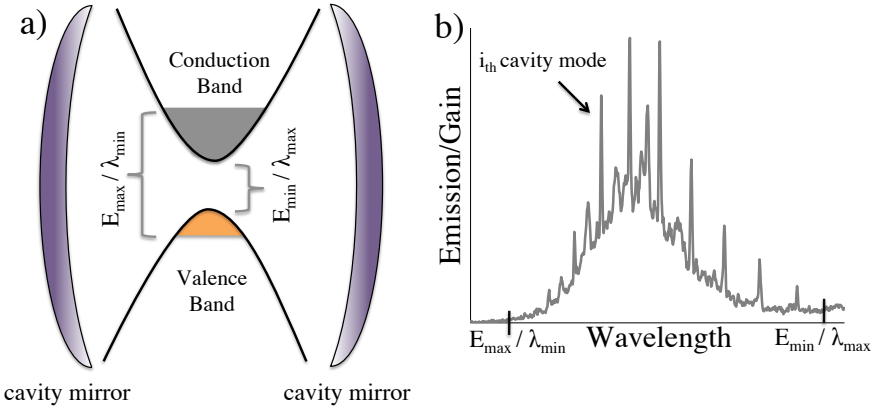

FIGURE 3.4: a) Schematic of a semiconductor gain medium inside an optical cavity. The minimum and maximum energy of the electron-hole are defined by the band edge and the fermi levels, respectively. b) representative emission spectrum from the device shown in a), one can cavity modes (sharp peaks) dressing the broadband emission spectrum.

the system in Figure 3.4, one must modify the photon rate equation to account for the multiple wavelengths of emission. Doing so produces Eq. 3.30 and Eq. 3.31, where the parameters with a λ subscript may or may not have a wavelength dependence, for any given laser device.

$$\left(\frac{dn_2}{dt}\right) = \frac{\eta P_{in}}{Vh\upsilon} - \frac{n_2}{\tau_{sp,\lambda}} - \frac{n_2}{\tau_{nr,\lambda}} - \int_{\lambda_{min}}^{\lambda_{max}} G_\lambda X_\lambda d\lambda \tag{3.30}$$

$$\left(\frac{dX_\lambda}{dt}\right) = \Gamma_\lambda G_\lambda X_\lambda + \frac{\beta_\lambda n_2}{\tau_{sp,\lambda}} - \frac{X_\lambda}{\tau_{cav,\lambda}} \tag{3.31}$$

It is important to note that the wavelength dependence of the gain and cavity lifetime plays a major role in determining which wavelength reaches the lasing condition first. In regards to gain, the maximum intensity of the emission spectrum in Fig. 3.4b) corresponds to the wavelength with the highest gain coefficient. Similarly, the sharp peaks decorating the emission spectrum correspond to cavity modes (resonances) which have the highest reflectivity and therefore longest photon lifetime τ_{cav}. We will examine the wavelength dependence in more detail shortly.

Using our modified rate equations, we arrive at Figure 3.5 and Figure 3.6 which are linear and log-log plots of the photon density of the lasing cavity mode ($\lambda = \lambda_0$) versus the incident pump power, respectively.

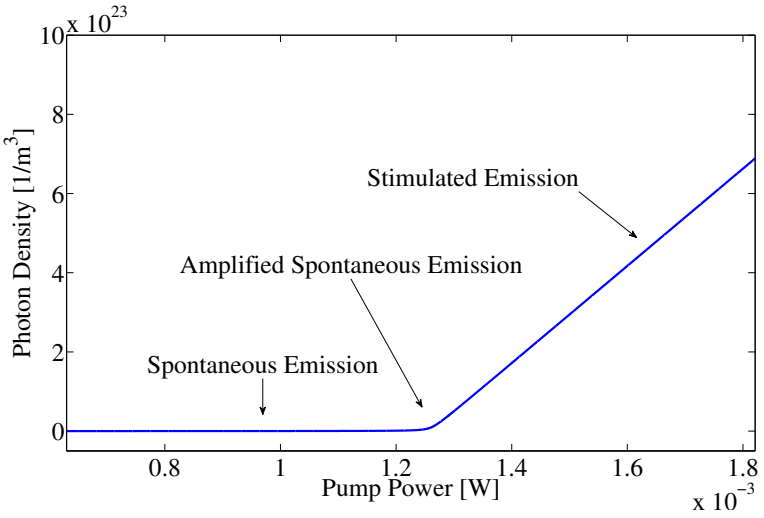

FIGURE 3.5: Light-out/light-in (L-L) lasing curve, where light-out and light-in correspond to the photon density of the lasing mode and incident pump power, respectively. The three regimes of laser operation, spontaneous emission, amplified spontaneous emission and stimulated emission dominated light output are also denoted.

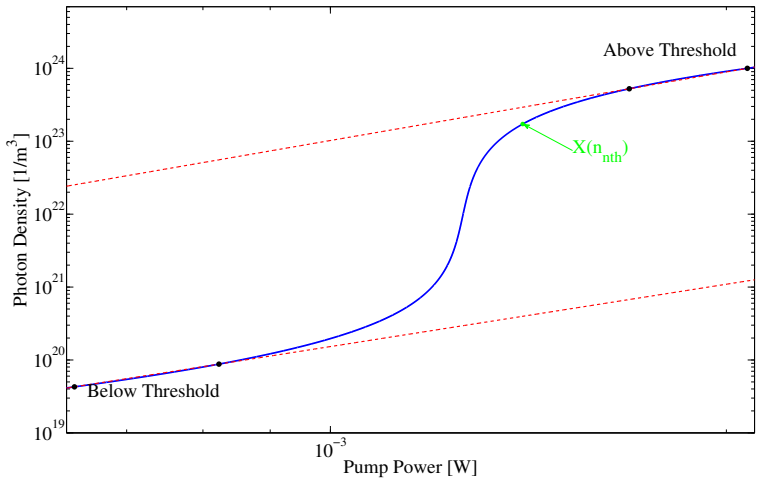

FIGURE 3.6: L-L lasing curve plotted log-log. The regions of constant slope which correspond to below and above threshold are denoted with red lines.The photon density at the threshold carrier density is also denoted, which is one commonly used definition of the lasing threshold.

From the photon density plots one can clearly identify three regimes of laser operation. The first regime is below the lasing threshold and the photon density its dominated

by spontaneous emission, which has a constant slope in the log-log plot, as expected from Eq. 3.18. As the carrier population increases with pump power, the gain increases leading to more stimulated emission events. However, as the rate of spontaneous and stimulated emission events become comparable, the device enters the second regime of laser operation known as amplified spontaneous emission (ASE).

ASE physically arrises from spontaneously emitted photons which copy themselves by triggering stimulated emission events. Because the rate of spontaneous emission is high and each spontaneously emitted photon can have a different phase and wavelength (λ), the device has a high density of stimulated emission photons which are seeded through distinct spontaneous emission events. This leads to the overall photon density in the cavity being incoherent, even though there can be local groups of coherent photons. The onset of ASE is characterized by an exponential increase in the photon population in the linear-linear plot.

Finally, as the pump power is further increased, the rate of stimulated emission becomes much higher than that of spontaneous emission. The device reaches the lasing threshold when the gain at one wavelength ($\lambda = \lambda_0$) is high enough to compensate for the cavity losses in the system at the same wavelength λ_0. In this case, both mirror and waveguide losses are incorporated into the total loss rate of the system. When this condition is met, one spontaneous emission event at λ_0 will lead to a cascade of stimulated events that causes a build up of coherent (in phase and wavelength) photons in the cavity. We will later show in this work that the wavelength in which lasing occurs is deterministic, meaning for any given laser device the wavelength with the most favorable conditions for lasing (λ_0) has the lowest lasing threshold $P_{in} = P_{th}$ and therefore always achieves the lasing condition first. We will return to this point when we consider the behavior of the laser rate equations with varying input parameters. We note as a point

of interest that at or above the lasing threshold, spontaneous and stimulated emission events at wavelengths not equal to the lasing wavelength are suppressed. This is because the rate of carrier recombination due to stimulated emission at the lasing wavelength far exceeds the rate of spontaneous or stimulated emission at other wavelengths, due to the high photon density at the lasing wavelength λ_0. The combination of the high photon density at the lasing wavelength and the suppressed emission at other wavelengths leads to a very distinct evolution of the light emission with increasing pump power for all laser devices. Figure 3.7 shows the intensity of light emission versus wavelength at three pump powers, corresponding to below, near and above the lasing threshold, for a device measured in this work.

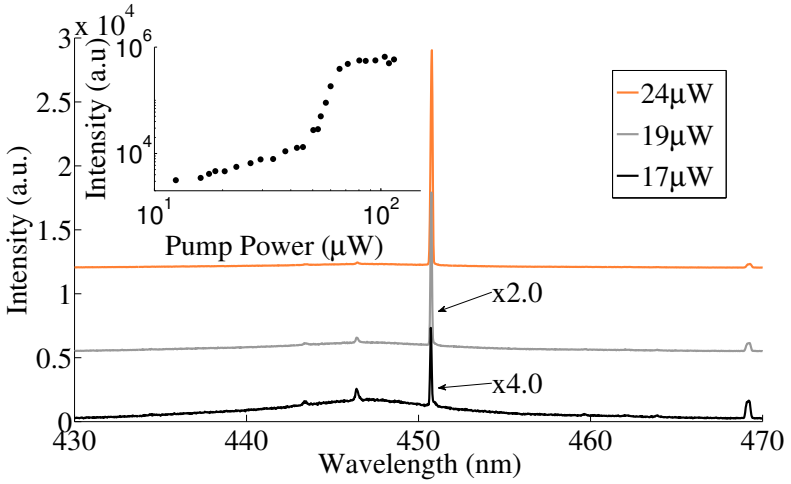

FIGURE 3.7: Light emission vs wavelength from a laser device at various pump powers. The curves are offset and scaled for clarity. The bottom, middle and top curves correspond to a device below, near and above threshold, respectively. The inset shows the intensity of the lasing mode vs pump power, plotted log-log.

We will elucidate the specific features of the device measured in Figure 4.1 in Section 6.4. However, qualitatively one can observe the main features of laser operation previously discussed. Below threshold, multiple modes are observed on top of a broadband emission spectrum. As the pump power is increased and the device approaches threshold, the intensity at all wavelengths is increased. Finally, above threshold, the

intensity of the lasing mode far surpasses the emission at any other wavelength. At this point the device emits a high density of coherent photons at the lasing wavelength. The inset of Figure 4.1 also agrees well with Figure 3.6, which further confirms that the model presented in this work adequately describes the devices we measure. We will now continue to the next section, where we will consider ways to improve laser performance by optimizing key parameters of the device.

3.3 Behavior of the laser with varying input parameters

In this section we examine which parameters can be either chosen or adjusted in order to lower a lasers' threshold. We see that the spontaneous emission factor, threshold current density and cavity lifetime play significant roles in determining a lasers' properties. Finally, we show that one can theoretically use the laser rate equations in order to infer whether the gain material is limiting a lasers' performance.

3.3.1 Varying the spontaneous emission factor

The spontaneous emission factor (β) of the lasing mode (λ_0) can assume any value between 0 and 1. Figure 4.2 is a log-log plot of lasing curves for β equals 0.001, 0.01, 0.1 and 0.8, respectively.

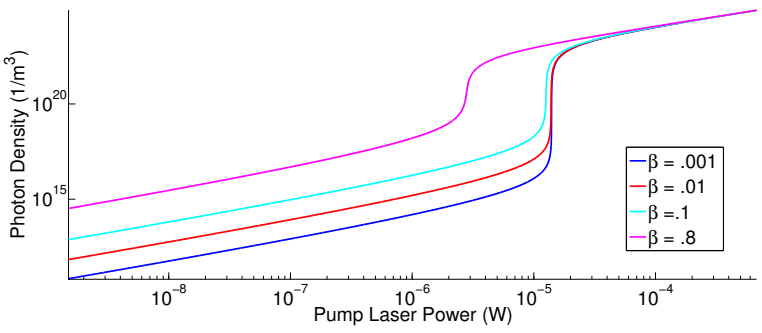

FIGURE 3.8: Lasing curves plotted over a wide range of values for β.

Looking at the below-threshold regime of operation one can see that as β_{λ_0} increases, so does the y-intercept of the lasing curve. Eq. 3.18 offers insight into the physical reason behind this trend. Below threshold, the number of spontaneously emitted photons into the lasing mode per unit time depends on the carrier density n_2, spontaneous emission lifetime (τ_{sp}), and spontaneous emission factor β_{λ_0}. The carrier density and spontaneous emission lifetime govern the total number of spontaneously emitted photons (at all wavelengths) emitted into the cavity per unit time. However, the spontaneous emission factor dictates what percentage of emitted photons are at the wavelength of the lasing mode with $\beta_{\lambda_0} = 0$ corresponding to zero photons and $\beta_{\lambda_0} = 1$ corresponding to the entirety of the emitted photons. Therefore, it makes sense that as β_{λ_0} increases, the photon density at λ_0 below threshold is higher for the same pump power because the device is more efficient at emitting photons at $\lambda = \lambda_0$. Interestingly, the lasing threshold does not appreciably change for β between 0.001 and 0.1. However, it is dramatically lowered at β equals 0.8. The reason for this can be understood by combining Eq. 3.22 and Eq. 3.23 in order to obtain an expression for the threshold pump power given in Eq. 3.32 where $P_{in} = P_{th}$ and $n_2 = n_{th}$.

$$P_{th} = \frac{Vh\nu}{\eta}\left(\frac{n_{th}}{\tau_{sp}}(\Gamma - \beta) + \frac{X_{th}}{\tau_{cav}}\right) \tag{3.32}$$

For this instance we will consider the case where Γ is equal to one. From Eq. 3.32 we see that for small β the threshold pump power depends on reaching a certain carrier density $n_2 = n_{th}$. Because the carrier concentration increases with pump power, the threshold is nearly the same for β between 0.001 and 0.1. However as β gets closer to unity, such as 0.8, the lasing threshold occurs at a fraction of n_{th}. In the limit where β equals one, the device reaches threshold a vanishly small carrier density. This behavior is known as 'thresholdless lasing' and is illustrated in Figure 4.3.

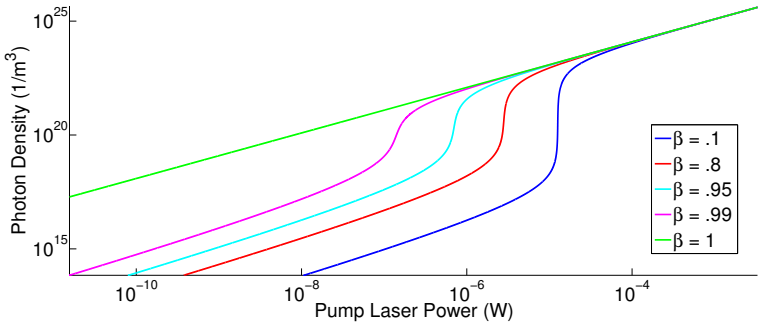

FIGURE 3.9: Lasing curves plotted over a range of values where β is close or equal to one. In the case where $\beta = 1$, the device has no lasing threshold.

While $\beta = 1$ is technically impossible to realize, the prospect of low-threshold lasing with a high beta is intriguing and has been realized in many semiconductor systems, including the GaN photonic crystal cavities presented in Chapter 7.2. We will return to consider how to design a laser device with β close to one in Chapter 4.

3.3.2 Varying the gain coefficient

Figure 3.10 is a log-log plot of lasing curves for gain coefficient G_0 equals 1e15, 5e15, 1e16, and 5e16 $1/s$, respectively. One can see that the threshold power does not decrease with increasing gain coefficient, as expected from the independence of Eq. 3.32 on G_0. Therefore the gain coefficient is not a critical parameter toward achieving low-threshold lasers.

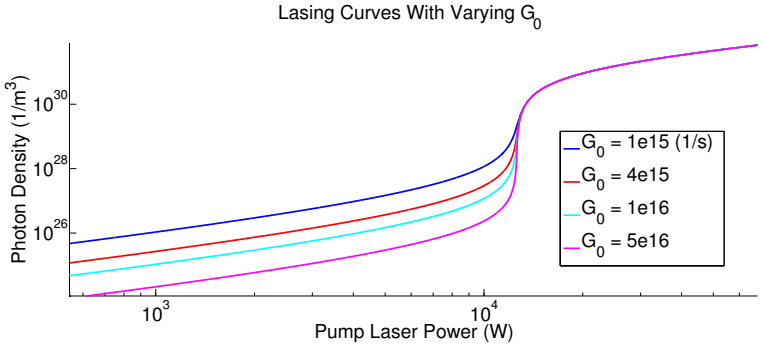

FIGURE 3.10: Lasing curves with various values of the gain coefficient G_0.

3.3.3 Varying the threshold carrier concentration

Figure 3.14 is a log-log plot of lasing curves for the threshold current density (n_{th}) equals 5e23, 1e24, 2e24 and 4e24 $1/m^3$, respectively. As expected from Eq. 3.32, the threshold lowers with decreasing values of n_{th}. It is important to note that one can not arbitrarily vary n_{th} as it relates to the electronic confinement of the gain medium. The increased localization of the electrons and holes leads to a greater probability of exciton formation and therefore photon emission. There has been a considerable amount of effort in the design and growth of gain materials with low threshold current densities. In particular quantum dots are predicted to have the lowest threshold current density of all gain materials, making them excellent candidates for low-threshold lasers. In practice, the capture efficiency of the gain medium must also be taken into account. The lower capture cross section of quantum dots compared to quantum wells can lead to a lower density of electron-hole pairs in the quantum dot, thereby increasing the overall carrier concentration for the quantum dot active layer. We will return to a more in-depth discussion of how the dimensionality of a gain medium effects n_{th} in the next section. For now we note that this parameter is critical toward realizing low-threshold lasers.

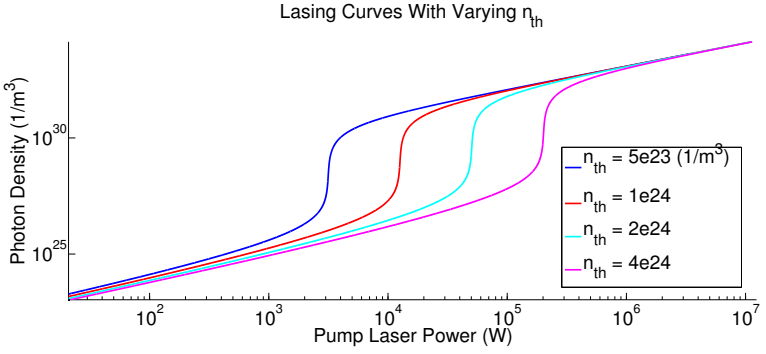

FIGURE 3.11: Lasing curves with vary values of threshold current density n_{th}.

3.3.4 Varying the spontaneous emission lifetime

Figure 4.6 is a log-log plot of lasing curves for the spontaneous emission lifetime (τ_{sp}) equals 5e-11, 1e-10, 5e-9 and 1e-9 s, respectively. One can see the lasing threshold of

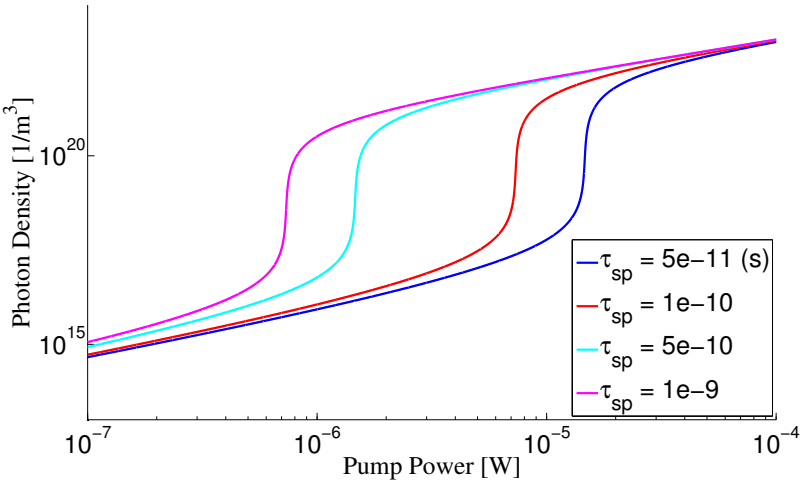

FIGURE 3.12: Lasing curves with vary values of spontaneous emission lifetime τ_{sp}

the device increases as the spontaneous emission lifetime decreases. This fact is interesting because it indicates that spontaneous emission events do not contribute towards lowering the lasing threshold, although in Section 3.3.1 we will see that increasing the fraction of spontaneous emission into the lasing mode lowered the lasing threshold. In the extreme case that the spontaneous emission lifetime was very long, there would be no spontaneously emitted photons in the cavity, thus the photon density would remain low below threshold. The correct interpretation is that spontaneous emission events are not desired because they steal carriers that would have undergone stimulated emission events. As discussed previously, the critical parameter towards achieving laser threshold is inverting the electron population, not achieving a high-photon density. In fact, certain laser devices such as Quantum Cascade Lasers (QCLs) have non-radiative lifetimes which are orders of magnitude shorter than spontaneous emission lifetimes. Therefore,

they emit almost no photons before the threshold condition is reached. Once the inversion condition is satisfied, it only takes a single spontaneous emission event to trigger a vast amount of stimulated emission events. Unfortunately, the spontaneous emission lifetime is often not engineered to be long as the gain medium is usually optimized for the wavelength of emission or other desirable properties for laser operation. However, the qualitative behavior of the laser device with varying spontaneous emission lifetime will serve as an intuitive framework in which we might better understand how the cavity volume affects the lasing threshold.

3.3.5 Varying the cavity volume

Figure 4.4 is a log-log plot of lasing curves for the cavity volume (V) equals 1e-21, 1e-20, 1e-19, and 1e-18 m^3, respectively.

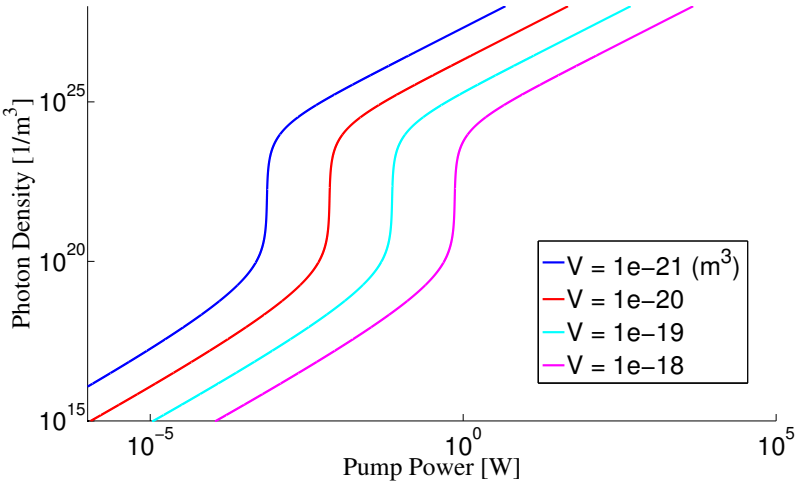

FIGURE 3.13: Lasing curves with vary values of V

As expected from Eq. 3.32, the threshold decreases linearly as the cavity volume is reduced. A smaller cavity volume lowers a devices lasing threshold, due to the density

of states in vacuum, which is given in Eq. 3.33.

$$\rho(\omega) = \frac{\omega^2 V}{\pi^2 c^3} \tag{3.33}$$

Where V is the volume of space considered, ω is optical frequency, and c is the speed of light. From Eq. 3.16, we know that the rate of spontaneous emission is proportional to the density of states. From the previous discussion in Section 3.3.4 of how a short spontaneous emission lifetime increases the lasing threshold, it logically follows that small cavity volumes are favorable for low-threshold lasing. Simply, this is equivalent to the fact that a high field strength confined to a small volume is more effective in inducing exciton transitions. The desire for small modal volume cavites has led to the design and fabrication of novel optical cavities with volumes as low as one wavelength cubed. We will follow up with a more in-depth discussion of low modal volume optical cavities in Chapter 4.

3.3.6 Varying the A and C coefficients

We now arrive at a point of interest regarding the behavior of the rate equations when contributions from linear recombination (A) and Auger recombination (C) are included. From Eq. 3.6, we know that the linear recombination, spontaneous emission and Auger recombination scale as n_2, n_2^2, and n_2^3 respectively. Auger recombination scales as the carrier density to the third power because it is a three particle process where an electron-hole pair non-radiatively recombine and transfer their energy to a third electron in the conduction band. This process is schematically demonstrated in Figure 3.14.

Therefore, it is natural to expect the slope of the lasing curve below threshold to vary depending on which phenomena are dominant. This is indeed the case, as can be

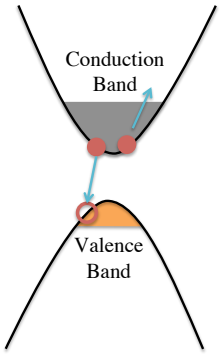

FIGURE 3.14: Schematic of Auger recombination. An electron-hole pair recombines and transfers energy to a third electron.

seen in Figure 3.15.

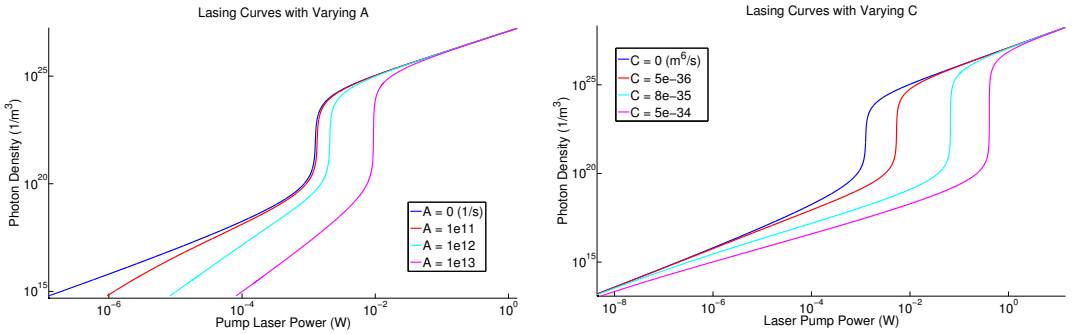

(a) Lasing curves with vary values of the A coefficient. (b) Lasing curves with vary values of the C coefficient.

FIGURE 3.15

It is apparent that from a graph of the lasing threshold versus the below threshold slope, one could infer if either linear or Auger recombination was limiting device performance. While this might seem obscure, certain material systems such as the nitrides experience degraded device performance in LEDs (often referred to as droop) which has recently been attributed to Auger recombination [90]. Conventional measurement techniques of non-radiative recombination are arduous, however the unique coupling between the gain medium and optical cavity within a laser serve as a platform to investigate material properties through optical measurements. Figure 3.16 is a plot of the lasing threshold versus the slope of the lasing curve below threshold.

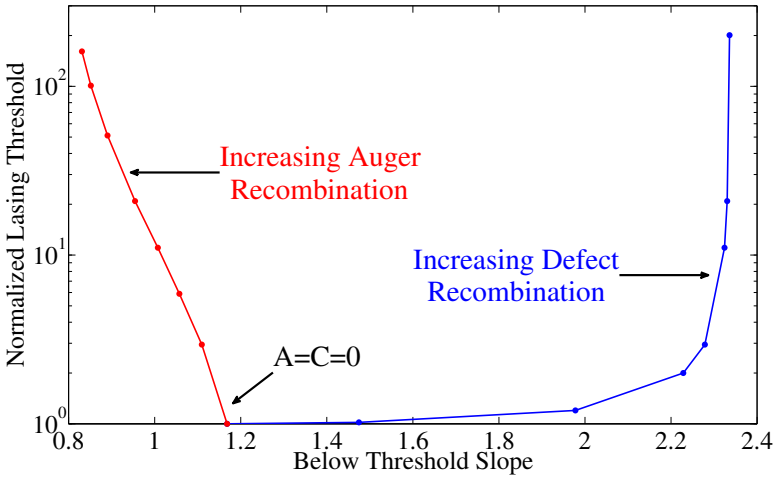

FIGURE 3.16: Semilog plot of the lasing threshold (normalized to no nonraditative recombination) versus the below threshold slope of the pump power versus photon density curve. A and C coefficients vary from 0 to 1e14 s^{-1} and 8e-35 m^6/s, respectively.

From Figure 3.16, one can see that the rate the lasing threshold increases is faster, at smaller deviations in the slope from A=C=0, for Auger recombination than linear recombination. This is to be expected as the C and A coefficients scale as the third and first order of the carrier concentration, respectively. In order to practically realize such an experiment, one would have to measure laser devices with varying values of A and or C. This could be done by engineering the defect density, impurity concentration between sample wafers, or implementing micron sized cavity devices in order to exploit the natural material inhomogeneities within one semiconductor wafer. Therefore the microcavity lasers can be used as a sensitive probe of the material properties, however for low-threshold lasing Auger recombination should be avoided and instead cavities should be engineered to be optically efficient.

3.4 A laser device with optimized parameters

From Section 8.2, we found that one can lower lasing thresholds by creating a device with a high spontaneous emission factor (β), low threshold current density (n_{th}), and

small cavity volume (V). In this section we investigate how to realize a laser device that exhibits such optimized parameters. Specifically, in Chapters 4 and 5 we will demonstrate that semiconductor quantum dots within a low modal volume microdisk or photonic crystal cavity fulfill such criteria and are therefore ideal candidates for low threshold lasers.

3.4.1 Optical cavity design

In this section we return to first principles in order to gain insight into what properties an optical cavity must have in order to possess a high spontaneous emission factor (β). Recalling our previous expression for β from Eq. 3.17, we now consider the density of states of an optical cavity mode in order to determine the spontaneous emission lifetime of the lasing mode (τ_0). Before doing so, we utilize the power of hindsight and divide the numerator and denominator of Eq. 3.17 by the spontaneous emission rate in free space (τ_{fs}^{-1}) in order to arrive at Eq. 3.34. This will ultimately help us formulate β in terms of the Purcell Factor, ubiquitous in light-matter coupling.

$$\beta = \frac{\tau_0^{-1}/\tau_{fs}^{-1}}{\tau_{sp}^{-1}/\tau_{fs}^{-1}} = \frac{\tau_0^{-1}/\tau_{fs}^{-1}}{(\tau_0^{-1} + \sum_{i\neq 0} \tau_i^{-1} + \tau_{ex}^{-1})/\tau_{fs}^{-1}} \tag{3.34}$$

Solving for τ_{fs}^{-1} to obtain β, we arrive at Eq. 3.35.

$$\tau_{fs}^{-1} = \frac{\left|\langle E_2|\, \vec{E}_{vac} \cdot \vec{d}\, |E_1\rangle\right|^2}{\hbar^2} \rho_{fs}(\omega_0) \tag{3.35}$$

Where the density of states in free space $\rho_{fs}(\omega_0)$ is given by Eq. 3.33 and the electric field of vacuum $\vec{E}_{vac}$ is derived using the equipartiton theorem and the quantum field theory (QFT) formalism that each point in space can be approximated as a harmonic

oscillator with energy $\hbar\omega/2$.

$$2\int \frac{\epsilon_0}{2}\vec{E}_{vac}^2 dV = \frac{\hbar\omega_0}{2} \tag{3.36}$$

$$\left|\vec{E}_{vac}\right| = \sqrt{\frac{\hbar\omega_0}{2\epsilon_0 V}} \tag{3.37}$$

Inserting $\rho_{fs}(\omega_0)$ and $\vec{E}_{vac}$ back into Eq. 3.35 and integrating over all possible dipole orientations where $\vec{d} = |d|\,cos(\theta)$ one has Eq. 3.38.

$$\tau_{fs}^{-1} = \frac{1}{4\pi\hbar^2}\int_0^{2\pi}\int_0^{\pi}\left|\vec{E}_{vac}\right|^2\left|\vec{d}\right|^2\rho_{fs}(\omega_0)cos^2(\theta)sin(\theta)d\theta d\phi = \frac{1}{\hbar^2}(\frac{\hbar\left|\vec{d}\right|^2\omega_0}{3\cdot 2\epsilon_0 V})(\frac{\omega_0^2 V}{\pi^2 c^3}) = \frac{\omega_0^3\left|\vec{d}\right|^2}{6\hbar\pi^2\epsilon_0 c^3} \tag{3.38}$$

Modifying Eq. 3.16 we arrive at the expression for τ_0 in Eq. 3.40.

$$\tau_0^{-1} = \frac{\left|\langle E_2|\,\vec{E}_0\cdot\vec{d}\,|E_1\rangle\right|^2}{\hbar^2}\rho(\omega_0) \tag{3.39}$$

$$\tau_0^{-1} = \frac{\left|\langle E_2|\,\vec{E}_0\cdot\vec{d}\,|E_1\rangle\right|^2}{\hbar^2}\frac{2\Delta\omega_c^2}{\pi\Delta\omega_c(4(\omega_0-\omega_c)^2+\Delta\omega_c^2)} \tag{3.40}$$

Where $\rho(\omega_0)$ is the density of states of a lorentzian oscillator which describes the optical cavity resonance with frequency and full width at half maximum (FWHM) of ω_c and $\Delta\omega_c$, respectively. Finally, $\omega_0 \equiv (E_2 - E_1)/\hbar$ corresponds to the frequency of the light emission. Upon simplification, the inner product term reduces to Eq. 3.41.

$$\left|\langle E_2|\,\vec{E}_0\cdot\vec{d}\,|E_1\rangle\right|^2 = \left(\frac{\left|\vec{E}_0\cdot\vec{d}\right|}{\left|\vec{E}_0\right|\left|\vec{d}\right|}\right)^2\left|\vec{E_{vac}}\right|^2\left|\vec{d}\right|^2 \tag{3.41}$$

Inserting Eq. 3.41 into Eq. 3.40 and simplifying, one has Eq. 3.42.

$$\tau_0^{-1} = \left(\frac{\left|\vec{E}_0\cdot\vec{d}\right|}{\left|\vec{E}_0\right|\left|\vec{d}\right|}\right)^2\left|\vec{d}\right|^2\frac{Q}{\hbar\pi V\epsilon_0}\frac{\Delta\omega_c^2}{(4(\omega_0-\omega_c)^2+\Delta\omega_c^2)} \tag{3.42}$$

$Q \equiv \omega_c/\Delta\omega_c = \tau_c\omega_c$ is known as the quality factor of the cavity, where τ_c is the cavity photon lifetime used previously in Eq. 3.20. Taking the ratio of τ_0^{-1} and τ_{fs}^{-1}, we arrive at Eq. 3.43, which is commonly known as the Purcell factor F.

$$F = \frac{\tau_0^{-1}}{\tau_{fs}^{-1}} = \left(\frac{\left|\vec{E_0} \cdot \vec{d}\right|}{\left|\vec{E_0}\right| \left|\vec{d}\right|} \right)^2 \frac{6Q\pi c^3}{V\omega_0^3} \frac{\Delta\omega_c^2}{(4(\omega_0 - \omega_c)^2 + \Delta\omega_c^2)} \tag{3.43}$$

Simplifying using the relationship $\frac{c}{\omega_0} = \frac{\lambda}{2\pi n}$, where λ_0 is the wavelength of cavity mode and n is the index of refraction one arrives at Eq. 3.44.

$$F = \frac{\tau_0^{-1}}{\tau_{fs}^{-1}} = \left(\frac{\left|\vec{E_0} \cdot \vec{d}\right|}{\left|\vec{E_0}\right| \left|\vec{d}\right|} \right)^2 \frac{3Q\lambda_0^3}{4\pi^2 V n^3} \frac{\Delta\omega_c^2}{(4(\omega_0 - \omega_c)^2 + \Delta\omega_c^2)} \tag{3.44}$$

Inserting Eq. 3.44 into Eq. 3.34, one has our final expression for β in Eq. 3.45.

$$\beta = \frac{F}{F + \xi} \tag{3.45}$$

Where $\xi = (\sum_{i \neq 0} \tau_i^{-1} + \tau_{ex}^{-1})/\tau_{fs}^{-1}$, represents spontaneous emission into optical pathways other than the lasing mode. There are many interesting points to note from Eq. 3.45. First, being that there are two ways to maximize β. β approaches unity when F is much greater than ξ or when ξ goes to zero. It is therefore desirable for low threshold lasers to have a high Purcell factor, bringing us to a key point of this work. From Eq. 3.44, one can see that the Purcell factor increases for high quality factor (Q), low modal volume (V) optical cavities. The desire for high Q and low V cavities serves as the guiding principle for cavity design in this work. Furthermore, in order to maximize the light-matter interaction, the cavity should be both spatially and spectrally matched to the emitter. Finally, by utilizing exotic optical cavities such as photonic crystal defects, one can engineer ξ to be small by designing the density of states to be vanishingly low

for the non-lasing modes. In Chapter 4 we introduce the theoretical principles behind microdisk and photonic crystal cavities to elucidate how one can actually design a high β cavity.

Chapter 4

Microcavity Resonators

4.1 Microdisk cavities

The results presented in this thesis were primarily obtained with microdisk resonators. As with all systems there are inherent advantages and disadvantages to microdisks. The main advantage is the existence of high Q low V cavity modes that can span over the entire gain region. This comes at cost, as with multiple modes there are more radiative pathways other than the lasing mode and therefore β is not as high as in other optical cavities. In spite of this, microdisks serve as excellent diagnostic devices for emerging semiconductor gain media and have been demonstrated as high-performance low-threshold lasers.

In this section we derive the optical resonances of a microdisk from first principles and demonstrate how the structure serves as a high Q and low V optical cavity. Figure 4.6 shows the cylindrical coordinates ($\hat{\rho}$,$\hat{\phi}$,$\hat{z}$) for the microdisk with radius R, height h and transverse electric TM, as well as transverse electric TE directions denoted.

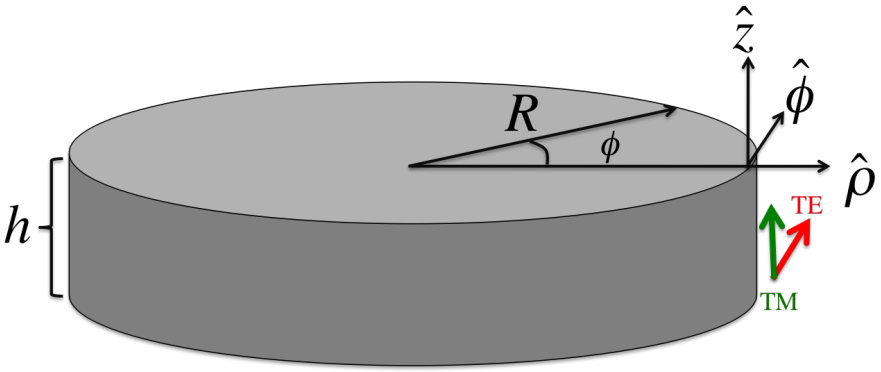

FIGURE 4.1: Microdisk with the coordinates system, dimensions and polarization denoted.

We begin with a ray optics model which offers some physical intuition for how a microdisk confines light. Light is confined within the boundary of a microdisk via the phenomenon of total internal reflection (TIR). It is well known that for light incident at an interface between two media with indices of refraction n_1 and n_2 (where $n_1 > n_2$), that above a critical angle θ_c the ray can undergo TIR and therefore remain confined to the medium with index n_1. From Snell's law the critical angle is defined by Eq. 4.1.

$$\theta_c = sin^{-1}(n_2/n_1) \tag{4.1}$$

Using geometry, one can show that for a ray originating from inside a circle that is incident upon its boundary at an angle θ, all subsequent reflections will also be incident upon the circle with angle θ. Therefore a ray that satisfies the TIR condition ($\theta > \theta_c$) for the first reflection off the boundary of a circle will continue to do so for all subsequent reflections. Such modes are known as Whispering Gallery Modes (WGM). Figure 4.2 shows an example of a source located inside the periphery of a microdisk. which emits rays in 360 degrees, at intervals of 6 degrees. Most of the rays originating from the source undergo partial reflection and refraction at the interface.However there are a range of angles with which all rays are totally internally reflected. The TIR reflected rays are denoted in red and the subsequent 20 bounces from each ray are denoted in gray.

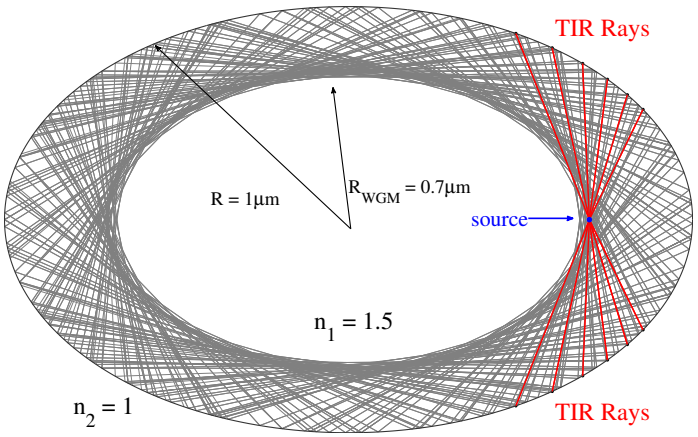

FIGURE 4.2: Ray optics simulation of a whispering gallery mode inside a one micron microdisk resonator with index 1.5 in air. Rays originating from the source (blue dot) which are totally internally reflected are denoted in red. The 20 subsequent reflections for each ray are denoted in gray.

One can see from Figure 4.2 that the totally internally reflected rays are confined to the periphery of the disk (300nm from the edge), giving rise to a high-field intensity also located near the edge of the disk. One can only satisfy the TIR condition for a source that is placed within 300nm from the edge of the disk (within the gray rays). In order to couple into a WGM, the source must be located near the periphery. One would expect that by increasing the index of refraction of the microdisk that the critical angle would decrease thereby increasing the number of rays from the source which are totally internally reflected. Figure 4.3 is a simulation for a microdisk of $n_1 = 2.5$ which demonstrates that this is indeed the case.

Now that we have gained some physical intuition for how light is confined within a microdisk we pause to consider some limitations with the ray optics model. The first problem is that in the simplified ray optics model the light emitted into the WGM is confined within the disk indefinitely. This cannot be true as the device would build up an infinite power density if the source emitted continuously. In fact, the device does not confine light indefinitely because light has a spatial extent and is therefore not infinitely

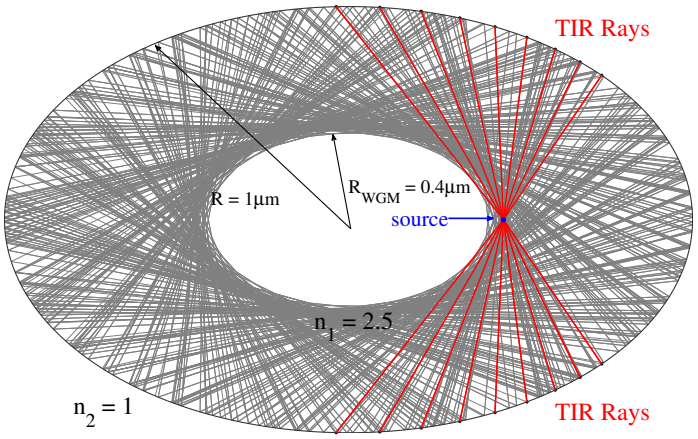

FIGURE 4.3: Ray optics simulation with the same conditions as in Fig. 4.2 except for the index of refraction of the disk which is increased to $n_1 = 2.5$. One can see the number of TIR rays has increased, due to the lower critical angle.

thin, as assumed with ray optics. In turn, this causes the perimeter of the disk to not be locally flat but curved, modifying the total internal reflection condition for light. This happens because certain wave vectors of a photon wave packet now violate $\theta > \theta_c$ and therefore escape from the disk. Furthermore, ray optics contain no information regarding the phase of the light, leading to an absence of frequency dependent resonances and accurate intensity profiles of modes. Finally, there is no polarization dependence for light rays satisfying the TIR condition, therefore one cannot distinguish between TE and TM modes. For all of the above reasons it is best to solve for the mode profile of light within a microdisk using Maxwell's equations. Such analysis will not only qualitatively agree with our ray optics approach but also offer additional insight into the behavior of light confined within the microdisk.

We begin with the Maxwell equations in the absence of sources or currents and assume the electric field and magnetic field are oscillatory in time and therefore obey the relation $\vec{E}(\vec{r},t) = E(\vec{r})e^{-i\omega t}$ and $\vec{H}(\vec{r},t) = H(\vec{r})e^{-i\omega t}$. Therefore the Maxwell equations

take the form of Eq. 4.2.

$$\begin{aligned} \nabla \cdot \vec{H}(\vec{r}) = 0 \qquad \nabla \times \vec{E}(\vec{r}) - i\omega\mu_0 \vec{H}(\vec{r}) = 0 \\ \nabla \cdot (\epsilon(\vec{r})\vec{E}(\vec{r})) = 0 \qquad \nabla \times \vec{H}(\vec{r}) + i\omega\epsilon_0\epsilon(\vec{r})\vec{E}(\vec{r}) = 0 \end{aligned} \tag{4.2}$$

We can now combine the equations in Eq. 4.2 in order to have an expression only in terms of the electric or magnetic field, depending on what is preferred. Doing so for the magnetic field yields Eq. 4.3.

$$\nabla \times \left(\frac{1}{\epsilon(\vec{r})} \nabla \times \vec{H}(\vec{r}) \right) = \left(\frac{\omega}{c} \right)^2 \vec{H}(\vec{r}) \tag{4.3}$$

Using the vector identify $\nabla \times (\nabla \times \vec{A}) = \nabla(\nabla \cdot \vec{A}) - \nabla^2 \vec{A}$, one arrives at the Helmholtz equation in Eq. 4.4. This is the same regardless if the electric or magnetic fields are isolated from the Maxwell equations.

$$\begin{aligned} \nabla^2 \vec{H}(\vec{r}) + k^2 \vec{H}(\vec{r}) = 0 \\ \nabla^2 \vec{E}(\vec{r}) + k^2 \vec{E}(\vec{r}) = 0 \end{aligned} \tag{4.4}$$

Where $k^2 = (n(\vec{r})\omega/c)^2$. To solve for the field we now must insert the Laplacian operator in cylindrical coordinates. We must also seperate variables such that $\vec{H}(\vec{r}) = R(\rho)\Phi(\phi)Z(z)$ we arrive at Eq. 4.5.

$$\frac{1}{R(\rho)} \{ \rho^2 \frac{\partial^2 R(\rho)}{\partial \rho^2} + \rho \frac{\partial R(\rho)}{\partial \rho} \} + \frac{1}{\Phi(\phi)} \frac{\partial^2 \Phi(\phi)}{\partial \phi^2} + \frac{\rho^2}{Z(z)} \frac{\partial^2 Z(z)}{\partial z^2} + k^2 = 0 \tag{4.5}$$

Any solution to Eq. 4.5 must have the ρ, ϕ and z differentials be equal to constants. If we let the ϕ and z differentials be equal to $-l^2$ and $-\beta^2$ respectively (where β has no

relation to the previously used spontaneous emission factor) one arrives at Eq. 4.6.

$$\rho^2\frac{\partial^2 R(\rho)}{\partial\rho^2}+\rho\frac{\partial R(\rho)}{\partial\rho}+\{\rho^2(k^2-\beta^2)-l^2\}R(\rho)=0 \tag{4.6}$$

Applying the change of variable $\rho\rightarrow\rho\sqrt{k^2-\beta^2}$ one arrives at Eq. 4.7 which is Bessel's differential equation, whose solutions are Bessel functions of order l if $k^2-\beta^2>0$ and Hankel functions of order l if $k^2-\beta^2<0$.

$$\rho^2\frac{\partial^2 R(\rho)}{\partial\rho^2}+\rho\frac{\partial R(\rho)}{\partial\rho}+(\rho^2-l^2)R(\rho)=0 \tag{4.7}$$

$\vec{H}(\vec{r})$ therefore assumes the form of Eq. 4.8 where Bessel functions are solutions within the radius of the disk as they are finite valued at $\rho=0$ and Hankel functions are solutions outside the radius of the disk as they approach asymptotically approach 0 at $\rho\rightarrow\infty$.

$$\begin{aligned}\vec{H}(\vec{r})&=J_l^1(\rho\sqrt{k^2-\beta^2})e^{\pm il\phi}e^{\pm i\beta z}, &\quad \rho\leq r\\ \vec{H}(\vec{r})&=H_l^1(\rho\sqrt{k^2-\beta^2})e^{\pm il\phi}e^{\pm i\beta z}, &\quad \rho>r\end{aligned} \tag{4.8}$$

The final step to find the fields inside and outside the disk is to match boundary conditions at the surface of the microdisk. We begin with the $\hat{z}$ component of the electric and magnetic fields at the upper boundary of the disk $z=h/2$. Since we want a general solution for both the magnetic and electric fields, which are related by a spatial derivative in 1 dimension, we seek to make the normal component of the displacement field, as well as its derivative, continuous at $z=h/2$ in order to avoid divergences of the magnetic field. Before doing so, we first make the assumption that the height of the disk is small enough in the vertical direction so that only one half wavelength can fit inside. In other words we assume $Z(z)=cos(\beta_1 z)$ for $z\leq h/2$. We also assume that the field outside the disk must be exponentially decaying as we are only considering solutions in which

TIR in the z direction within the disk. This mathematically equates to $Z(z) = e^{-\beta_2 z}$ for $z > h/2$. Calculating the field and its derivative at the boundaries we arrive at Eq. 4.9.

$$\begin{aligned} \epsilon_1 A_1 cos(\frac{\beta_1 h}{2}) &= \epsilon_2 A_2 e^{\frac{-\beta_2 h}{2}} \\ \epsilon_1 A_1 \beta_1 sin(\frac{\beta_1 h}{2}) &= \epsilon_2 A_2 \beta_2 e^{\frac{-\beta_2 h}{2}} \end{aligned} \tag{4.9}$$

Where A_1, A_2, correspond to the amplitude of the field inside and outside the disk respectively. Dividing the 2nd equation by the 1st and simplifying, one arrives at Eq. 4.10.

$$\beta_1 tan(\frac{\beta_1 h}{2}) = \beta_2 \tag{4.10}$$

Interestingly, this condition is reminiscent of the finite potential well in quantum mechanics. In fact, one can reformulate our electromagnetic differential equation in terms of a quantum wave function in an arbitrary potential. We will return to this point in more detail shortly. For now, we can further simplify Eq. 4.10 by inserting the values for β_1 and β_2. β is often expressed in terms of an effective mode index $\bar{n}$ which is given in Eq. 4.11.

$$\begin{aligned} \beta^2 &= k^2 - k_0 \bar{n}^2 \\ \bar{n} &= \frac{\int_V \epsilon(\vec{r}) \left|\vec{E}(\vec{r})\right|^2 dV}{\int_V \left|\vec{E}(\vec{r})\right|^2 dV} \end{aligned} \tag{4.11}$$

Where $k = k_0 n$, and n is the index of refraction. Therefore $\beta_1 = k_0\sqrt{n_1^2 - \bar{n}^2}$ and $\beta_2 = k_0\sqrt{\bar{n}^2 - 1}$ which transforms Eq. 4.10 into Eq. 4.12.

$$\sqrt{n_1^2 - \bar{n}^2} tan(\frac{h k_0}{2}\sqrt{n_1^2 - \bar{n}^2}) = \sqrt{\bar{n}^2 - 1} \tag{4.12}$$

We now apply a similar procedure to the $\hat{\rho}$ direction and noting that $2\frac{\partial J_n(x)}{\partial x} = J_{n-1}(x) - J_{n+1}(x)$ and $\frac{\partial H_n(x)}{\partial x} = \frac{nH_n(x)}{x} - H_{n+1}(x)$ one arrives at Eq. 4.13

$$\left(\frac{J_{l+1}(Rk_0\bar{n})}{J_l(Rk_0\bar{n})} - \frac{l}{Rk_0\bar{n}}\right) = -\left(\frac{n_0}{\bar{n}}\right)\left(\frac{H_{l+1}(Rk_0n_2)}{H_l(Rk_0n_2)} + \frac{l}{Rk_0\bar{n}}\right) \tag{4.13}$$

Where Eq. 4.12 and Eq. 4.13 are for TE modes, for TM modes the right hand side of both equations should be multiplied by $(\frac{\bar{n}}{n_2})^2$. The solution to the transcendental equation in Eq. 4.13 is straightforward, but computationally heavy as one must sweep over the wavenumber (k_0) for each mode of quantum number l. Figure 4.4 shows an example of a TE polarized WGM solution to the Helmholtz equation. This was obtained using the procedure outlined above next to a Finite Difference Time Domain (FDTD) simulation which numerically solves the Maxwell's equations over space and time. This mode is referred to as a first order whispering gallery mode because it has only one maximum in the radial direction. The agreement between the two plots suggests that our mathematical formulation adequately describes our microdisk resonators.

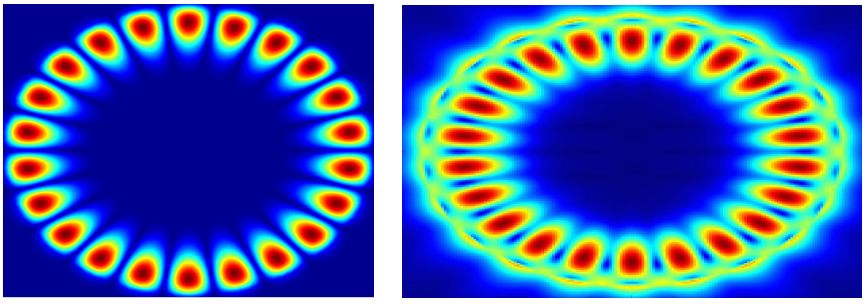

(a) Helmholtz wave equation solution (b) FDTD simulation

FIGURE 4.4: Comparison between the numerically computed WGM and FDTD simulation. Both qualitatively agree with the ray optics solution but offer additional insight into the field distribution of the mode.

We also note that the azimuthal solution offers a method to calculate the free spectral range (FSR) of the WGM modes. In order to be a standing wave in the azimuthal direction, the wave must repeat itself upon one round trip around the circle. This

imposes a restriction on the spacing in optical frequency between two modes, as given in Eq. 4.14.

$$\Delta\nu = \frac{1}{\Delta t} = \frac{c}{2\pi Rn} \tag{4.14}$$

Where c is the speed of light in vacuum, R is the radius of the disk, and n is the index of refraction of the cavity membrane. Converting to wavelength and using the chain rule one has the expression given in Eq. 4.15.

$$\Delta\lambda = \Delta\left(\frac{c}{\nu}\right) = \frac{c\Delta\nu}{\nu^2} = \frac{c^2}{2\pi Rn\nu^2} = \frac{\lambda^2}{2\pi nR} \tag{4.15}$$

Figure 4.5 is a plot demonstrating the FSR of an optical resonator. The frequency spacing between modes increases as the radius of the disk decreases. This is critically important for low-threshold lasers as reducing the number of modes increases the spontaneous emission factor of a laser via a reduction in the ξ factor in Eq. 3.45.

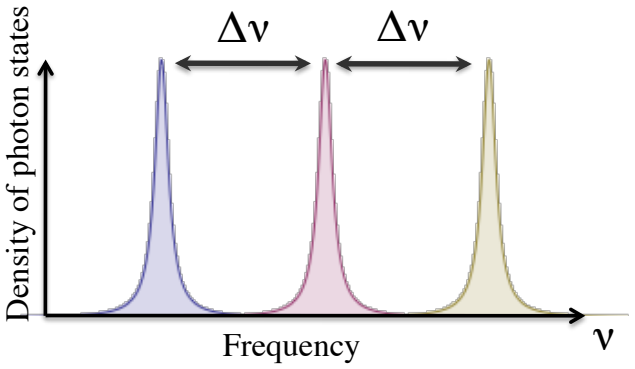

FIGURE 4.5: Schematic with the FSR ($\Delta\nu$) of cavity resonances denoted. For low-threshold lasers a high FSR is desired which requires the microdisk radius and therefore modal volume to be small

We conclude our discussion of microdisk resonators by returning to a previously mentioned point, that the electromagnetic Helmholtz equation can be reformulated in terms of a wave function Ψ in an effective potential U_{eff}. This offers insight into why

light escapes from the disk. For a more detailed discussion of the effective potential formalism see [91]. We begin with Schrodinger's Equation in Eq. 4.16 where $E = \frac{\hbar^2 k_0^2}{2M}$.

$$\{-\frac{\hbar^2}{2M}\Delta + U_{eff}\}\Psi(r) = E\Psi(r) \tag{4.16}$$

On can now rearrange our radial differential equation given in Eq. 4.17.

$$\frac{\partial^2\Psi(\rho)}{\partial\rho^2} + \frac{1}{\rho}\frac{\partial\Psi(\rho)}{\partial\rho} + (k_0^2\bar{n}^2 - \frac{l^2}{\rho^2})\Psi(\rho) = 0 \tag{4.17}$$

We multiply by $-\frac{\hbar^2}{2M}$ and add $\frac{\hbar^2 k_0^2}{2M}\Psi(\rho)$ to both the left and right hand side of Eq. 4.17 which allows us to solve for U_{eff}.

$$\begin{aligned} \frac{-\hbar^2}{2M}\{\frac{\partial^2\Psi(\rho)}{\partial\rho^2} + \frac{1}{\rho}\frac{\partial\Psi(\rho)}{\partial\rho}\} + \frac{-\hbar^2}{2M}\{(-k_0^2 + k_0^2\bar{n}^2 - \frac{l^2}{\rho^2})\}\Psi(\rho) &= \frac{\hbar^2 k_0^2}{2M}\Psi(\rho) \\ U_{eff} &= \frac{\hbar^2}{2M}\{k_0^2(1-\bar{n}^2) + \frac{l^2}{\rho^2}\} \end{aligned} \tag{4.18}$$

Figure 4.6 shows U_{eff} as well $\Psi(\rho)$, which is the solution to Eq. 4.18 for $R = 10\mu m$, $n_1 = 1.4$, $n_2 = 1$, where $\lambda = 445$ nm and $l = 200$.

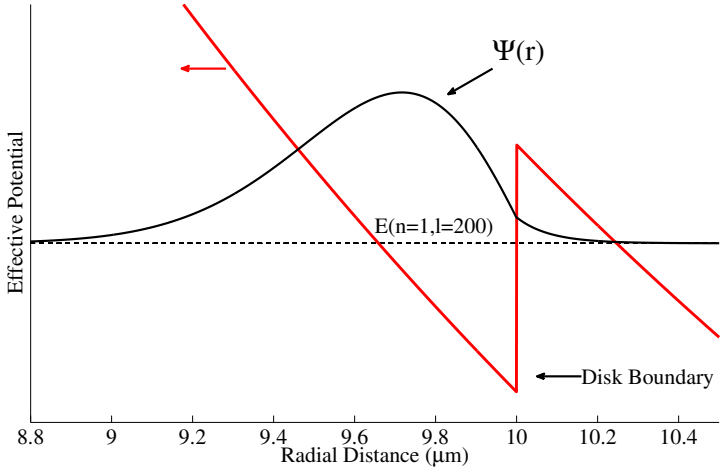

FIGURE 4.6: Effective Potential of a microdisk cavity with bound state wave function and energy level solution superimposed.

From Figure 4.6, one can now see why the lifetime of a mode is finite. Essentially, the mode (or bound state) has a finite probability of tunneling through the potential barrier which defines a cavity lifetime inversely proportional to the tunneling rate. The author would like to thank Xingyu Zhang for his generous help in the formulation and implementation of the quantum analogue presented above.

We conclude our discussion of microdisks with a plot of the calculated spontaneous emission factor β from [12] shown in Figure 4.7. We can see that β can be as high as 0.25, which can lead to low threshold lasing as seen in section 3.3.1. As discussed previously, the high β comes from the long lifetime (high Q) small modal volume (low V) properties of the microdisk, which can theoretically be as high as 1e6, and $1(\frac{\lambda}{n})^3$, respectively.

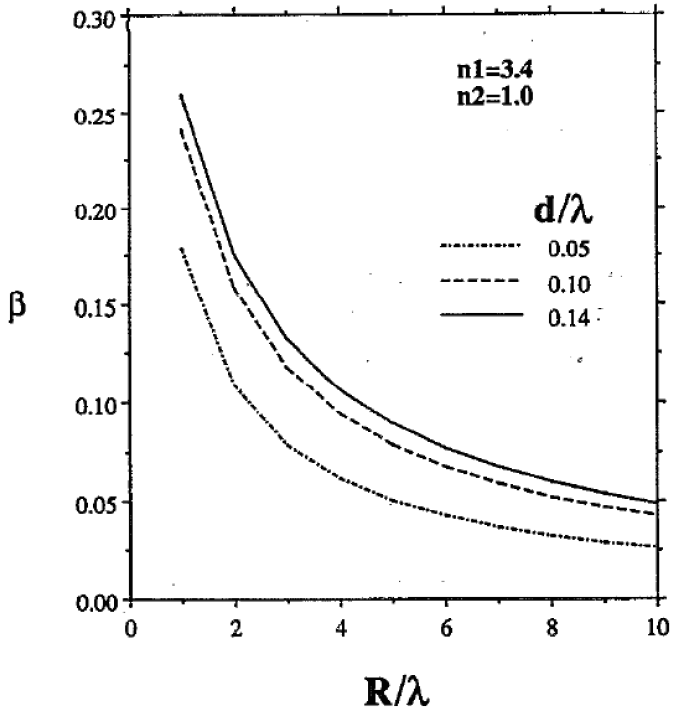

FIGURE 4.7: Calculated spontaneous emission factor for microdisks of varying radii and thickness from [12] assuming only one mode overlaps the gain spectrum of the emitter.

In the next section we discuss the theory of operation for another type of optical resonator, photonic crystal cavities, which can exhibit even higher device performance

over microdisk resonators.

4.2 Photonic crystal cavities

As we have seen in the discussion of microdisks in section 4.1, there is a direct analogue between quantum mechanics and Maxwell's equations. The photonic crystal cavity (PCC) utilizes a symmetry breaking inside a periodic dielectric structure in order to localize light within the region of an optical defect. This is very similar to an atomic defect within a periodic lattice, acting to confine electrons to a finite region. Concepts from solid state physics such as the Bloch condition, band structure and band gap can be directly applied to their photonic counterpart. PCCs serve as ideal high spontaneous emission factor optical cavities and are implemented in the lowest threshold InGaN based laser to date, presented later in Section 7.2. We begin with the photonic crystal band structure, then continue to PCCs which introduce defect states within the photonic band gap that localize photons, and finish with theoretical and experimental results of optimized devcies' spontaneous emission factors. The discussion in this work is heavily based on "Photonic Crystals," by Steven G. Johnson (2008). For further details on topics presented below please refer to that text.

Consider a one dimensional periodic dielectric structure with dielectric constants ϵ_1 and ϵ_2 with lattice constant a, where $\epsilon_1 > \epsilon_2$. If we consider a photon with wave vector k propagating in the positive $\hat{x}$ direction with electric field $\vec{E} = e^{i(kx-\omega t)}$, and the photon wavelength is the same as the lattice spacing ($k = \pi/a$), strong Bragg scattering will occur. This causes a back propagating wave vector which leads to the existence of a standing wave in the medium, described by $\vec{E} = e^{i(kx-\omega t)} \pm e^{-i(kx-\omega t)}$. The energy density is proportional to the dielectric constant multiplied by the magnitude of the

electric field squared. For a standing wave, this can be separated in terms of sines and cosines.

$$\begin{aligned} \langle U \rangle_- &= \frac{\epsilon(x)\epsilon_0}{2} sin^2(\frac{\pi x}{a}) \\ \langle U \rangle_+ &= \frac{\epsilon(x)\epsilon_0}{2} cos^2(\frac{\pi x}{a}) \end{aligned} \tag{4.19}$$

Where $\langle U \rangle_+$ and $\langle U \rangle_-$ correspond to waves which are localized primarily in the regions of high and low dielectric constant respectively. After matching boundary conditions at each interface, one has an energy density which is shown in Figure 4.8 that is adapted from [13].

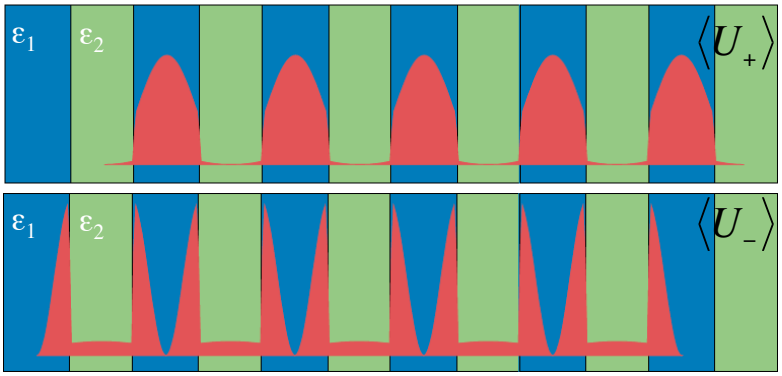

FIGURE 4.8: Energy density of standing waves which are localized in the regions of the high (ϵ_1) and low (ϵ_2) dielectric constant, respectively.

The band structure can be found using the photonic analogue of the quantum Kronig-Penney model and is presented in Figure 4.9. One can show that a photonic band gap exists if $\epsilon_1 > \epsilon_2$. Furthermore, for many practical devices, including those presented in this work, the low dielectric medium is air ($\epsilon_2 = 1$). This allows for the definition of two bands: the dielectric and air bands. These correspond to light localized in the dielectric and air medium, respectively.

If we now consider a break in the periodicity of the dielectric stack, we can introduce a defect state that exists within the photonic band gap. As light at frequencies within

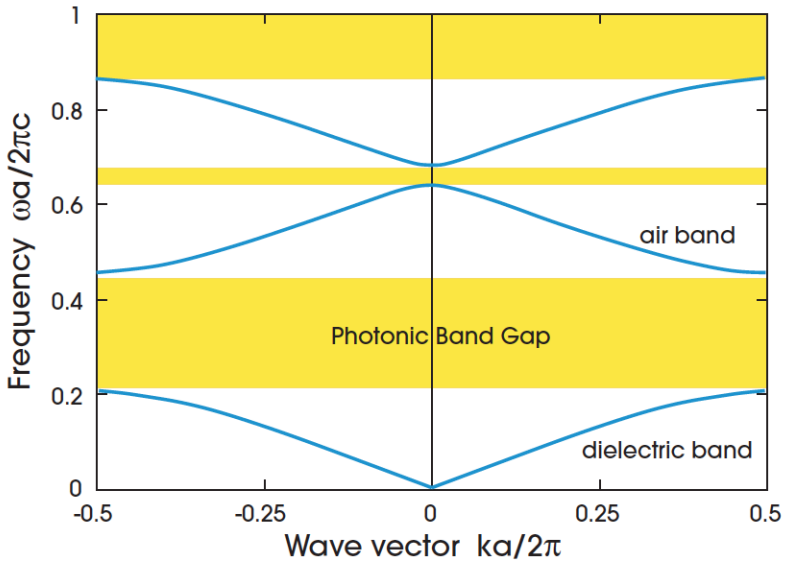

FIGURE 4.9: Bandstructure for a 1D dielectric-air stack, adapted from [13]. The photonic band gap is critical to the operation of photonic crystal cavities.

the photonic band gap is exponentially decaying in the periodic region of the dielectric stack, the light is confined to the spatial region of the photonic crystal defect. Figure 4.10 shows the spatial profile of a one dimensional PCC as well as the photonic density of states (DOS) versus frequency.

From Figure 4.10 one can observe three properties of PCCs which make them excellent platforms for low-threshold lasers. Firstly, the modal volume of the optical cavity can be extremely small due to the fact that the break in periodicity needs to be only the size of one element in the periodic array. This leads to structures with modal volumes as low as $.01(\frac{\lambda}{2})^3$, making PCCs the smallest dielectric optical cavities to date [92]. The second desirable trait of PCCs is their long cavity lifetimes (or equivalently high Q), due to the vanishingly small DOS at frequencies within the photonic band gap in the dielectric stack region of the device. Recent work has demonstrated theoretical quality factors higher than 10^9 and experimental realization higher than 10^5 [93, 94]. The high Q, low V properties of PCCs lead to high Purcell factors for the lasing mode, defined as F in Eq. 3.45. These in turn, contribute to high spontaneous emission (β) factors. The

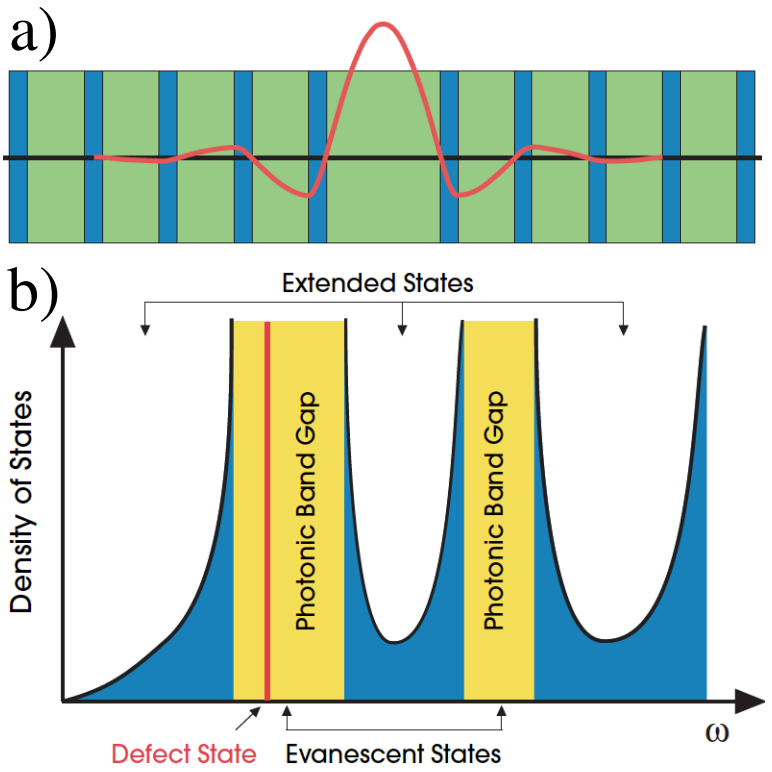

FIGURE 4.10: Bandstructure for a 1D dielectric-air stack, adapted from [13]. The photonic band gap is critical to the operation of photonic crystal cavities.

third point of interest of PCCs also relates to the DOS within the photonic band gap. This is numerically calculated for a photonic crystal and shown in Figure 4.11, adapted from [14].

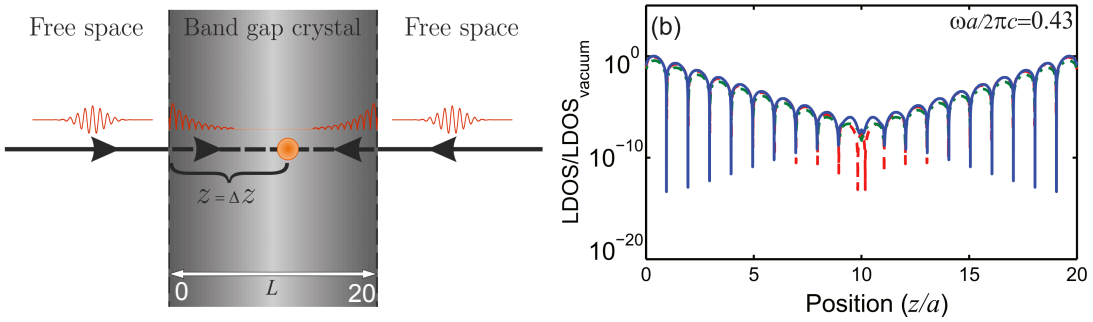

FIGURE 4.11: Calculated density of states (DOS) for a frequency of light within the photonic band gap of a photonic crystal, adapted from [14]. The vanishingly small DOS versus free space leads to record high β factors.

As discussed previously in section 3.4.1, reducing the rate of spontaneous emission into pathways other than the lasing mode (defined as ξ) leads to higher values of β.

Furthermore, as the rate of emission is proportional to the density of states, the small density of states at frequencies other than the lasing mode lead to inhibited emission and therefore low values of ξ. Utilizing various PCCs designs experimental β factors as high as 0.41, 0.85, 0.92 and 0.94 have been reported[15, 16, 19, 95]. Figure 4.12 shows various PCC cavity designs, from which it is currently accepted that the 1D nanobeam offers the best cavity design for high Q and low V adapted from references [15–17].

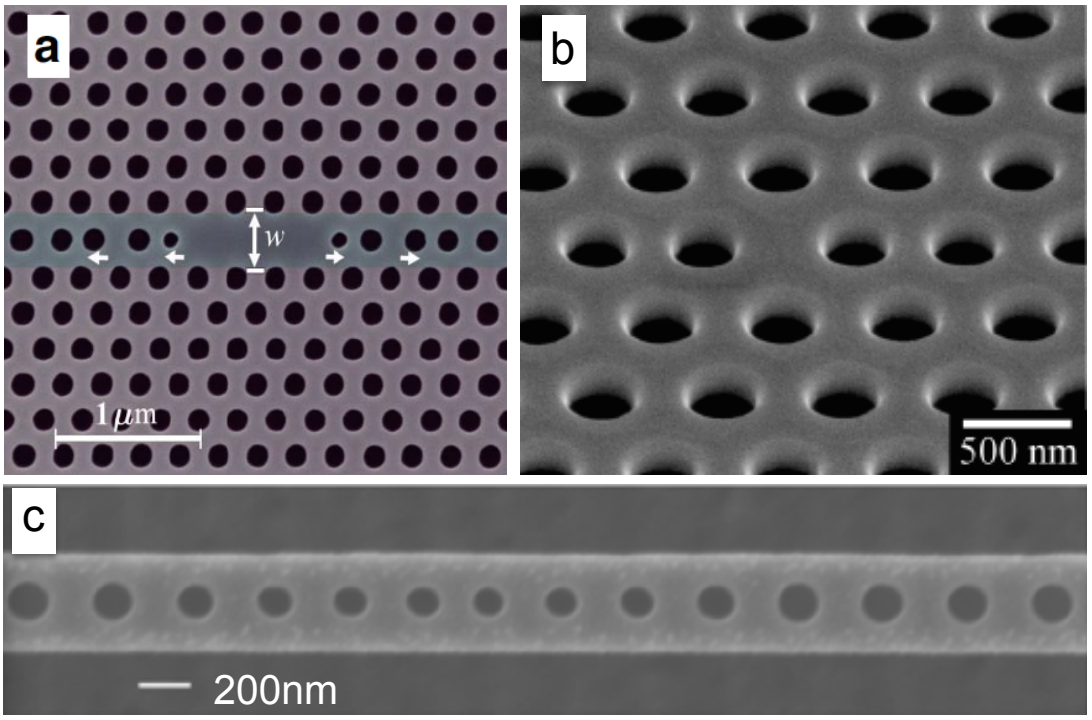

FIGURE 4.12: Various high beta PCC designs taken from references [15–17], respectively.

Chapter 5

Semiconductor Gain Medium

5.1 Semiconductor gain medium

In this section we shift our focus from the optical cavity design to the properties of the gain material. From our discussion of the laser rate equations, we found the lasing threshold decreases as the gain coefficient (G_0) increases and the threshold current density (n_{th}), decreases as shown in Figures 4.4 and 3.14, respectively. It is therefore desirable to utilize a gain medium with a high gain and low-threshold current density in order to realize a low-threshold laser. In order to calculate the gain per unit length for a given material, we follow the formalism given in reference [96] and reformulate the Beer-Lambert law originally presented in Eq. 3.10 in terms of a spatial derivative given in Eq. 5.1.

$$g_m = \frac{1}{X}\frac{dX}{dz} \tag{5.1}$$

Where X is the photon density and z is the spatial dimension in which the light propagates. Using the chain rule and the fact that $\frac{dz}{dt} = v_g$, where v_g is the group velocity of

light in the semiconductor one arrives at Eq. 5.2.

$$g_m = \frac{1}{X v_g} \frac{dX}{dt} \tag{5.2}$$

As we are only interested in the rate of photon generation due to stimulated emission, we include the radiative transition rate (τ_{st}^{-1}), calculated using Fermi's Golden Rule, as well as the occupation probabilities f_1 and f_2 for an electron being at a given energy in the valence or conduction band, respectively. As a note, only electrons that satisfy both energy and momentum conservation with a photon transition will undergo stimulated emission and emit photons. Therefore the entire population of the valence or conduction band is not considered for the gain calculations. This is quantified by defining f_1 and f_2 using Eq. 5.3.

$$\begin{aligned} f_1 &= \frac{1}{e^{(E_1 - E_{Fv})/kT} - 1} \\ f_2 &= \frac{1}{e^{(E_2 - E_{Fc})/kT} - 1} \end{aligned} \tag{5.3}$$

Where E_1 and E_2 satisfy the relation $\Delta E = E_2 - E_1 = h\nu$, where ν is the frequency of the light emitted upon the recombination of the electron-hole pair. T also represents the temperature of the system and E_{Fv} and E_{Fc} represent the quasi-Fermi levels in the valence and conduction bands, respectively. Implementing our expression for $\frac{dX}{dt}$ one arrives at an expression for the gain given in Eq. 5.4.

$$\begin{aligned} g_m &= \frac{\tau_{st}^{-1}}{X v_g} \rho(\Delta E) \cdot (f_2 - f_1) \\ g_m &= \frac{2\pi}{\hbar} \frac{1}{X v_g} \left| \langle E_2 | \, \vec{E} \cdot \vec{d} \, | E_1 \rangle \right|^2 \rho(\Delta E) \cdot (f_2 - f_1) \\ g_m &= \frac{2\pi}{\hbar} \frac{2q^2 \hbar \omega}{cn\epsilon_0} |\langle E_2 | \, \vec{r} \, | E_1 \rangle|^2 \rho(\Delta E) \cdot (f_2 - f_1) \end{aligned} \tag{5.4}$$

Where τ_{st}^{-1} is the stimulated emission rate calculated using Fermi's Golden Rule, in analogy to the spontaneous emission rate calculated in Eq. 3.16. The photon density X has also been reformulated in terms of the frequency and dielectric constant by equating expressions for the energy density given in Eq. 5.5. Finally, the group velocity has been simplified using the relation $v_g = c/n$ where $n^2 = \epsilon$.

$$U = \hbar\omega X = \frac{1}{2}\epsilon_0 \epsilon \left|\vec{E}\right|^2 \tag{5.5}$$

For semiconductor lasers, there are four different types of gain media which have been realized, all of which depend on altering the degrees of freedom of the electron-hole pair from 3 dimensions down to 0 dimension. The precise value of the gain (g_m) must be calculated for each medium using the density of states in addition to the wave functions of the electron in the valance and conduction bands for the dimensionality of each gain media. This calculation has been carried out in reference [18] and the density of states as well as the gain for 3D to 0D $Ga_{0.47}In_{0.53}As/InP$ emitters is shown in Figure 5.1. As expected from Eq. 5.4, the maximum gain is the highest for the quantum dot (QD)

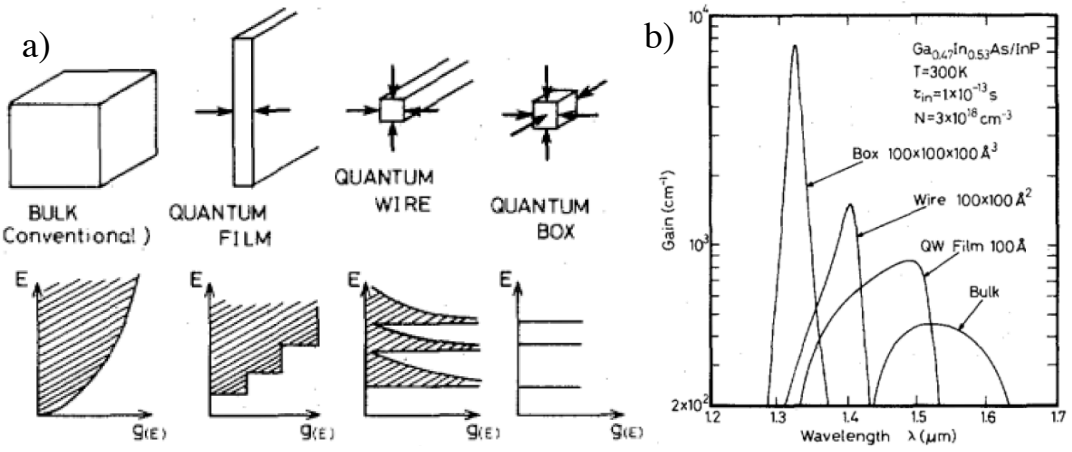

FIGURE 5.1: a) Density of states for an emitter with 3, 2, 1 and 0 degrees of freedom for the exciton which correspond to bulk, quantum film (also known as quantum well), quantum wire and quantum box (also known as quantum dots) respectively. b) The gain for $Ga_{0.47}In_{0.53}As/InP$ formed into each of dimensionality shown in a) [18].

as the density of states and electron-hole overlap is maximal when the exciton has zero degrees of freedom. One can also calculate the threshold current density which is shown in Figure 5.2, also taken from reference [18].

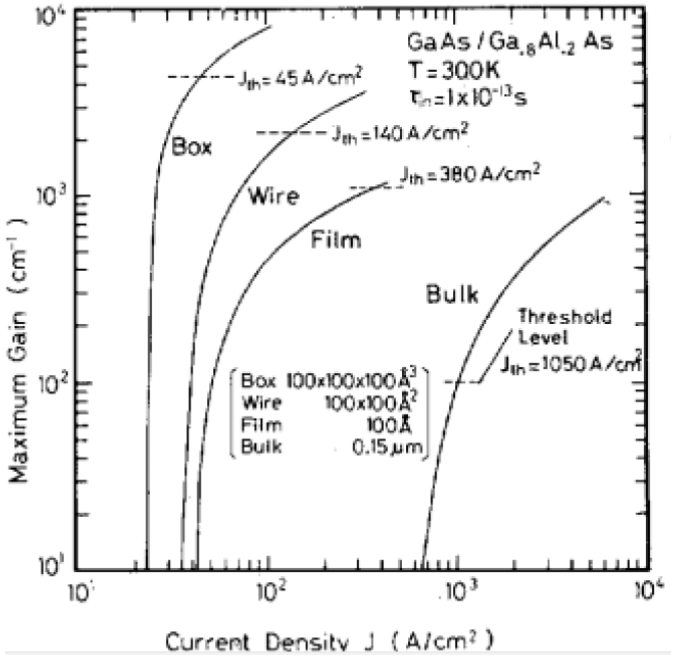

FIGURE 5.2: Calculation of the maximum gain as well as the threshold current density for each dimensionality of the $Ga_{0.47}In_{0.53}As$/InP gain media. [18]

Figure 5.2 sums up the results of this section, as the QD emitters clearly have the highest gain and lowest threshold current density. This theoretically makes them the best gain material for low-threshold lasers. As a practical note, quantum well (QW) lasers can (and often do) have lower thresholds than QD lasers. This is because the areal coverage of QDs compared to a QW can lead to a higher capture efficiency of photo-generated or electrically-injected carriers which ends up dominating the higher differential gain of the QDs. We will return to this point in more detail in the Section 6.4.

5.1.1 Quantum dots within microcavities

As we have seen in our discussion of optical cavities as well as semiconductor gain media, incorporating a QD active medium inside a high-spontaneous emission factor optical cavity in the form of a microdisk or PCC offers the optimum design for low-threshold lasers. This has been experimentally demonstrated in a variety of material systems, with the lowest lasing thresholds in the arsenides and phosphides obtained with PCCs and microdisks with embedded QDs in the (as of 2014). Figure 5.3 shows experimental data of lasing thresholds for indium arsenide (InAs) QDs within gallium arsenide (GaAs) PCCs with threshold as low as 124nW and 181nA for optically pumped and electrically injected devices, respectively [15, 19].

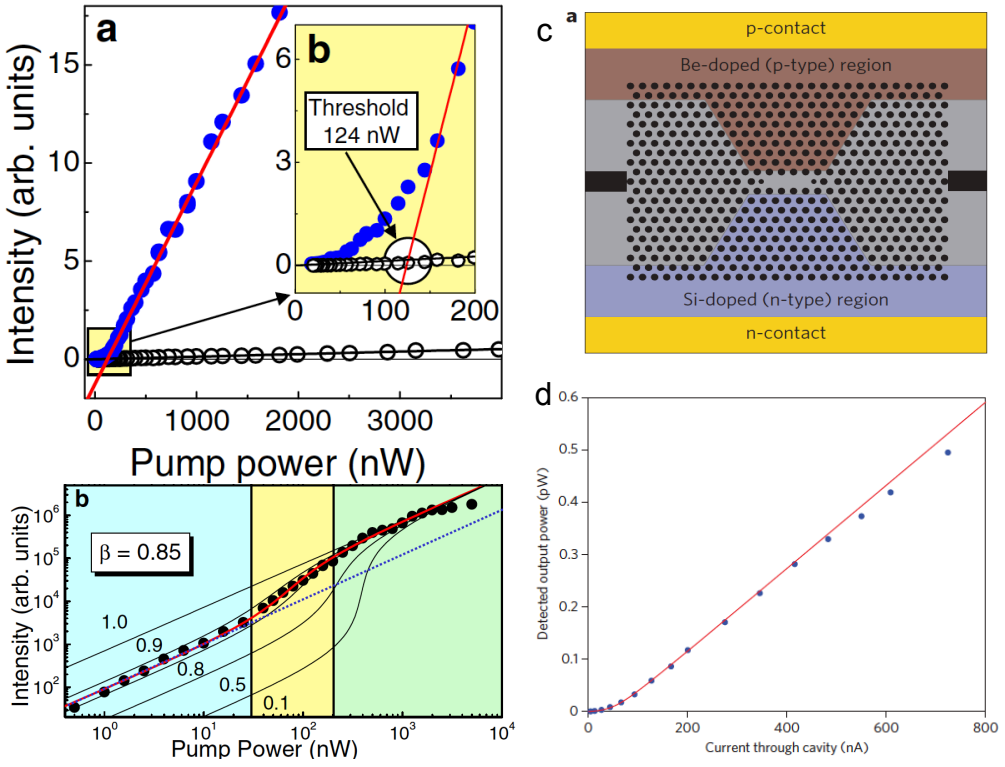

FIGURE 5.3: PCC lasers with embedded InAs QDs, a) and b) are data taken from an optically pumped device from [15], and c) and d) are for an electrically pumped device from [19]

Figure 5.4 shows microdisk lasers with embedded InAs and InP QDs with thresholds as low as $1\mu W$ and $1.6\mu W$, respectively, measured via optical pumping [20, 21].

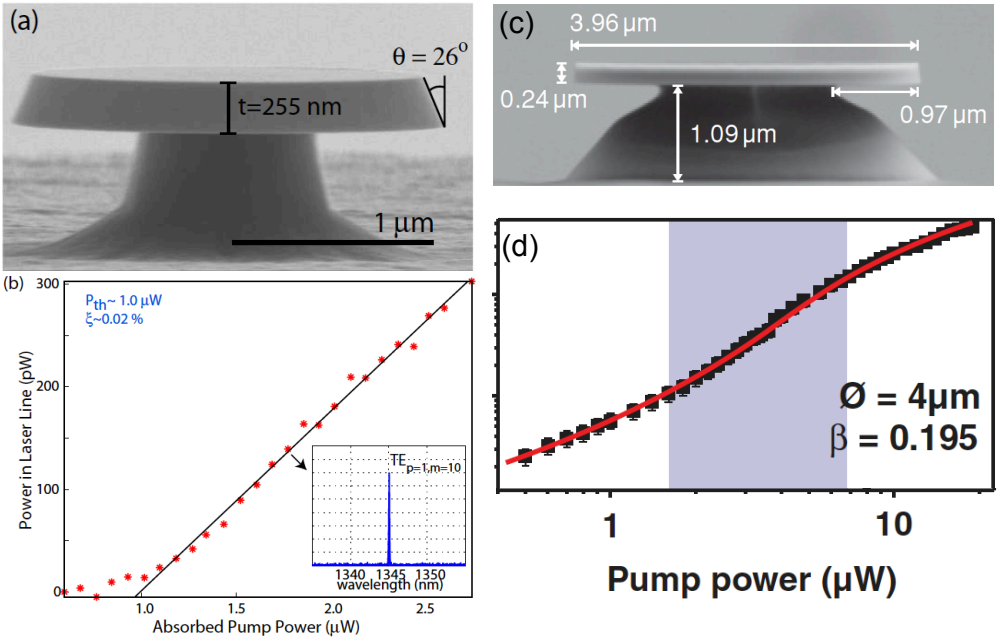

FIGURE 5.4: Optically pumped low-threshold microdisk lasers. a), b) $2\mu m$ microdisk laser with embedded InAs QDs. c), d) $4\mu m$ microdisk laser with embedded InP QDs. [20, 21].

5.2 Conclusion

In Chapter 3 we derived the laser rate equations from first principles. We then separated the laser device into two fundamental components: the gain material and the optical cavity. We identified high-spontaneous emission factor optical cavities as having the potential for thresholdless lasing due to the large percentage of spontaneous emission that is coupled into the lasing below threshold. Next, in Chapter 4, we introduced microdisk and photonic crystal cavities as possessing spontaneous emission factors as high as 0.25 and 0.94, respectively, making them the optimal cavity designs to date. In this chapter, we found the gain and threshold current density of the laser device depends on the degrees of freedom of the confined exciton, with QDs having the best

performance. Combining our two analyses, we found that QD emitters embedded within high-spontaneous emission factor optical microcavites serve as the ideal platform for low-threshold lasing. Experimental realizations of low-threshold microcavity lasers have been demonstrated for the arsenide and phosphides with thresholds as low as 124nW and 181nA for optical and electrical pumping, respectively. In the next chapter we consider the nitride family of emitters and show that InGaN within optical micro cavities has the potential to outperform other III-V emitters due to its wide band gaps and high exciton binding energies.

Part III

Experimental results

Chapter 6

InGaN QD microdisk lasers

6.1 Introduction

In this chapter we present the experimental results obtained from microdisks with embedded InGaN quantum dots (QDs). We first present the results demonstrating microdisks with Q's higher than 9,000, a record for GaN microdisk cavities. This study also demonstrated that the microdisk Q did not depend on the number of InGaN QD active layers, which suggested that reabsorption from the QDs was not limiting the device Q. Next, we present experiments demonstrating the first InGaN QD microcavity laser with lasing thresholds of 0.2mJ/cm^2 ($167\mu\text{W}$). The chapter concludes with a systematic study of the lasing dynamics of microdisks containing three layers InGaN QDs, quantum wells (QWs) or fragmented quantum wells (FQWs) which conclusively proved that the lasing was facilitated by the QD gain media and not the accompanying FQW layers.

6.2 Optimizing the device design

The following authors contributed to the work presented in this section, Alexander Woolf*, Dr. Igor Aharonovich*, Dr. Kasey J. Russell*, Nan Niu, Christine Zgrabik, Dr. Tongtong Zhu, Dr. Menno J. Kappers, Prof. Rachel A. Oliver and Prof. Evelyn L. Hu. Where the * denotes equal contribution. Alex and Igor fabricated and measured the devices. Nan and Christine assisted in measuring the devices. Kasey, Alex, and Igor analyzed the data, Tongtong and Menno grew the material. Rachel and Evelyn led the Cambridge and Harvard teams respectively.

As mentioned in Section 2.3, the high chemical inertness of the nitrides provides challenges in their fabrication into high quality optical cavities. The epitaxial growth of these materials on lattice-mismatched substrates limits the crystalline perfection of the materials. Furthermore, the relatively short emission wavelength of the GaN-related compounds makes them extremely sensitive to fabrication defects and scattering. It is particularly important to identify and eliminate the sources of loss in the cavities, associated with the material growth. These include dislocations, point defects and absorption due to the active gain medium and the surrounding material. It was shown previously, that choosing quantum dots (QDs) as emitters instead of quantum wells (QWs) reduce the absorption. Furthermore, detailed materials exploration with various structure designs has been explored to engineer the optimum structure for photonic devices [2]. Indeed, there is an ongoing effort to improve the quality factors achieved with GaN materials. Recent reports of Q's of approximatly 5000 in InGaN/GaN quantum well PCCs and GaN/AlN quantum dot (QD) microdisk cavities have been documented [97, 98].

In this section we report on record high quality factors approaching nearly 10,000, obtained from GaN microdisk cavities 3 μm in diameter, containing embedded InGaN QDs [32]. Furthermore, we compare four different samples which have membrane thicknesses of 120 nm and 200 nm and contain either one or three layers of QDs [99] (Figure 6.1). Our results indicate that the microdisk cavities fabricated with the thicker membrane layer typically exhibit a higher quality factor than the thinner ones. The increase in Q is a result of reduced electric field strength at the vertical boundaries of the microdisk, leading to lower loss.

A schematic illustration of the sample structure is shown in Figure 6.1. This also summarizes the materials properties of the four samples. Briefly, an $In_xGa_{1-x}N$/ $In_yGa_{1-y}N$ sacrificial super lattice (SSL, x = 5.1%, y =6.1% In) is grown on an n-doped GaN pseudosubstrate and capped by a thin 10 nm GaN layer, followed by an $Al_{0.2}Ga_{0.8}N$ etch stop layer. Previous studies have shown that structures with higher indium contents in the SSL underwent relaxation and generated further dislocations, resulting in higher surface pit densities and lower Q values overall in microdisks fabricated by the photoelectrochemical (PEC) etch process. The compositions used here were chosen to avoid strain relaxation within the full structure, as can be ascertained from the surface pit densities, which are similar to that of a GaN pseudo-substrate (typically 3-6 $\times 10^8$ cm^{-2}) [100]. The surface pits relate to the termination of dislocations (both edge and screw dislocations were observed with an atomic force microscope [2]) and provide a fairly accurate measure of the density of dislocations threading through the disk.

Figure 6.2 shows the photoluminescence (PL) spectra of the as-grown samples, prior to disk fabrication, recorded at room temperature using an excitation wavelength of 266 nm. The peak near 360 nm is the GaN band-edge emission, whereas the peak near 380 nm is emission from the InGaN superlattice structure that is selectively etched during

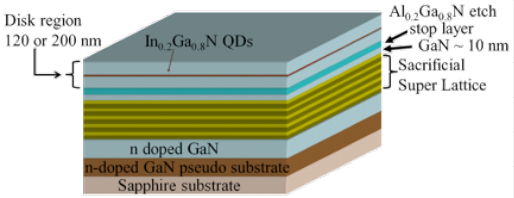

Sample	QD layers	Membrane thickness	Surface pit density (cm^{-2})
3QD_120nm	3	120	$(5 \pm 0.6) \times 10^8$
1QD_200nm	1	200	$(4 \pm 0.6) \times 10^8$
3QD_200nm	3	200	$(5 \pm 0.4) \times 10^8$
1QD_120nm	1	120	$(4 \pm 0.5) \times 10^8$

FIGURE 6.1: (a) A schematic illustration of the sample structure. The disk region has a thickness of 120 or 200 nm with either one or three embedded QD layers. (b) Material properties of the four investigated samples.

microdisk fabrication. More energy from the laser is absorbed in the 3 QD layers than in the single QD layer before it reaches the sacrificial layers, therefore less light is generated in the sacrificial layers of 3QD structures for a given laser power density. Sample 1QD-200nm has a thicker GaN cap then 1QD-120nm and therefore more emission from the InGaN is observed in the 1QD-120nm sample. The intensity of the broad emission centered at 570 nm (commonly referred to as yellow band emission) varies between the different samples. From the power dependence measurements it can be seen that the yellow band emission in samples 3QD-200nm and 1QD-120nm is significantly lower than in samples 3QD-120nm and 1QD-200nm. Note that the pit density, which highlights the number of threading dislocations, is comparable across the samples.

To fabricate the microdisks, 3 μm silica beads were dispersed onto the samples to serve as etch masks. Mesas were then defined by reactive ion etching using a 500 W inductively coupled plasma (ICP) reactive ion etching in an argon/chlorine environment with a flow rate of 25/25 standard cubic centimeters per minute, respectively. The silica beads were then removed by immersing the samples in water in an ultrasonic bath for five minutes. The metal film (Ti/Au), which serves as the cathode for the PEC etching, was then deposited using an e-beam evaporator. Finally, to optically isolate the membrane layer, the microdisks were undercut using (PEC) etching [101] for 18 minutes. Using our approach, we fabricated and measured more than forty microdisks, providing a good

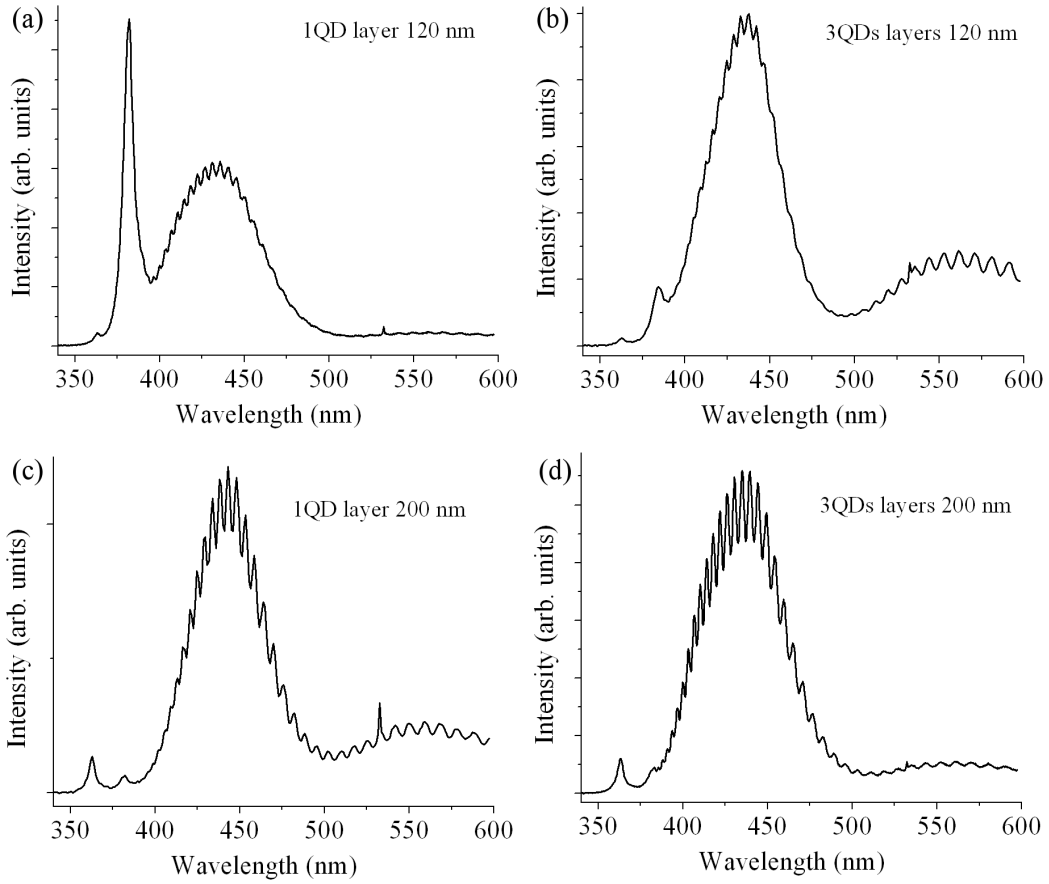

FIGURE 6.2: PL characteristics using 266 nm excitation laser (0.7 mW incident power) of the bulk samples. The PL intensity is normalized to the maximum emission intensity from the QDs. The peak near 360 nm is the GaN band-edge emission, whereas the peak near 380 nm is emission from the InGaN superlattice structure. (a) 1 QD layers 120 nm. (b) 3 QD layers 120 nm. (c) 1 QD layers 200 nm. (d) 3 QD layer 200 nm.

statistical sampling. Figure 6.3 shows scanning electron microscope (SEM) images of the fabricated microdisks. The smooth sidewalls of the microdisks are clearly evident. Some microdisks, as shown in Figure 6.3b and 6.3c, exhibited whiskers. These features are believed to be formed due to presence of threading dislocations in the material that locally reduce the efficiency of the PEC etch process [2]. We conclusively prove this in Section 7.4. Figures 6.3b and 6.3c show representative side view SEM images of a microdisk with a 120 nm thickness membrane and a 200 nm thickness membrane, respectively. These figures also show that the same PEC etch time produces a larger undercut in the thicker samples than in the thinner ones. Based on the SEM images, the undercut in the thicker samples propagates approximately 100 nm deeper toward

the center of the disk, compared to the thinner samples. One hypothesis to explain this result is as that since all samples were etched down for the same amount of time, the metal cathode is closer to the post region in samples with 200 nm thickness membranes than in samples with 120 nm thickness membranes. The proximity of the metal provides a shorter collection path for the electrons and increases the etch rate. Further analysis is required to more fully understand the differences in the etch rates, but we believe this is related to the different geometries of the structures, relative to the placement of the cathode material used in the etch process.

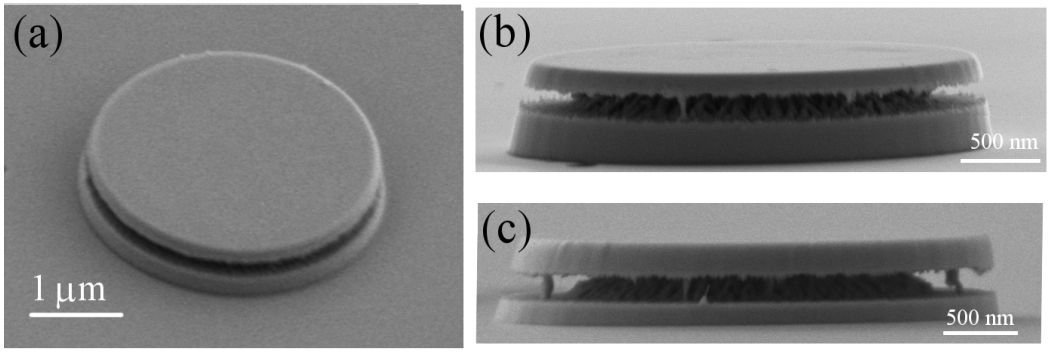

FIGURE 6.3: SEM micrographs of a 3 μm microdisk cavities. (a) Perspective view of the microdisk. (b) Sideview image of a microdisk with a 120 nm membrane thickness. (c) Sideview image of a microdisk with a 200 nm membrane thickness. Some whiskers are observed on the sidewall of the microdisks.

A frequency-doubled titanium sapphire laser emitting at 380 nm was employed to carry out spectroscopic analysis on the microdisks. The 500 nm diameter beam was incident on the top of the microdisks through a long working distance objective (100, numerical aperture = 0.5). The emission from the microdisk was collected through the same objective and directed into a spectrometer through a lens and a 10 μm single mode fiber to achieve better confocality. Figure 2.10 shows a schematic of the (μ-PL) setup used to collect all the spectra obtained in this work.

Figure 6.4 a)-d) shows PL spectra recorded at room temperature from each of the samples. Whispering gallery modes (WGMs) are evident, modulating the broad emission

from the QD layers. By employing finite difference time domain (FDTD) simulation of the field intensity, we identified the first and second order WGMs in the radial direction with transverse electric (TE) polarization. The 8 nm free spectral range of the first order WGMs agrees with the theoretical simulations for a 3 μm disk with refractive index of 2.48. These modes are partially marked on the spectra in Figure 6.4 a)-d). The microdisks with the thinner 120 nm membrane show primarily first order WGMs. The microdisks with the thicker membrane of 200 nm exhibit higher order modes. As noted earlier, the 200 nm thick microdisks were more deeply undercut than the 120 nm thick disks. Therefore, thicker samples can support the propagation of second order WGMs, closer to the center of the disk.

Figures 6.4 e) and f) show Lorentzian fits of particular modes from samples 3QD-200nm and 3QD-120nm, respectively. The Q values were determined by calculating $\lambda_{cav}/\Delta\lambda_{cav}$, where λ_{cav} is the cavity mode resonance and $\Delta\lambda_{cab}$ is the full width at half maximum (FWHM) of the mode. The measured Q of 9100 was the highest Q reported from GaN-based microdisks reported to date. Calculations using FDTD reveal that the theoretical Q values for the microdisks with 200 nm and 120 nm membranes are 1.3×10^5 and 6.9×10^4, respectively. Therefore, our obtained quality factors are still approximately one order of magnitude smaller than the calculated values. However, these Qs were obtained in microdisk cavities with relatively small diameters of 3 μm which exhibit smaller modal volumes [98].

Figure 6.5 a) shows a comparison of the highest measured Q from each of the samples. Figure 6.5 b) shows the quality factors measured for the WGMs of the four samples as a function of wavelength. Each data point represents a particular frequency of a WGM. Noticeably, the microdisks which have a thicker membrane of 200 nm exhibit significantly higher quality factors (Q of 8000) than the microdisks with a 120 nm

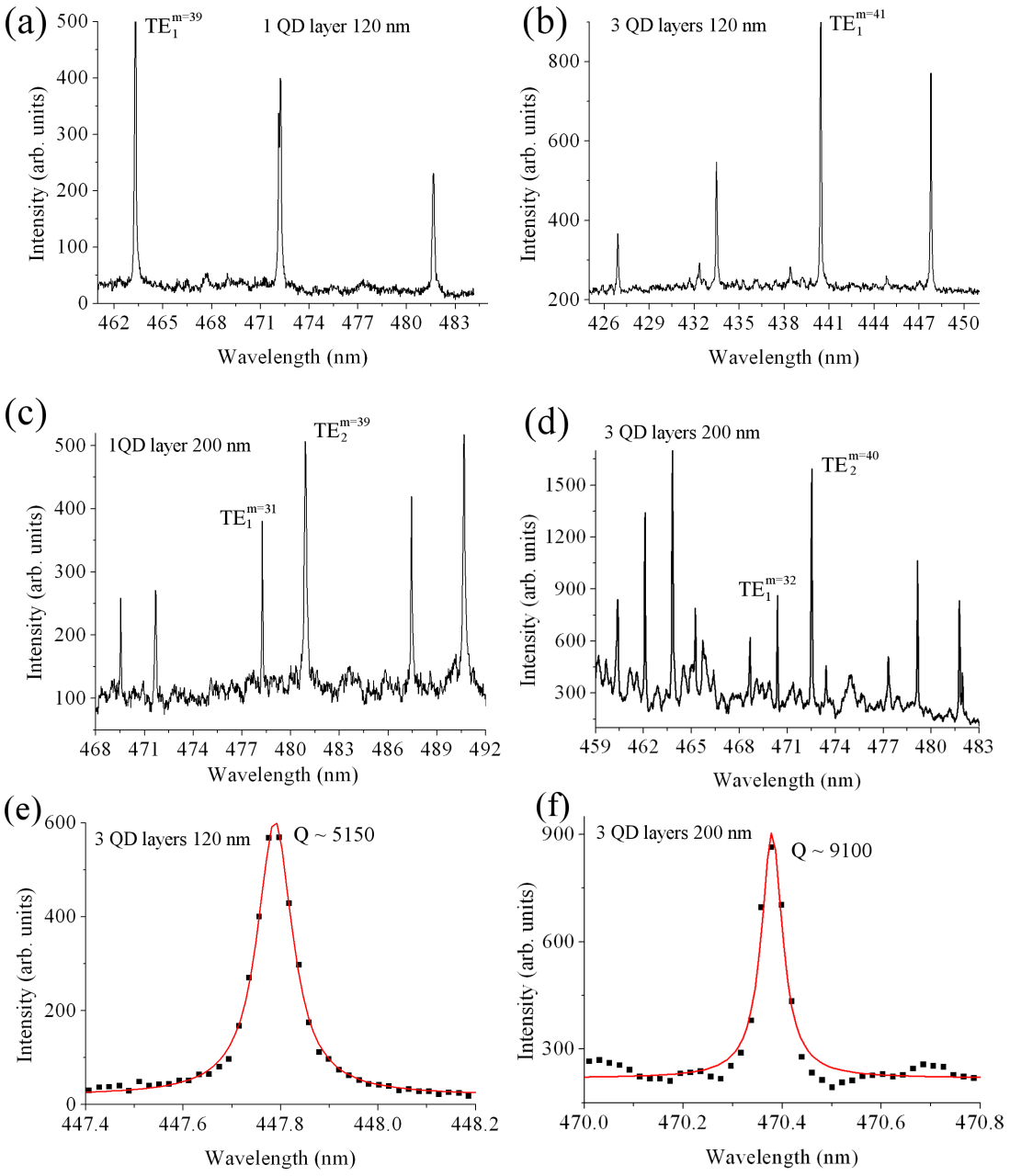

FIGURE 6.4: PL spectra of the four samples recorded at room temperature using 380 nm excitation. a) 1 QD layer 120 nm. b) 3 QD layers 120 nm. c) 1QD layer 200 nm d) 3 QD layers 200 nm. (e,f) Enlarged spectral range of a high Q modes from sample 3QD-120nm and 3QD-200nm, respectively.

membrane (Q of 5000). First order WGMs with quality factors on the order of 8000 were repeatedly measured from the samples with 200 nm membrane thickness. This may be attributed to a more efficient PEC etch achieved with thicker membranes. Thinner membranes are more susceptible to inhomogeneity during the etching process reducing the quality factor of the cavity.

No clear distinction is observed between the one and three QD layers, indicating that addition of QD layers does not degrade the quality factor. This is also true when comparing WGMs with equal energy (e.g. at 480 nm, Figure 6.5 b)) where the distribution of quality factors does not depend on the number of QD layers. Some of the microdisks with three layers of InGaN QDs showed improved Q when compared to microdisks with one layer of QDs. This observation implies that the reabsorption by the QDs is not a dominating mechanism for the limited Q achievable in GaN microdisk cavities to date. The internal electric field in InGaN QDs leads to quantum confined stark effect [102], significantly reducing the reabsorption efficiency of QDs for the emitted photons. The emission from sample 3QD-120nm is clustered at lower wavelengths and this sample exhibits lower quality factors. Before processing, this sample showed similar PL to the other samples (Figure 6.2) and at this time we cannot identify the reason for the observed blueshift. Finally, no clear correlation is observed between the intensity of the yellow band and the observed Q in the different materials. The yellow band is profoundly larger in samples 3QD-120nm and 1QD-120nm, than in samples 3QD-200nm and 1QD-120nm. However, the highest Q's were measured in samples 1QD-200nm and 3QD-200nm. Therefore, we can suggest that sources of absorption and loss other than the QD layers or the yellow-band related defects are present in the samples.

The demonstration of high Q resonators with three layers of QDs is highly advantageous for more advanced quantum optics experiments such as lasing and weak/strong

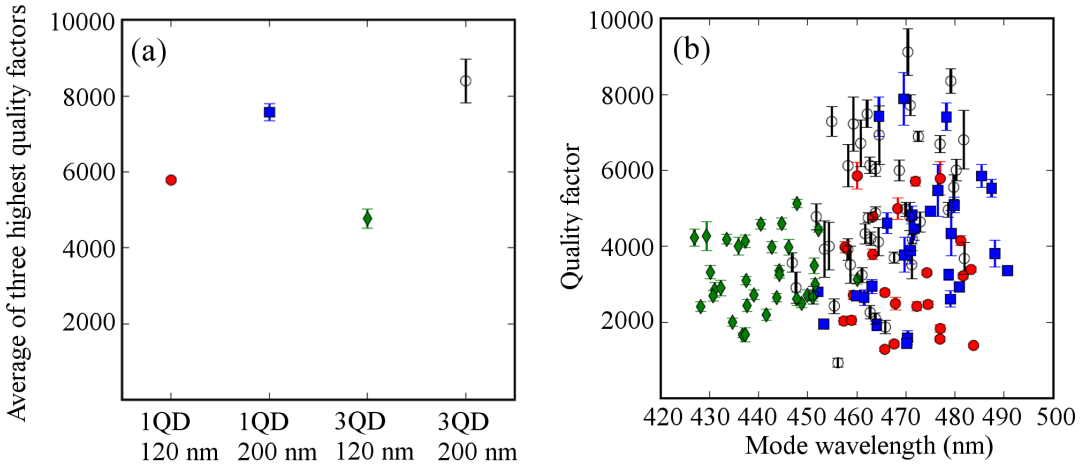

FIGURE 6.5: (a) Highest quality factor of a first order mode observed for each sample. (b) Distribution of quality factors as a function of wavelength for each of the samples (the symbols correspond to the samples as in a)).

coupling. This is because a higher density of QDs enhances the probability of spectral and spatial overlap between the QD emission and the cavity mode. Brighter luminescence is typically achieved from these samples, making them amenable to brighter and more efficient light emitting devices. On the other hand, achieving high Q cavities with only one layer of QDs will be pivotal for coupling a single QD to a cavity mode and a realization of brighter single photon emitters via modification of their spontaneous lifetime through Purcell enhancement.

To summarize, we fabricated microdisk cavities with embedded InGaN QDs that exhibited WGMs with record high quality factors (9000). We showed that microdisks with membrane thickness of 200 nm have higher quality factors than microdisks with 120 nm membrane thickness. Finally, it was shown that the number of QDs layers within the photonic resonator does not degrade the quality of the cavity. Our results will have important implications in the demonstration of Purcell enhancement with InGaN QDs and realization of room temperature low-threshold lasing.

6.3 First demonstration of lasing from microcavities with embedded InGaN QDs

The following authors contributed to the work presented in this section, Alexander Woolf*, Dr. Igor Aharonovich*, Dr. Kasey J. Russell*, Dr. Tongtong Zhu, Nan Niu, Dr. Menno J. Kappers, Prof. Rachel A. Oliver, and Prof. Evelyn L. Hu. Where the * denotes equal contribution. Alex and Igor fabricated and measured the devices. Nan assisted in measuring the devices. Kasey, Alex, and Igor analyzed the data, Tongtong and Menno grew the material. Rachel and Evelyn led the Cambridge and Harvard teams respectively.

In spite of our promising results obtained from 3 μm microdisks, none of the devices from Section 6.2 exhibited lasing. However, recalling our discussion of microdisk resonators in Section 4.1, the spontaneous emission factor (β) increases as the disk radius decreases. As the β factor increases, the lasing threshold will decrease, shown in Figure 4.2. This is due to the fact that there are fewer modes or pathways for the gain medium to emit light into. Therefore it takes fewer photogenerated carriers in the device to achieve the gain necessary to overcome the loss of light at the frequency of the lasing mode. In this section we present our results for the exact same structures in Section 6.2, however with diameters of 1μm instead of 3μm. As a note, the Q's are lower for 1 μm disks because the device has more curvature than a 3μm disk, causing a breakdown of the total internal reflection (TIR) boundary condition at the surface, which assumes the surface is flat. The decrease in the number of modes overcompensates the decrease in Q and allows for the realization of an InGaN QD laser.

Previous work on GaN-based lasers within microcavities has demonstrated room-temperature thresholds in the range of a few mJ/cm^2 (for pulsed measurements), [103]

or a few hundred kW/cm2 (CW)[79, 104]. This section describes the incorporation of quantum dot (QD)-containing active regions within high Q (6000) microdisk cavities. Lasing was achieved for 1 μm diameter microdisks incorporating three layers of QDs, at threshold energies as low as 0.28 mJ/cm^2. Our experiments took place with the concurrent evaluation of four sample structures allowing us to probe the influence of QD density and cavity design on the lasing threshold. The concurrent comparison of different materials and cavity structures will allow us to better understand the critical factors that determine the onset of lasing.

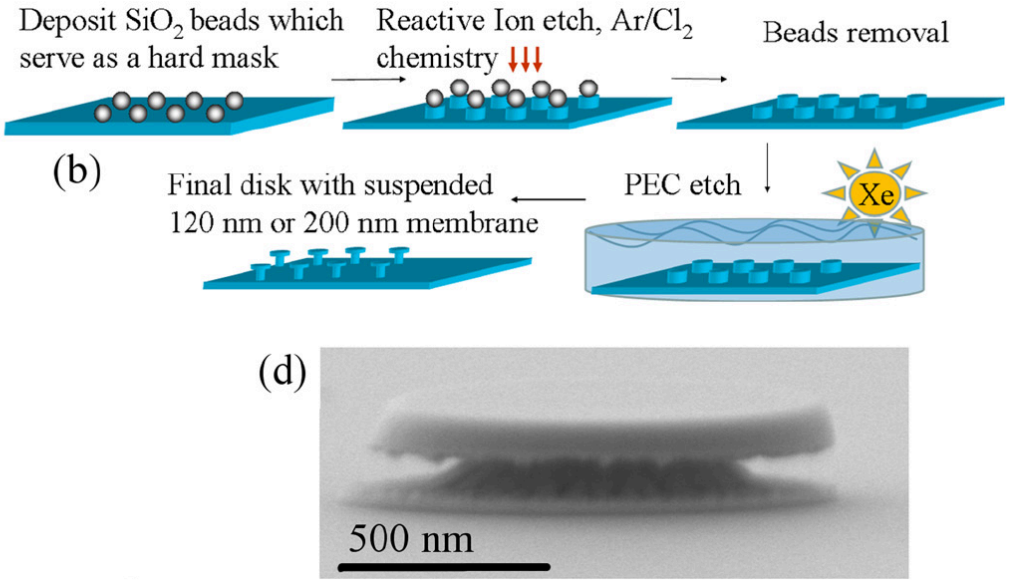

FIGURE 6.6: Schematic illustration of the procedure used to fabricate the microdisks. d) SEM image of the 1 μm diameter microdisk cavity.

The microdisks were fabricated by dispersing 1 μm silica beads onto the samples which served as etch hard masks. Figure 6.6 is a schematic of the fabrication process flow as well as an SEM of a completed 1μm microdisk. PL spectra recorded at room temperature from 1 μm diameter microdisks show whispering gallery modes (WGMs), modulating the broad emission from the QD-containing layers (Figure 6.7 a)). Figure 6.7 b) shows a high resolution spectrum of the transverse electric $TE_{1,11}$ mode at 475.8 nm from sample 3QD-200nm.

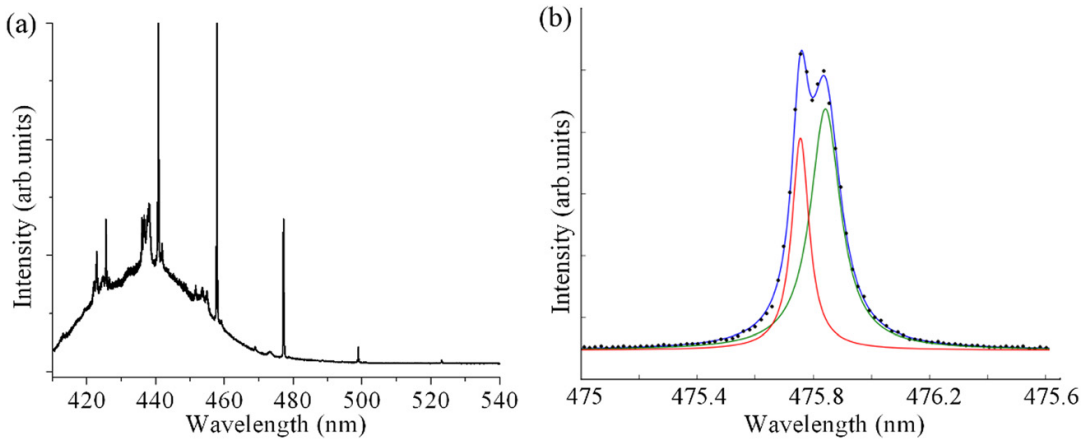

FIGURE 6.7: a) Optical characterization of a microdisk made of material 3QD-200nm. PL spectrum recorded using 380nm excitation wavelength, showing predominantly first order WGMs decorating the broad QD-related emission. b) High resolution PL spectrum of a high Q mode with Q equals 6600. Green and red lines are fits to a Lorentzian.

This mode exhibits a splitting between the two normally-degenerate counter-propagating WGMs that is likely due to slight imperfections in fabrication that destroy the rotational symmetry of the disk. These two modes are fitted with Lorentzian functions, as indicated with the red lines in Figure 6.7 b). The highest measured Q for 1μm diameter disks from sample 3QD-200nm, Q equals 6600, is one of the highest Q's reported from GaN-based microdisks [98].

Lasing behavior in microdisks is observed through the dependence of the PL emission intensity and mode linewidth on excitation power, as is shown in Figure 6.8 a). At excitation powers below the lasing threshold multiple WGMs are observed. As the excitation power is increased through the lasing threshold, the intensity of a single mode increases abruptly and at higher powers dominates the emission. This behavior is indicative of a transition from spontaneous emission to lasing. The lasing mode in this case was determined to be the $TE_{1,13}$ mode based on finite difference time domain (FDTD) simulations [105]. A plot of the output intensity versus input power for the microdisks from sample 3QD-200nm (blue triangles) and sample 3QD-120nm (red circles) is shown in Figure 6.8 b), with clear thresholds at 0.28mJ/cm^{2}and 0.63 mJ/cm^2, respectively.

The lasing threshold was determined as the intersection of the horizontal axis and a linear fit to the higher-power region of the data. The same data plotted on a log-log scale (top right inset, Figure 6.8 c)) shows all three regimes of operation: spontaneous emission, amplified spontaneous emission and laser oscillation [106]. In addition, we observed a pronounced narrowing of the lasing mode as the excitation power was increased through the lasing threshold, signifying the increased temporal coherence of emission in the lasing regime (Figure 6.8 c)). Taken together, this data unambiguously demonstrates the achievement of lasing behavior in our devices. The bottom left inset of Figure 6.8c) shows the optical image of the microdisk laser above lasing threshold recorded using a CCD camera.

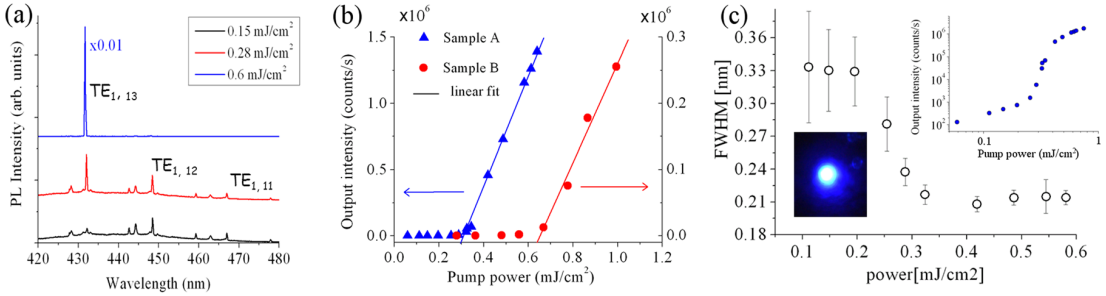

FIGURE 6.8: a) PL spectra as a function of excitation power recorded from a 1 μm size microdisk cavity (Sample 3QD-200nm). (b) Optical output power of the microdisk laser as a function of excitation power for sample 3QD-200nm (blue triangles) and 3QD-120nm (red circles). A clear lasing threshold is observed at 0.28 mJ/cm2 and 0.63 mJ/cm2 for samples 3QD-200nm and 3QD-120nm, respectively. The lines are a linear fit to the data above threshold. c) Linewidth of the lasing mode plotted as a function of excitation power for sample 3QD-200nm. The reduction of the linewidth is in accord with lasing behavior. Inset top right, same data as in b), replotted on a logarithmic scale. Inset bottom left, an optical image of the microdisk laser above threshold recorded using a CCD camera.

A comparison among all four samples provides an indication of the most critical factors affecting the lasing behavior of these devices. All microdisks included in this analysis exhibited pronounced modes in the PL spectra, with a minimum Q of 1000. Of the four samples investigated in this study, only samples 3QD-200nm and 3QD-120nm exhibited lasing behavior. Sample 3QD-200nm showed lower threshold lasing because it exhibits high Q and has three layers of QDs contributing to the emission gain. The

other samples have either thinner membranes, which FDTD simulations suggest should lead to lower maximum Q of 18,000 for 120 nm membrane versus Q of 25,000 for the 200 nm membrane, or have fewer layers of QDs. These variations in theoretical and actually-observed Q's of the structure and in density of the gain medium provide an excellent probe of the critical parameters in material and structure that give rise to low-threshold lasing. For all disks that achieved lasing, values were extracted for the threshold power, mode wavelength and maximum cavity Q measured at low excitation power (Figure 6.9). This trend is consistent with FDTD simulations, although in both samples the measured Q is more than an order of magnitude lower than the theoretical limit. This is not unusual, since the simulations do not account for imperfections in the material or in the fabrication of the microdisks.

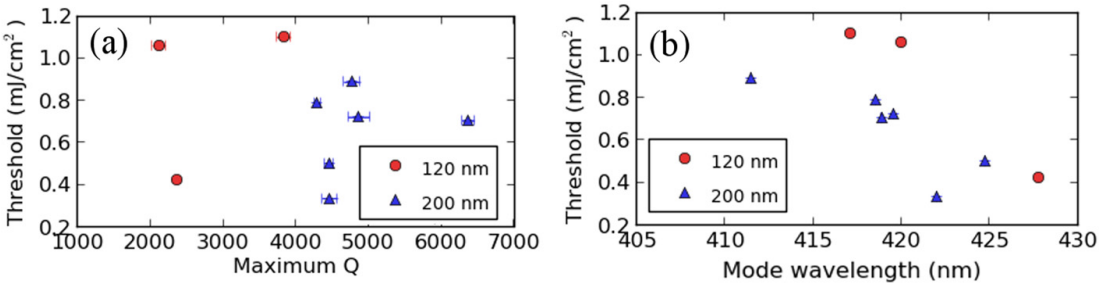

FIGURE 6.9: (a) Lasing threshold is plotted as a function of maximum Q recorded from the same microdisk for sample 3QD-200nm (blue triangles) and sample 3QD-120nm (red circles). (b) Lasing threshold is plotted as a function of a lasing wavelength for sample 3QD-200nm (blue triangles) and sample 3QD-120nm (red circles).

In samples 1QD-200nm and 1QD-120nm, which only contained a single layer of QDs, lasing was not observed on any disks under the excitation powers available in our experimental setup. In addition, the Q of these cavities was comparable to or lower than cavities from samples 3QD-200nm and 3QD-120nm, respectively. These observations suggest that re-absorption within the InGaN layers themselves is not the dominant factor limiting Q in these structures and that, at least under pulsed excitation at room temperature, multiple QD layers are necessary to supply sufficient gain to compensate

losses. The importance of the areal density of quantum dots, and how it limits the modal gain of the active layer, has been noted earlier for InGaAs-based quantum dot lasers [107]. Larger cavity, in-plane lasers with InGaN quantum dot active material have employed 8 to 10 QD layers [108–110]. We also note that no clear dependence is observed between the lasing threshold and the Q of the microdisk. Low InGaN re-absorption is consistent with the low number of QDs coupled to a mode:.Each 1 μm diameter disk contains approximately 100 QDs per layer at a QD density of 10^{10} cm^2, and of these, and due to their random placement in the cavity it is likely that fewer than 10 are in spatial and spectral resonance with a WGM.

Because re-absorption is sufficiently low in these devices, modes are visible across the entire gain spectrum and not only at the low-energy side of the spectrum (as is typical for GaN microdisks with quantum well active region [11, 111]. In fact, in our devices the lasing mode was consistently located at wavelengths shorter than 430 nm, on the high-energy side of the broad QD emission spectrum (Figure 6.9 b)). This dramatic blue-shift of the lasing wavelength for pulsed, rather than CW optical excitation has been observed previously in InGaAs QD microdisk lasers [112] The reasons for this behavior will be explored in the Section 6.4, but the cause was originally thought to relate to a differential change in radiative lifetimes within a cavity environment with a high instantaneous charged carrier background. The complex interplay between the energies of the lasing mode and the QD gain spectrum is evident in the variation of lasing threshold with wavelength (Figure 6.9 b)). The threshold decreases at longer wavelengths as the overlap with the QD emission spectrum increases. Nevertheless, lasing from a mode at the center of the QD emission spectrum was not observed.

Several aspects of this comparison highlight the need for further understanding of the interplay of active layer composition and cavity structure in determining the

lasing thresholds of the resulting devices. Further exploration is needed on the optimal InGaN QD material structure, the influence of background defects in the materials, the wavelength-dependence of the QD radiative lifetimes and efficiencies, as well as optimal cavity designs. In addition, our gain medium consists of InGaN layers which contain not only QDs but also an inhomogeneous ("patchy") quantum well layer, refered to here as fragmented quantum well (FQW). Atomic force microscope data indicating that the QDs may be located not only on top of the QW layer (similar to the case of Stranski-Krastanov (SK) growth in, for example, InAs/GaAs, where QDs sit on top a wetting layer) but also in the "patches" between quantum well regions. The sample exhibits both QD-like and QW-like emission. QD emission has been confirmed for these samples at the wavelengths at which lasing is observed using low temperature μ-PL [99].

To summarize, we have characterized a set of microdisk lasers with quantum dot-containing active layers. Of the four samples investigated in this study, only samples 3QD-200nm and 3QD-120nm, containing three layers of QDs exhibited lasing behavior with thresholds as low as 0.28 mJ/cm_2 under pulsed excitation at room temperature. Our results suggest the critical importance of sufficiently high QD areal density. Although the lasing thresholds of these devices are exceptionally low, the sparser areal density of the quantum dot gain material, compared with quantum wells, may explain the yet lower threshold of 300 W/cm_2 reported by Tamboli et al. [11] for a QW microdisk laser under continuous wavelength excitation at room temperature. A better strategic design of the InGaN QD active layer material, matched to a smaller mode volume cavity (e.g., a photonic crystal cavity) may result in still lower values of lasing thresholds. We believe our studies are important not only for the efficient lasing performance demonstrated but also because of the important insights gained on the relative impact on lasing of the materials composition and structure, matched to the microdisk

design and fabrication.

6.4 Distinctive lasing signature of InGaN QDs

The following authors contributed to the work presented in this section, Alexander Woolf, Tim Puchtler, Dr. Igor Aharonovich, Dr. Tongtong Zhu, Nan Niu, Danqing Wang, Prof. Rachel A. Oliver, and Prof. Evelyn L. Hu. Alex and Tim fabricated, measured, and analyzed the devices. Nan, Danqing, and Igor assisted with data analysis and Tongtong grew the material. Rachel and Evelyn led the Cambridge and Harvard teams respectively.

In this section, we explore the lasing dynamics of 1μm microdisks containing either QDs and fragmented quantum well (FQW), FQW only, or QW only. The devices containing only QD+FQW exhibited the blue shifted lasing, which was originally observed in Section 6.3. This conclusively shows that the lasing from the microdisks is facilitated by QDs.

As discussed in Section 2.2, the family of III-nitride materials is promising for the realization of photonic devices including light emitting diodes and lasers [77, 109, 110, 113–115]. These systems have also been explored to engineer quantum emitters based on nitride quantum dots (QDs) that are active at room temperature and are suitable for applications in quantum information science [46]. The increased control of the growth of isolated InGaN QDs in a high quality GaN matrix has also resulted in the fabrication of high quality nitride microcavities including microdisks and photonic crystal cavities with emission at wavelengths in the blue spectral range (320nm-470nm), [70, 116]. Subsequently, electrically excited emitters and low-threshold lasers based on QDs as the

gain medium have been studied [20, 117]. However, in spite of the theoretical advantages of QD lasers related to the density of electronic states for QDs [18, 118–120], QD-microcavity devices still have higher thresholds than QW-microcavity devices for the nitride materials [11, 70, 116]. Furthermore, InGaN QDs formed through a modified droplet epitaxy (MDE) method are always associated with an accompanying fragmented quantum well (FQW) layer. Thus, it is important to determine the possible influence of the FQW layer on lasing properties in order to achieve a better understanding of the unique contribution from the QDs to the lasing mechanism. This work studies the lasing dynamics and the correlation between lasing threshold and lasing wavelength of microdisk lasers whose active areas comprise either QWs, FQWs or a combination of QDs with FQWs. Through a detailed comparison of lasing in devices with the same geometries but with different active areas, we find that the distinctive signature of QD facilitated gain is lasing at shorter wavelengths than the average of the background emission. The short wavelength emission is further confirmed by low-temperature, low-power PL measurements.

To investigate the dynamics of InGaN QD microcavity lasers, we simultaneously fabricated numerous 1.2 m diameter microdisk cavities from four wafers with identical cavity designs with the exception of the three active layers embedded in c-plane GaN. The active layers were either composed of $In_xGa_{1-x}N$ QWs, $In_xGa_{1-x}N$ FQWs or $In_xGa_{1-x}N$ QDs + $In_xGa_{1-x}N$ FQWs, respectively. Furthermore, the two QD+FQW samples (A and B) differed in the average density of QDs and in the percentage of FQW comprising the active layer. The volume of InGaN QW in each sample was analyzed by an atomic force microscope (AFM), with the percentage of the surface covered by the QW layer as: 100% (QW), 78.3% (FQW), 75.3% (sample A), and 63.9% (sample B). The QD density is estimated to be $2.8\pm0.1 \times 10^{10}$ cm^{-2} and $2.5\pm0.1 \times 10^{9}$ cm^{-2} for

samples A and B, respectively. To ensure that all samples exhibit similar room temperature PL peak emission wavelengths (450 ± 5 nm), the InGaN growth temperature was varied between 707 to 755 degrees Celsius to compensate for any loss of indium during annealing steps. Figure 6.10 shows AFM images of one uncapped active layer for each of the four samples. It is apparent that some portions of the QD+FQW samples

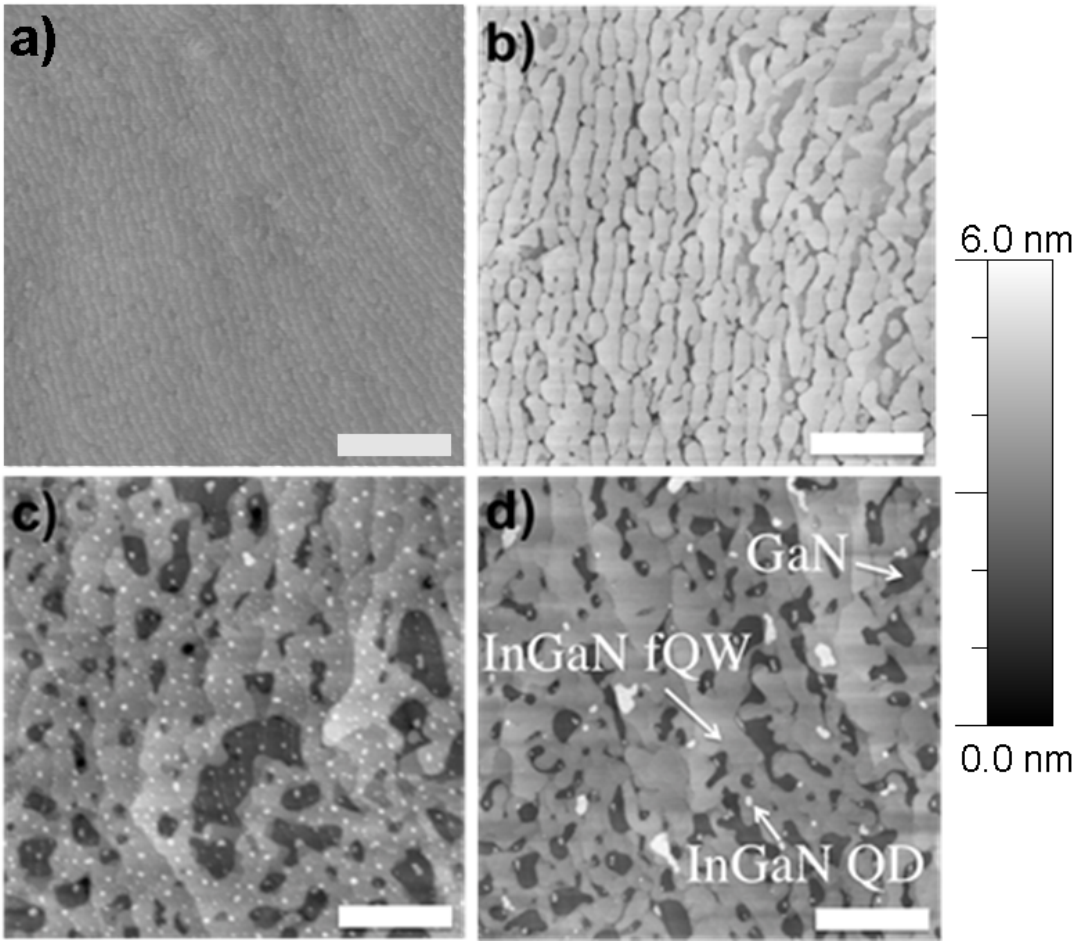

FIGURE 6.10: AFM images of uncapped active layers a) QW sample showing atomic terraces of the top surface of the InGaN QW, b) FQW, c) QD+FQW A and d) QD+FQW B. Scale bar is 500nm in width, with a vertical scale of 6 nm. The white bright dots in c) and d) are indium droplets which form InGaN QDs during growth of the GaN capping layer. The dark patches in b), c) and d) are bare GaN.

contain fragmented QW material or QDs alone, while other portions of the material may comprise a QD overlying FQW material. Regions of the InGaN FQW, QD and bare GaN are denoted in Figures 1 (e) and 5 (d).

AFM scans of the InGaN layers were performed on uncapped versions of the samples. The QW sample (Figure 6.10 a)) shows a smooth top surface of the InGaN QW (RMS roughness of 0.16 nm), whereas the other sample scans (Figure 6.10 b), c), d) show areas of both underlying GaN and the FQW surfaces. The depth of the FQW has been measured as 2.5 nm for all FQW samples. The details of the growth methods for the active regions are as follows:

InGaN QWs: To minimize the indium loss from the QW during barrier growth, GaN barriers were grown at the same temperature as the InGaN QWs. The nominal thickness for the QWs is 2.5 nm. This method results in continuous QWs with no visible well width fluctuation measured using Transmission Electron Microscopy (TEM) [121].

InGaN FQWs: 2.5 nm thick InGaN epilayers were grown and annealed at the growth temperature for 240 seconds in an NH3/N2 atmosphere prior to the growth of a GaN capping layer. The use of an NH_3/N_2 gas mixture was to ensure that no metallic droplets were formed during the annealing process. The annealed epilayer exhibits a network of interlinking InGaN strips aligned along the [11-20] direction as shown in Figure 6.11 (a) [122].

$In_xGa_{1-x}N$ QDs + $In_xGa_{1-x}N$ FQWs: Modified Droplet Epitaxy (MDE) was used for the growth of InGaN QDs in our samples. The full MDE technique is discussed elsewhere [32], however a brief description follows: a post-growth N_2 anneal is performed on a 2.5 nm InGaN QW layer causing the layer to be broken into regions of "pits" and regions of "fragmented QW", with metallic indium/gallium droplets being created across both of these regions. During the growth of the GaN capping layer, these droplets re-react with ammonia, forming InGaN QDs.

Microdisk cavities with equal diameters were consequently fabricated from these materials using reactive ion etching and photoelectrochemical etching to achieve the

final undercut structure of the microdisk. The fabrication of the microdisk cavities was identical to that described in Section 6.3. The microdisks were designed to be 1.2 μm in diameter and 200 nm in thickness in order to have multiple modes widely spaced over the entire emission spectrum. Figures 6.11 a) and b) show representative SEM images of the completed microdisk cavities. Figures 6.11 c), d) and e) are schematics of the active layers in the QW, FQW, and FQW+QD devices, respectively.

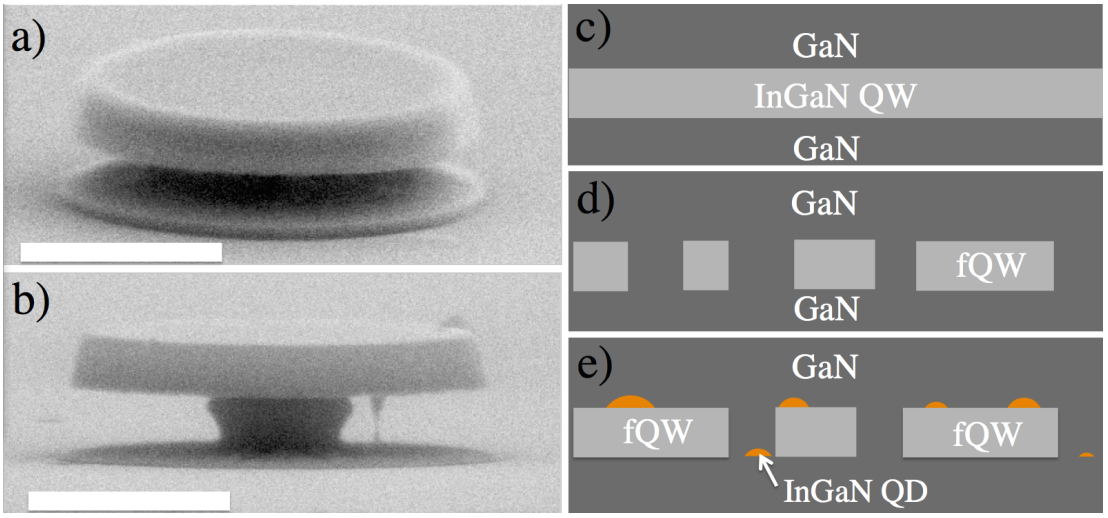

FIGURE 6.11: Images and schematic of devices examined in this work. a), b) SEM image of the top and side view of a completed 1.2μm GaN microdisk cavity. Scale bar is 500nm in width. c), d), e) Schematic of one of the three active layers embedded in the QW, FQW and FQW+QD samples respectively.

Room temperature PL measurements were carried out to measure the quality factor of the microdisk cavities. Quality factors as high as 5500 were measured from all samples, comparable with the best nitride microdisks currently achievable at these cavity dimensions [123]. The devices were measured using a 100x objective in a standard micro-photoluminescence (u-PL) setup in which a frequency-doubled pulsed titanium sapphire laser emitting at 380 nm was used to isolate the InGaN layers (bandgap 425 nm) from the GaN bulk emission (bandgap 360 nm).

Low temperature (4K), low power (1.4 μW) excitation measurements of FQW+QD microdisks suggest that the QDs predominantly emit light on the short wavelength side

of the gain spectrum. These data are shown in Figure 6.12, as well as data taken at a higher pump power (43 μW). Of all the active layer material considered here, only the FQW+QD A and B samples exhibited sharp peaks, identified as InGaN QD excitons in previous work [74, 124, 125]. These were consistently located on the short wavelength side of the emission spectrum and visible up to 40K. The short wavelength QD emission is believed to be a consequence of the MDE technique, as has been previously explained [126]. The excitons were observable only at the lowest incident pump powers, while the modes were clearly seen at both high and low pump powers. The dominant modes do not appreciably change as the pump power is raised from 1.4 to 43 μW power, but the gain spectrum does appear to shift by approximately 10 nm to shorter wavelengths, as can be seen in the Gaussian fits to the data.

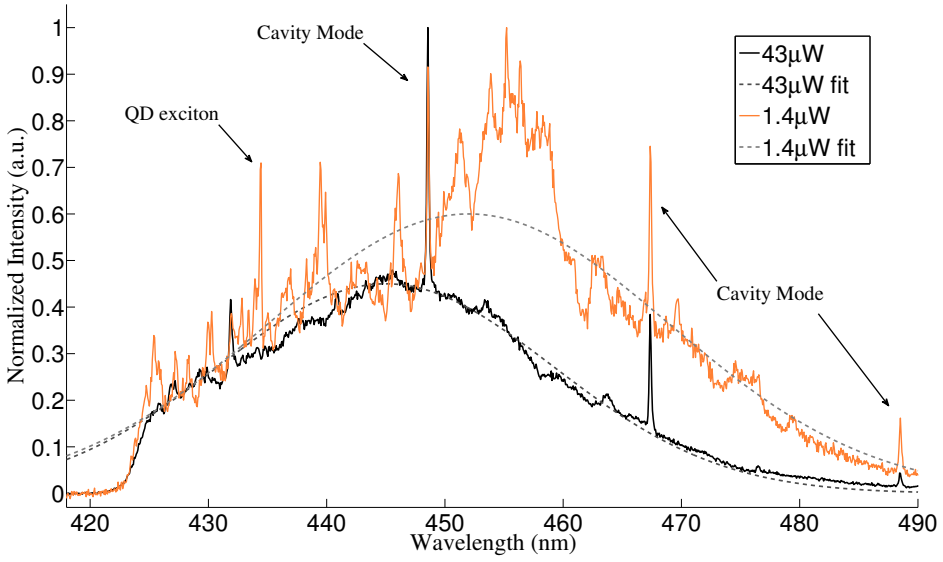

FIGURE 6.12: Normalized PL spectra from a FQW+QD (A) microdisk obtained at 4K. The exciton peaks are only visible at low pump powers (up to 10 μW), whereas the cavity modes are visible at all pump powers. Gaussian fits (dashed lines) show that the emission spectrum shifts to shorter wavelengths with increasing pump power.

Light in-Light Out (L-L) lasing curves were obtained at room temperature from 20 microdisks on each of the four wafers, allowing for the identification of the laser threshold as well as lasing wavelength. Representative room temperature microdisk

lasing spectra are shown in Figures 3 (a), (b) and (c) for a QW, FQW and QD+FQW device, respectively, with full L-L curves displayed in the insets. The log-log plot clearly indicates the evolution from spontaneous emission to lasing. Particularly notable in the data of Figure 3 is the transformation of the PL spectra for the three samples under progressively higher pump powers. Although there were across-sample variations in the widths and peak positions of the luminescence, in general at low input powers, all spectra display a broad luminescence peak, characteristic of the inhomogeneous widths of the QW and FQWs. Against these broad backgrounds are the distinctive, narrow peaks that modulate the broad PL spectra. These correspond to the modes of the microdisks, indicative of the coupling of the emitters to the surrounding cavity. The most prominent modes help to spotlight the optical transitions that are best coupled to the cavity at a given incident pump power, whether because of advantages in radiative emission rate, spatial overlap with a mode or resonance in frequency. For the QW, the most prominent mode appears near the peak of the PL distribution. This mode continues its prominence under higher pump powers, and ultimately defines the lasing wavelength. For the FQW sample, the dominant modes under low pump power are those at the long-wavelength tail of the distribution (471 nm). At a higher pump power, the dominant mode is blue-shifted (452 nm), closer to the center of the broad PL peak. Similar to the QW samples, lasing takes place at a wavelength close to the center of the broad gain spectrum. The PL spectra of the QD+FQW samples initially have similarities to the FQW (alone) samples: at the lowest pump power shown (75 μW), the spectrum in Figure 6.13 c) displays a prominent mode at the approximate center of the gain distribution (436 nm), with a small red-shifted mode at 452 nm. The distinctive change for the QD+FQW samples at the higher pump powers is the dramatic dominance of a peak at the very short wavelength limit of the emission spectrum. At 217 μW pump power, the prominent

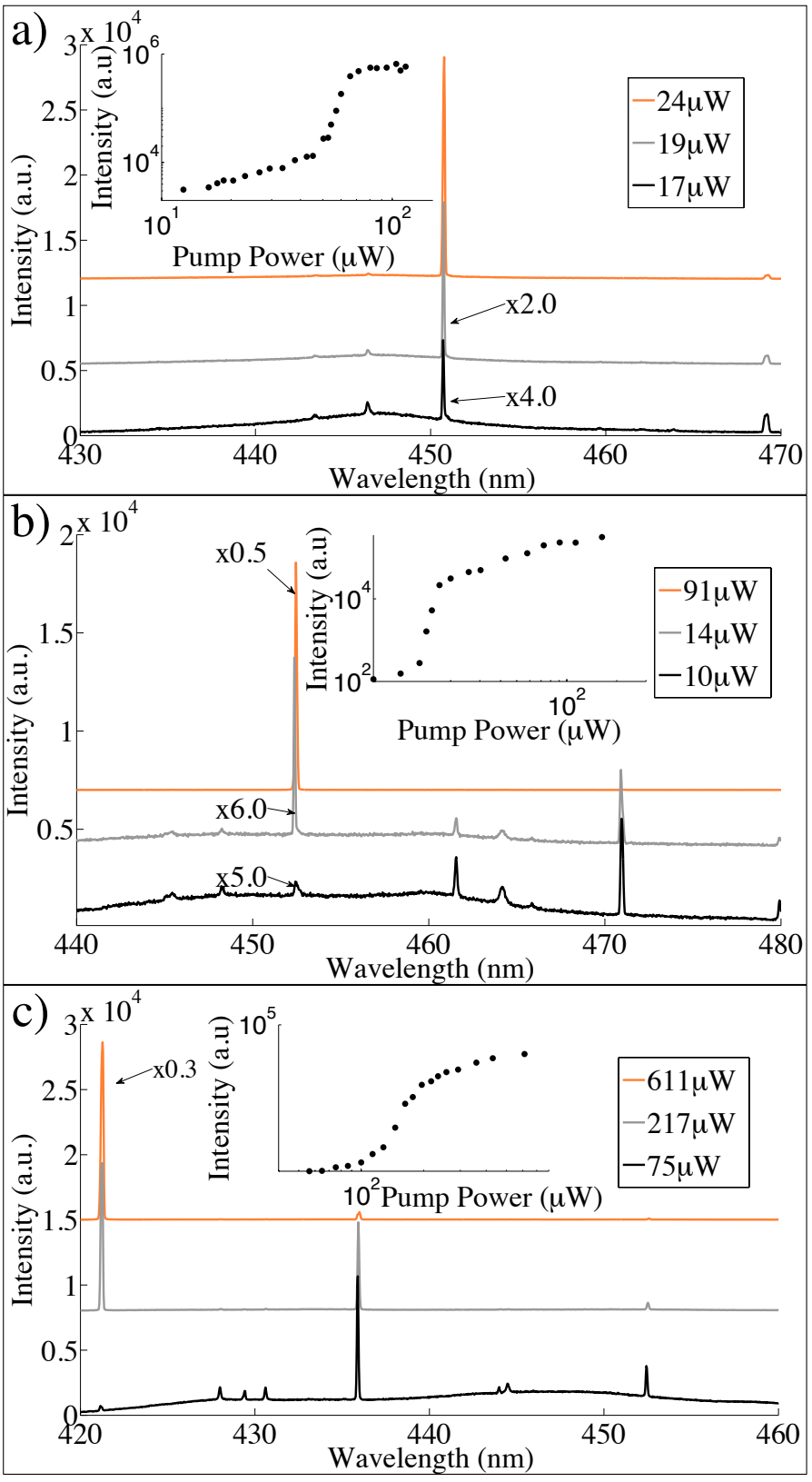

FIGURE 6.13: Lasing spectra from devices with varying gain media. a, b, c) Typical room temperature lasing spectra of QW, FQW and QD+FQW samples, respectively. Inset: full log-log lasing curves showing the three laser regimes of spontaneous emission, amplified spontaneous emission, and lasing.

mode has blue-shifted to 421 nm. This microdisk sample ultimately exhibits lasing at that wavelength. While the very broad gain spectrum reflects the optical emission of the entire range of FQWs and QDs that comprise the active layer, the dominant modes highlight the relative strengths of contribution of FQW and QDs as the incident pump power is changed. For the FQW+QD A and B samples, lasing ultimately occurs at wavelengths characteristic of the QDs, at wavelengths much shorter than the center of the room temperature gain spectrum. This distinctive behavior of these samples is observed over a significant sampling of microdisks as shown in Figure 6.14. A histogram of the wavelength of the lasing mode for each measured device is overlaid with the average background emission of the four samples. For FQW+QD A and B, the distribution of QD emission is also denoted. This distribution was determined by taking the average wavelength and standard deviation of QD exciton peaks, measured at low temperature. Finally, color bars represent the average lasing threshold of the microdisks within one histogram bin. While the lasing wavelengths for the QW and FQW devices are fairly equally distributed about the center-emission wavelengths for these materials, the lasing wavelengths of the FQW+QD materials are substantially blue-shifted (13 nm for sample A) from the broadband gain emission and instead are centered on the QD emission spectrum.

For clarity, for each active layer composition, the averaged data for the center of the gain spectrum, the lasing wavelength, and the lasing threshold are also tabulated in Table 6.1.

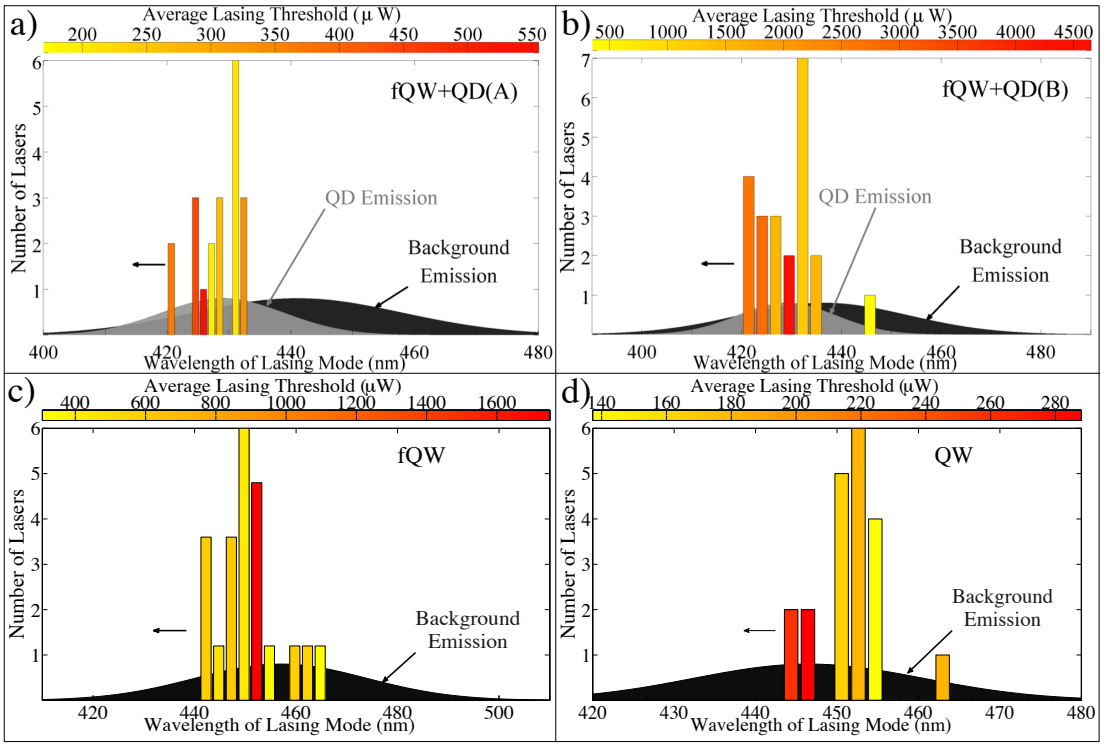

FIGURE 6.14: Histogram of the wavelength of lasing mode for each laser measured from each of the four samples a) FQW+QD(A), b) FQW+QD(B), c) FQW, and d) QW. The average lasing threshold of the devices in each histogram bar is denoted by the color map, with yellow and red corresponding to low and high thresholds, respectively. The normalized background emission spectrum is denoted in black and the QD emission spectrum is denoted in gray for FQW+QD(A) and FQW+QD(B).

Sample	Average wavelength of background emission (nm)	Average wavelength of lasing mode (nm)	Average Lasing Threshold (μW)	Threshold Range (μW)
QW	446 ±2.3	448±6.7	184	88-375
FQW	457± 3.5	451± 6.7	753	83-3600
FQW+QD A	441± 4.8	428± 3.8	303	118-815
FQW+QD B	437± 4.4	429± 6.3	2029	350-6175

TABLE 6.1: Center of background emission spectrum, average wavelength of lasing mode, and lasing threshold determined by averaging over the 20 microdisk lasers measured for each of the four active layer materials.

The information on lasing thresholds and wavelengths for the various active areas, as well as the evolution of the spectra at differing pump powers. provides significant insights into the important constraints on lasing in these microdisk devices. The evolution of the dominant mode from longer to shorter wavelengths as the pump power is increased reflects the interplay between and relative importance of the carrier capture cross-section

versus the efficiency and rate of radiative emission of those FQW regions of varying size. The larger area FQW regions are more effective at carrier capture, with subsequent emission at the longer wavelengths characteristic of their energy levels. Efficient carrier capture may be the dominant advantage at the lowest pump powers. However because of better spatial localization of the excitons, the radiative efficiency and, ultimately, the radiative rate will be higher for the smaller area FQWs [127]. As the pump power increases, carrier capture may be less influential than the higher radiative efficiency emission rate of the smaller area FQWs and the emission spectrum shifts to the shorter wavelengths characteristic of the energy levels of those FQW regions. The behavior continues for the FQW+QD sample. At higher pump powers, the QD emission into the mode at 421 nm becomes observable, and ultimately lasing at that wavelength is observed. We note the relatively short wavelength exciton emission of the QDs in Figure 6.13, as well as the blue-shift of the gain spectrum as the pump power changed from 1.4 μW to 43 μW. Thus, QD lasing at 421 nm is consistent with the low temperature PL spectrum of excitonic transitions from the QDs. In addition, previous work suggests that the threshold carrier density for QDs is lower than that of QWs [18, 31]. Thus at sufficiently high pump powers, the stronger spatial localization and higher radiative emission efficiency mediate the much lower relative carrier capture efficiency and result in lasing at the short wavelengths characteristic of the QDs. Such a mechanism may also explain why FQW+QD (B) lases closer to the center of the background gain spectrum: its QD density is 10x less than that of FQW+QD (A) and thus certain devices may not have the critical number of QDs to facilitate lasing. In this case, the device behaves similarly to a FQW device.

In conclusion, we have fabricated microdisk cavities containing QW, FQW and FQW+QD layers as the gain medium. The modal signatures of the respective spectra

show interplay between the large carrier capture cross section of larger area FQWs at the lowest pump powers, yielding precedence to the higher carrier localization of smaller area FQWs and QDs at the higher pump powers. In FQW+QD devices, we observe lasing at wavelengths centered on the QD gain spectrum, which is blue shifted from the peak of the broadband emission. We believe that this distinctive emission wavelength is a signature of QD lasing in these samples. These observations offer a method of distinguishing lasing from QDs from that of the MDE-associated FQWs and provide insights into the optimal nitride gain medium in order to achieve lower laser thresholds and improved device performance.

In the next Chapter we further investigate the FQW material as well as the mechanism which is limiting the microdisk quality factors. Surprisingly, the FQW active layers embedded within photonic crystal cavities exhibit a significantly lower threshold than QW active layers. We explain our working hypothesis for reason why in Chapter 7.

Chapter 7

Further experiments on GaN-based microcavities

7.1 Introduction

This chapter expands upon our experiments related to InGaN QD lasing presented in Chapter 6 and explores device designs to further improve the performance of GaN-based microcavities. The first section details the realization of record low lasing thresholds in the nitride systems using photonic crystal cavities (PCCs) with embedded InGaN fragmented quantum well (FQW) active layers. Surprisingly the PCCs with embedded FQW active layers exhibit lower lasing thresholds than identically fabricated quantum well (QW) devices. Next we present cavity QED experiments on an InGaN QD embedded within a GaN PCC. The lack of experimental evidence for weak or strong coupling naturally motivates the question of what mechanism is limiting the device performance. We then present experiments demonstrating that threading dislocations located within

the microdisk structure causes "whiskers," which in turn lower the quality factor of microdisk cavities. We also observe that 1 μm diameter microdisks with no whiskers have quality factors (Q-factors) no higher than 5400. We explore surface roughness, radiation losses and absorption as possible mechanisms leading the relatively low Q's. The chapter concludes with progress on tapered fiber experiments which can serve to conclusively diagnose the mechanism limiting the Q of GaN microcavities.

7.2 Low threshold lasing in photonic crystal nanobeam cavities

In this section we digress from the topic of devices with QD active layers to discuss the exciting and somewhat unexpected low threshold lasing from FQWs embedded within PCCs. In Section 6.4 we found that identically fabricated 1 μm diameter microdisks with FQWs and a high density of QDs, FQWs and QWs exhibited average lasing thresholds of 303 μW, 753 μW and 184 μW, respectively. This suggests that the QW active layers possess higher gain than FQWs and QDs and should therefore exhibit the lowest lasing thresholds within PCCs. Surprisingly upon fabrication of PCCs with either three FQW or QW active layers and comparable Q's, we found that the FQW exhibited over an order of magnitude lower lasing thresholds than QW. Upon consideration of the absorbed pump power into the device, we find that these devices exhibit the lowest lasing thresholds of any GaN-based device (9.1 μJ/cm^2). In short we attribute the high performance of the FQW to increased spatial localization of the photogenerated excitons, which acts to increase the gain and decrease the effects of non-radiative surface recombination.

The following authors contributed to the work presented in this section: Nan Niu, Alexander Woolf, Danqing Wang, Dr. Tongtong Zhu, Dr. Qimin Quan, Prof. Rachel A Oliver, and Prof. Evelyn L. Hu. Nan designed and fabricated the devices in addition to assisting with their measurement. Alex measured, and analyzed of the PCC devices and their respective spectra and lasing curves.. Danqing assisted in measuring the devices. Tongtong grew the material structure and Qimin contributed to the design of the PCC. Rachel and Evelyn led the Cambridge and Harvard teams respectively.

In this work, we demonstrate a GaN photonic crystal cavity (PCC) nanobeam laser with three layers of InGaN fragmented quantum wells (FQWs) operating with an ultra-low adjusted threshold of 9.1 μJ/cm^2. The choice of sample with InGaN FQW active medium is due to the associated disordered potential fluctuation that offers extra electronic confinement compared to quantum wells (QWs) and better spatial overlap with the cavity mode compared to quantum dots. Comparing the lasing threshold of nanobeam lasers containing three layers of continuous QWs with the same design, the FQW active layer material leads to lasers with thresholds that are more than an order of magnitude lower. With a modal volume close to unity, GaN/InGaN photonic crystal nanobeam lasers could provide exceptional ultra-low threshold operation in the blue.

The material design and growth was identical to the devices presented in Chapter 6. Each FQW was formed by growing a 2.5 nm thick InGaN epilayer at 710 degrees C and annealing at the growth temperature for 240 seconds in an atmosphere of NH_3 and N_2 prior to capping with 7.5 nm of GaN. Following annealing, the InGaN epilayer exhibits a network of interlinking InGaN strips aligned roughly along the [11$\bar{2}$0] direction [122], as demonstrated by the AFM scan in Figure 7.1, which shows an FQW sample prior to the growth of the GaN cap. The average width of the InGaN strips is approximately 70

nm. For more details on the lasing characteristics of FQW versus QDs and QWs within microdisks, please refer to Section 6.4.

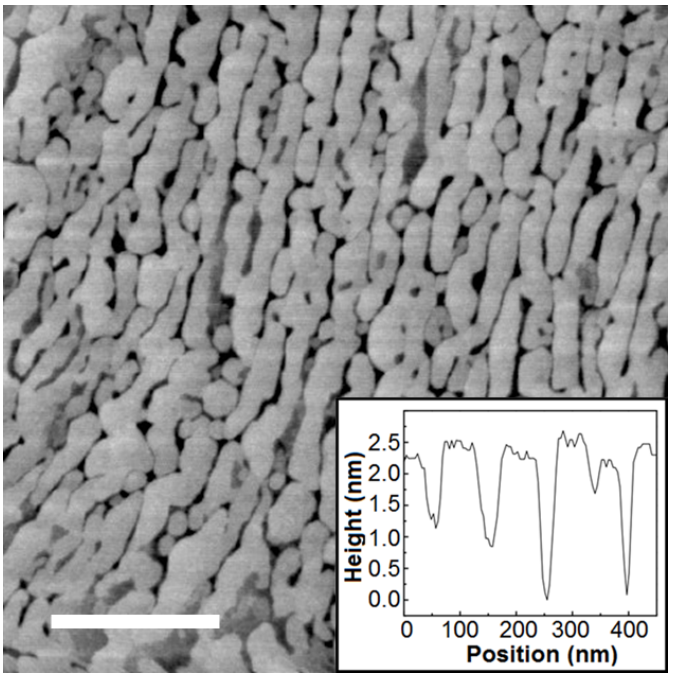

FIGURE 7.1: AFM scan of the annealed InGaN epilayer showing the fQWs before capping. The average width of the InGaN fQW strips is approximately 70 nm. The inset image shows an AFM line profile of a selected region on the as-grown annealed InGaN epilayer indicating a height variation of roughly 3 nm. Scale bar is 400 nm.

The InGaN FQW active layer is located in the middle of the cavity membrane sandwiched by the GaN barrier layers. The superposition of the nanobeam cavity pattern onto the FQW layers by dry etching results in the formation of isolated regions of InGaN. It is important to note that the indium composition is not homogeneous within one FQW strip. In fact, the center of a FQW island has a higher indium concentration then the edges. This leads to a smaller spatial extent of the confinement potential for the excitons compared to the size of an island. Figure 7.2 shows a schematic of the indium composition when viewed from the top and side, with the etched regions of the nanobeam denoted in orange. As the diffusion length of an exciton in bulk InGaN is approximately 60nm and there are a multitude of etched surfaces due to the PCC design, the non-radiative surface states can dramatically decrease the device performance with InGaN

QW's active regions. Therefore, the presence of the confining potential of the FQW can reduce the effective diffusion length of confined excitons, mitigating the negative effects of the etched surfaces.

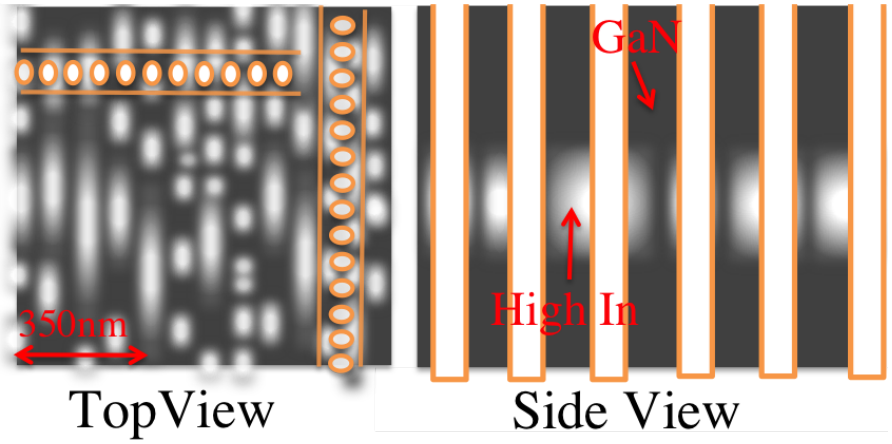

FIGURE 7.2: Schematic of the indium composition of the FQW active region viewed from the top and side. The white and gray colors correspond to regions of high indium and the GaN, respectively. The orange colored regions denote the material that is removed during the dry etching of the PCC. Thereby making the FQW more fragmented.

Figure 7.3 is a zoomed in schematic of Figure 7.2, with the lossy surface states denoted in orange.

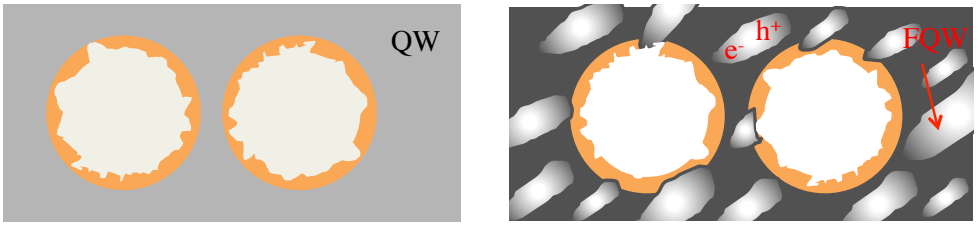

FIGURE 7.3: a) Schematic of the InGaN QW active region near a PCC hole. Carriers can easily diffuse to the lossy surface states, denoted in orange. b) Schematic of the InGaN FQW active region near a PCC hole, the confining potential reduces the fraction of carriers that can reach the lossy surface states.

The nanobeam cavity consists of a ridge waveguide perforated with gratings of cylindrical holes designed using a deterministic high-Q design [128, 129]. The cavity beam has a total length of 5.2 μm, comprised of 40 gratings with the same distance (130 nm) between neighboring holes. The width and thickness of the beam is 125 nm and

200 nm, respectively. The beam is symmetric to the middle plane, perpendicular to the beam direction. This intentional adiabatic tapering of the nanobeam design creates a bandgap that traps the optical field in the center of the beam to allow for maximum overlap between the mode and the active medium. FDTD simulations indicate that the resonance is at 419.48 nm, with simulated Q factor of 101,000 and modal volume (V) of $1.5(\lambda/n)^3$, where n is 2.5, the refractive index of GaN. Figure 7.4 a) shows the FDTD simulated intensity profile of the mode. The nanobeam is designed so that the peak field of the mode overlaps with the material region to allow strong light-matter interaction.

Fabrication of the photonic crystal nanobeams was carried out in a two-step dry etching transfer process followed by a photoelectrochemical (PEC) etch process to undercut the nanobeams and optically isolate them from the substrate. A schematic of the process is outlined in Figure 7.5.

First, 5 nm of SiO_2 is deposited on the as-grown GaN/InGaN wafer prior to evaporation of 15 nm of Ti. The Ti layer mitigates substrate charging during electron beam (E-beam) lithography. The 5nm SiO_2 spacer layer prevents the diffusion of the Ti through the GaN top surface. Then, negative resist (XR-1541) is spin-coated and E-beam lithography (Elionix F-125) is used to define the nanobeam and circular pad which serve as masks for the subsequent inductively coupled plasma (ICP) etch of the material in 25 sccm of N_2 and Cl_2 gas for an approximate depth of 300 nm. Subsequently, FOX-16 resist is spin-coated and E-beam lithography is again used to define a large rectangular pad aligned to the dry-etched nanobeam and circular pad. This pattern was subsequently dry-etched to a depth of approximately 200 nm, using the same conditions described above. The two-step process allows for application of a thin XR-1541 resist mask to better define the nanobeams. The second dry etch allows access to the $In_xGa_{1-x}N/In_yGa_{1-y}N$ superlattice which is selectively removed by the PEC etch,

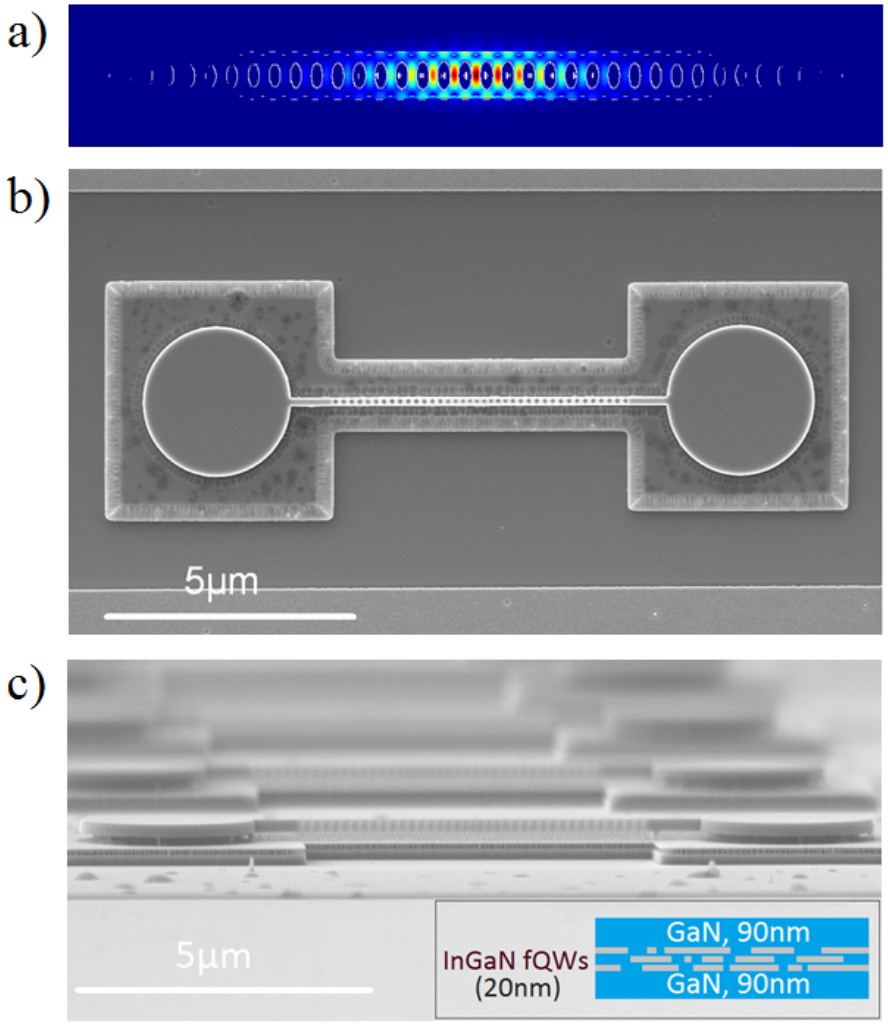

FIGURE 7.4: a) FDTD simulation of the intensity profile of mode at 419.48 nm. The modal volume (V) is $1.5(\lambda/n)^3$ and Q is approximately 101,000. b) SEM top-view image of the photonic crystal nanobeam. c) SEM side-view image of the photonic crystal nanobeam. The inset shows schematics of the cavity membrane. The broken lines represent the non-continuous nature of the FQWs. The inset shows schematics of the cavity membrane. The broken lines represent the non-continuous nature of the fQWs. Scale bar is 5 μm.

using a solution of 0.004 M HCl. This undercut-etch produces the final suspended photonic crystal structure. Details of the full PEC process can be found elsewhere [79]. Fig 7.4 b) and c) show scanning electron microscope (SEM) images of the photonic crystal nanobeam device.

Optical characterization of the nanobeams was performed using a frequency-doubled pulsed Titanium-sapphire laser emitting at 380 nm (200 ps pulse length, 76 MHz repetition rate) an energy below the bandgap of GaN and above the bandgap of the InGaN

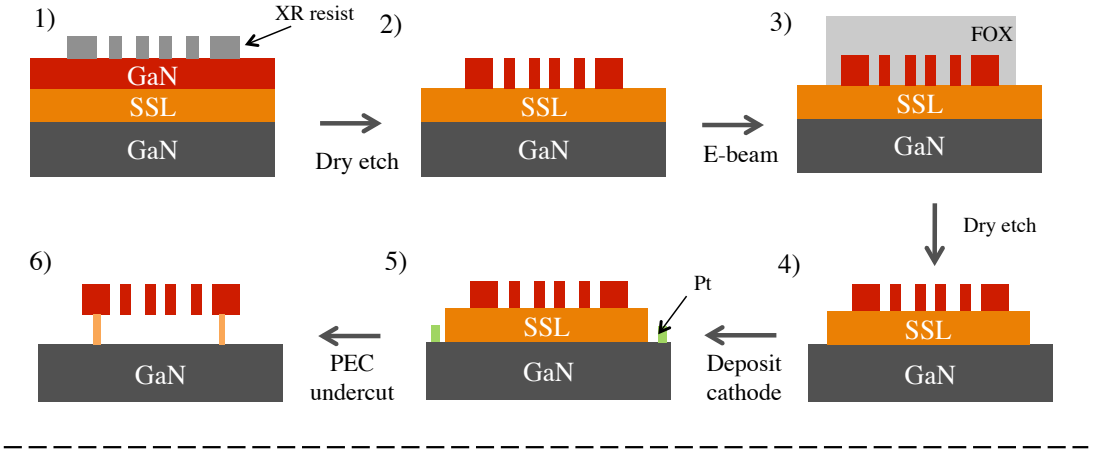

FIGURE 7.5: Process flow for the PCC fabrication. A two step e-beam/dry etch approach is used to allow for the definition of the holes with thin XR e-beam resist instead of thicker FOX which is needed to serve as a hard mask for the etch down to the GaN layer.

FQWs, through a long working distance objective (x40, NA=0.5). The emission from the photonic crystal was collected through the same objective and guided into a spectrometer. For later calculations, we will assume that all incident excitation power is irradiated upon the device and that the laser spot is a uniform Gaussian-shaped beam, 2.6 μm^2 in size. Lasing behavior in the nanobeam devices is clearly demonstrated through the dependence of the PL emission intensity as a function of incident pump power and linewidth narrowing [116]. This is on average 2.5 times more narrow than the linewidth below threshold. The Q's of the fabricated devices range from approximately 1300 to 1900. The quality factors of fabricated devices rarely match the simulated values, because it is difficult to incorporate the consequences of fabrication-induced and natural material imperfections into the simulations. Although the cavity modes were designed to have wavelengths of ~420 nm, the measured mode is positioned around 454 nm. The "red-shift" of the modes resulted from the slightly smaller radii of the fabricated air holes, compared to the originally designed value. Although, the red shifting of the mode actually benefited the lasing behavior through a closer match to the emission of the gain medium.

As the excitation power is increased beyond the lasing threshold, the intensity of the mode increases dramatically. At even higher power, the mode entirely dominates the background emission. A log-log plot of the output intensity versus input power for the device with the lowest threshold is shown in Figure 7.6 a) and demonstrates all three regimes of operation: spontaneous emission, amplified spontaneous emission and laser oscillation [106]. Considering only a portion of the laser beam spot covers the nanobeam, we estimate that the fraction of incident pump power absorbed by the device is approximately 0.9%, assuming a value of absorption coefficient 5×10^6 m^{-1}[130] with an average InGaN FQWs thickness of approximately 2.5 nm. This leads to adjusted lasing thresholds as low as 9.1 $\mu J/cm^2$. We have reasonably assumed that the incident power is absorbed in the InGaN layers which have a nominal total thickness of 7.5 nm. Given the possibility of some absorption centres in the GaN layers, a more conservative estimate of the absorption depth would be 10% of the thickness of the nanobeam. This would increase the adjusted thresholds by roughly a factor of 2.6. Figure 7.6 shows three different spectra taken: below threshold, at threshold and above threshold. The broad background at low pump power is the signature emission of the active medium which couples to the leaky modes of the cavity. At increased pump power, there is a slight blue-shift of the peak, which may be related to screening of the built-in electric field. In addition, the linewidth of the mode narrows significantly, from 0.32 nm to 0.1 nm, at the onset of lasing, indicating an increased temporal coherence of emission in the lasing regime. These data unambiguously demonstrate the achievement of lasing behavior in our device.

At pump powers far above the lasing threshold, the slope of the curve of laser intensity versus pump power levels off, as shown in the inset of Figure 7.6 b). The linewidth of the lasing mode is generally broadened. This indicates heating effects and

the generation of excess carriers. The linewidth broadening can be attributed in part to the resulting changes in the effective refractive index and enhanced free carrier induced absorption [131].

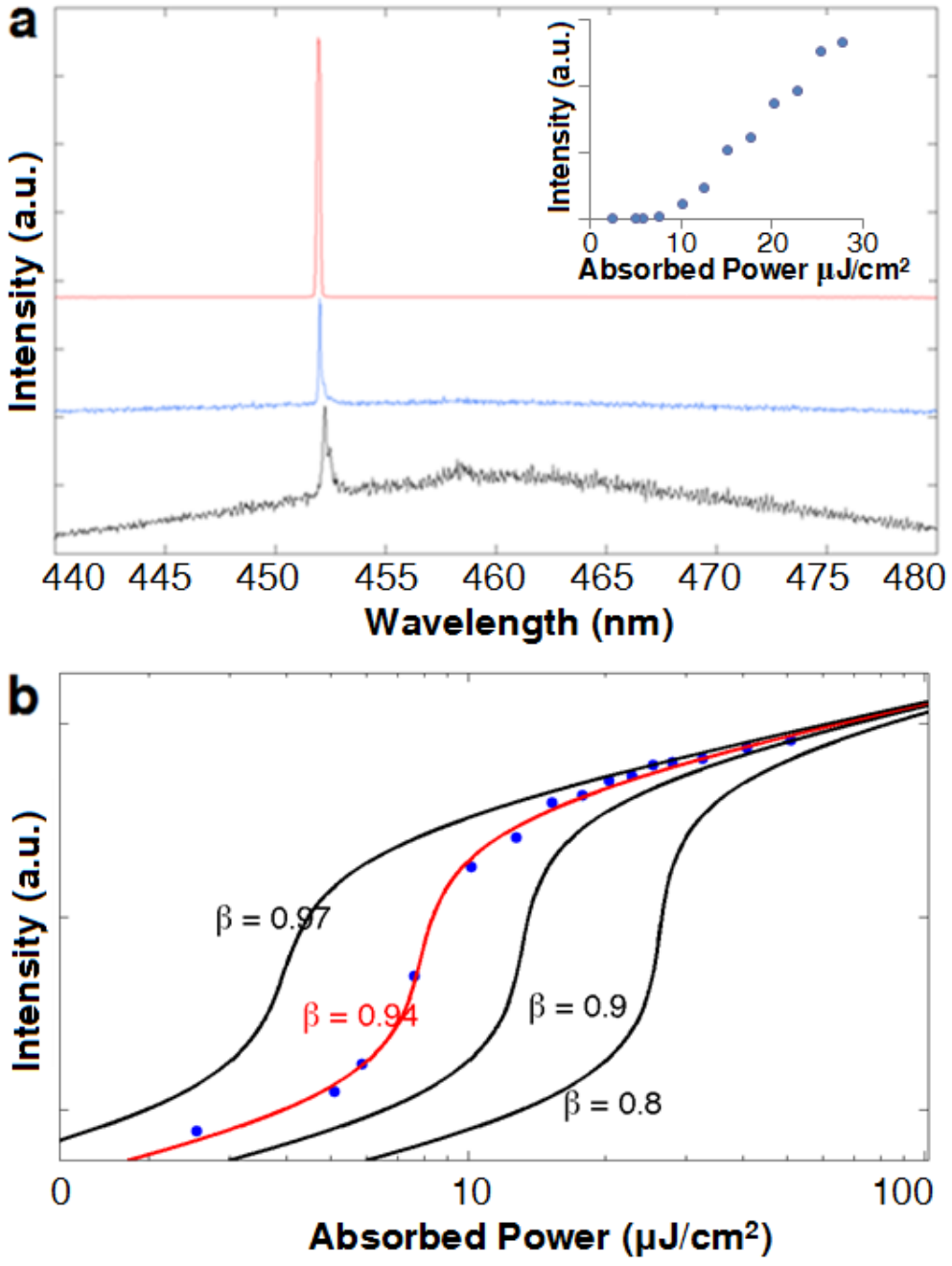

FIGURE 7.6: Log-log plot of the lasing behavior and emission spectrum of a measured nanobeam laser. a) spectra of the nanobeam at three pump regimes: below threshold, at threshold, and above threshold. Linewidth narrowing is clearly observed. The inset graph shows a linear plot of the lasing behavior. b) log-log plot of the emission intensity vs. pump power clearly indicating three regions of operation: spontaneous emission, amplified spontaneous emission, and laser oscillation.

Fits of the experimental data to the laser rate equations suggest a spontaneous emission factor as high as $\beta = 0.94$. As numerous material properties, such as the threshold current density (n_{th}), differential gain coefficient (G_0) and non-radiative lifetime (τ_{nr}), of the FQW active layers are unknown, we use the fitting method described in reference [132] which lumps the unknown laser parameters into two variables: ξ and γ. Qualitatively, ξ can be interpreted as the photon number in the lasing mode at transparency. On the other hand, γ is the photon loss rate. Eq. 7.1 is the analytical dependence of the pump current (I) as a function of photon number (p).

$$I = \frac{q\gamma}{\beta}\left[\frac{p}{1+p}(1+\xi)\left(1+\beta p+\frac{\tau_{sp}}{\tau_{nr}}\right)-\xi\beta p\right] \tag{7.1}$$

We assume that $\tau_{nr} \gg \tau_{sp}$ and implement a least squares fitting algorithm to obtain the best fit to the experimental data. However, before we can perform the fit, there is a scaling parameter between the photon number within the laser device (p) and the intensity of collected photons which is obtained with PL (Intensity (a.u)). As the scaling parameter is unknown, the fitting curve is scaled vertically in order to make the photon density of the analytical model equal to the intensity of the lasing curve for the data point collected at the highest pump power. Furthermore, before the fit is performed the incident pump power (P_{in}) must be converted to the pump power actually absorbed by the laser device (P_{abs}). This conversion must account for the fraction of the laser spot that is intercepted by the nanobeam cavity (A_{int}), as well as the fraction of absorbed power (η). Eq. 7.2 shows the relationship between the pump power and the absorbed pump power in the laser device.

$$P_{abs} = \eta A_{int} P_{in} \tag{7.2}$$

A_{int} is straightforward to calculate, as a diffraction limited focused pump laser emitting at 380 nm the laser spot size is 2.64 μm^2. The approximate cross sectional area of a 125 nm wide beam with 35 nm etched holes (A_{beam}) and corresponding A_{int} is is given in Eq. 7.3.

$$\begin{aligned} A_{beam} = 125[nm] \cdot (2 * 290[nm]) - 2\pi \cdot (35[nm])^2 = 0.64[\mu m^2] \\ A_{int} = \frac{A_{beam}}{A_{spot}} = 0.245 \end{aligned} \tag{7.3}$$

The fraction of absorbed power is calculated by accounting for the amount of light reflected from the air-GaN membrane interface as well as multiple reflections of light within the cavity. In order to estimate the number of electron-hole pairs which are actually generated in the device, η also accounts for the thickness and absorption coefficient of the FQW active medium. Figure 7.7 shows a schematic used to calculate (η) where R is the fraction of reflected light between GaN and air, d is the total thickness of the active region, and α is the absorption coefficient of the active region.

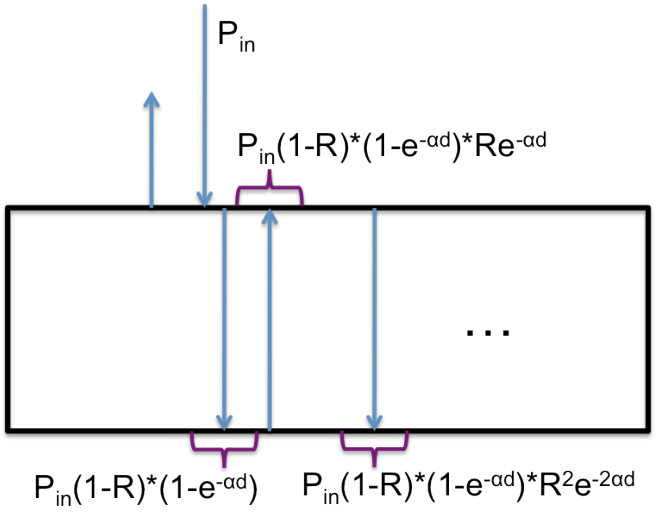

FIGURE 7.7: Schematic showing the derivation of the fraction of absorbed power

By identifying the presence of the geometric series, one has the functional form of η which is given in Eq. 7.4.

$$\begin{aligned} \eta &= (1-R)\cdot(1-e^{-\alpha d})\cdot(1+Re^{-\alpha d}+R^2e^{-2\alpha d}+...) \\ \eta &= \frac{(1-R)\cdot(1-e^{-\alpha d})}{1-Re^{-\alpha d}} \end{aligned} \tag{7.4}$$

We insert the following parameters into Eq. 7.4: α=5×10^4 cm^{-1}, d = 7.5 nm^2, and R = 0.18 one has η = .034. Because of uncertainties in the actual thickness of the InGaN QWs and fQWs upon growing the capping GaN layer, and because there may be absorption levels in the GaN itself, it is also possible to extend a conservative estimate of d to be 20 nm, or 10% of the physical thickness of the nanobeam. Following this conservative estimate, η is then computed to be approximately .093. Plugging our values for η and A_{int} into Eq. 7.2 one arrives at $P_{abs} = 0.023 \cdot P_{in}$. To ensure that the units are consistent, the fit is performed in with the absorbed pump power in units of Watts. This necessitates that the pump current (I) also be converted to units of Watts. Since we have already accounted for the absorption in the laser, each 380 nm photon (5.228×10^{-19} J/photon) creates one electron-hole pair. Multiplying by the electric charge, one Watt of Pump power is equivalent to 0.3 Amps of current. Inverting the relation we now have I in units of Watts, which is the same unit as the absorbed pump power. The fixed parameters are the spontaneous emission lifetime $\tau sp = 1ns$ (which is measured with a time-resolved photoluminescence setup), modal volume $V = 9\times10^{-21}m^3$. The best fit is obtained for the following following free parameters: γ = 8.5e12 1/s, and $N_{th} = 3\times10^{27}$ m^3, and β = 0.94. Where $\xi = N_{th}\beta V/\gamma \cdot \tau sp$. As a note, one could also account for the surface recombination velocity given in Eq. 3.7 if the other material properties were known and the full rate equation model in terms of the A, B, C model given in Eq. 3.6 could be applied. The reasons for the high spontaneous emission factor is discussed in

Section 4.2 but in brief, it is due to the small modal volume, the high quality factor of the mode and the presence of a photonic band gap which suppresses unwanted spontaneous emission pathways.

All of the 50 FQW nanobeam lasers probed demonstrated lasing. Although we did not fully characterize every device on the sample, we studied five nanobeams in detail. These all demonstrated lasing. Their characteristics are summarized in Table 7.1. The quality factor, Q, ranges from 1300 to 1900. The lasing thresholds range from 9.1 μJ/cm^2 to 27.2 μJ/cm^2 (adjusted for absorbed incident power), and the lasing wavelengths are relatively consistent at around 454 nm. As a note, during the experiment the power is measured in units of Watts. In order to convert from μW to $\mu J/cm^2$, we use the fact that the repetition rate of 76 MHz is long compared to the lifetime of the carriers. Therefore the PCC laser turns off after each pulse of the pump laser. Therefore 1 μW of pump power is equivalent to 1.32 J/pulse. Using the fact that the area of the beam (A_{beam}) is the active area of the device. We then have the conversion factor that 1 μW of absorbed pump power is equivalent to 20.3 $\mu J/cm^2$.

PCC #	Lasing Wavelength (nm)	Q (below theshold)	Adjusted threshold ($\mu J/cm^2$)
1	456	1333	27.2
2	453	1905	9.3
3	454	1354	12.6
4	452	1451	9.1
5	452	1605	19.8

TABLE 7.1: List of the lasing wavelengths and quality factors of the five measured cavities below the lasing threshold, as well as the computed lasing threshold of the devices.

We note that nanobeam structures identical to those described here, but which incorporated three layers of homogeneous quantum well material of the same stoichiometric composition showed a far poorer percentage of lasing devices. Roughly 30% of the devices showed clear lasing behavior. Those structures that did undergo lasing required

an order of magnitude higher input power. The measured average adjusted threshold for the QW nanobeam lasers is 203.6 $\mu J/cm^2$, more than an order of magnitude higher than the average threshold of the FQW nanobeam lasers. Figure 7.8 shows lasing curves for a typical FQW and QW PCC device superimposed on the same plot. The FQW material clearly outperforms that of the QW.

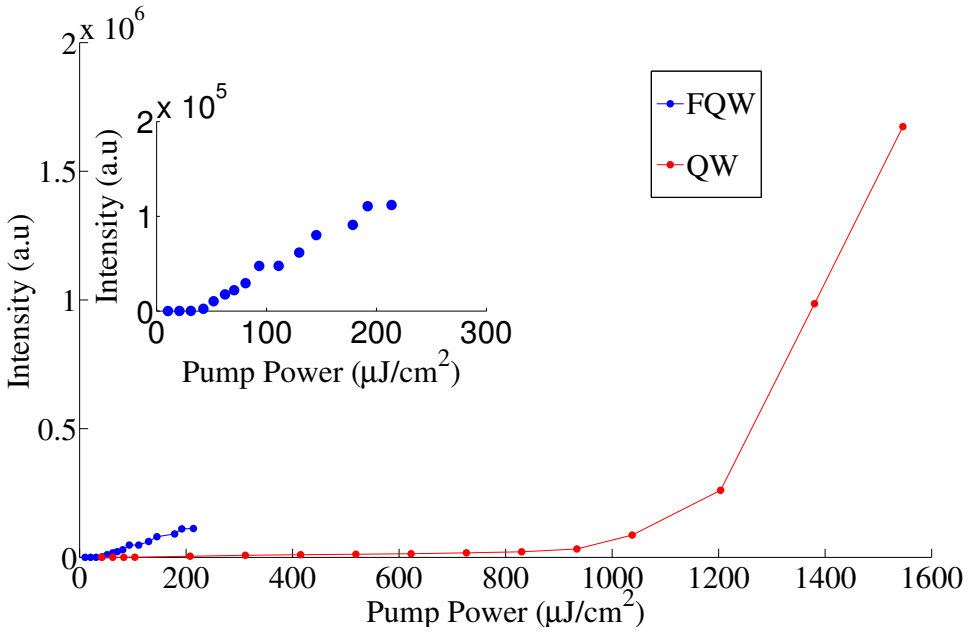

FIGURE 7.8: Superimposed lasing curves of a typical FQW and QW PCC laser. Inset: Zoomed in lasing curve the of FQW lasing curve.

Although a more complete comparison of these devices will be given in a future paper, we remark that the geometry of the nanobeam and the spatial profile of the modes make these structures more sensitive to non-radiative recombination through surface states. The FDTD simulation of the modes in the nanobeam, shown in Figure 7.4 a), indicates the overlap of the mode with the boundaries of the etched holes in the nanobeam. Therefore, it is expected that the efficiency of photon generation in the cavity would be strongly limited by non-radiative recombination with surface states. Boroditsky et al., deduced values of the surface recombination velocity, S, for InGaN to be $\sim 3 \times 10^4 cm/s$ [133]. When the holes in the nanobeam are formed through

ion-assisted techniques, such as were used here, S was found to increase by a factor of two. Nevertheless, the influence of surface recombination alone, without the addition of etch-induced damage, can be shown to increase the thresholds of microcavity lasers. Thus, although the nanobeam cavity design was chosen for its high Q and small modal volume, the close spatial proximity of the modes to the surfaces of the structure imposes constraints on the optical efficiency of the gain medium. In the FQW, the existence of isolated regions of active material can mitigate carrier diffusion to surface states, resulting in improved lasing thresholds and potentially leveraging the benefits of such cavity. Future work will explore the exact mechanism for the enhanced FQW performance.

In conclusion, we successfully demonstrated an ultra-low threshold InGaN/GaN photonic crystal nanobeam laser. An obvious transition from spontaneous emission to lasing was observed with clear linewidth narrowing. The ultimate device has an adjusted threshold of 9.1 $\mu J/cm^2$ and is the lowest recorded lasing threshold in this material system. We attribute the dramatic reduction to the ultra-small modal volume of the cavity and the reduction in the number of competing modes. Moreover, we observed an order of magnitude reduction in lasing threshold on nanobeams fabricated from FQWs compared to QWs because of an increased carrier confinement. This is expected to reduce the impact of surface states. These observations underscore the advantages of this photonic crystal nanobeam design, matched to the three layer FQW gain material. Matching nanocavity geometry to the gain medium provides GaN/InGaN lasers with excellent performance. These devices are potential candidates for efficient, on-chip optical sources in the blue spectral region.

7.3 Cavity quantum electrodynamics attempts

The following authors contributed to the work presented in this section: Alexander Woolf, Tim Puchtler, Dr. Kasey Russell, Nan Niu, Dr. Tongtong Zhu, Prof. Rachel A Oliver, and Prof. Evelyn L. Hu. Kasey and Alex designed and built the cryostat gas tuning setup. Tongtong grew the material wafers and Nan designed and fabricated the PCC. Tim and Alex conducted the tuning experiment and data analysis. Rachel and Evelyn led the Cambridge and Harvard teams respectively.

As we have mentioned previously in Section 2.2, an InGaN QD coupled to a photonic mode could potentially serve as the basis for a room temperature thresholdless polariton laser or solid state quantum computer. The interaction between the cavity mode and the exciton transition is critical towards the realization of such schemes. For quantum computing applications the QD-cavity system must be strongly coupled in order to ensure efficient optical initialization, manipulation and readout of the the QD qubit state. For polariton lasing, an anti-crossing of the exciton and cavity photon state is necessary in order to create the lower polariton branch where exciton-polariton condensation occurs. Following the approach described in [6], we can use the formula for the Rabi frequency given in Eq. 7.8 (which was originally derived in Eq. 2.4) to infer which cavity parameters are necessary in order to achieve strong coupling.

$$\begin{aligned} \Omega &= 2\sqrt{g_0^2 - \left(\frac{\delta\omega_0 - \delta\omega_c}{4}\right)^2} \\ g_0^2 &= \left|\langle \vec{d} \cdot \vec{E} \rangle\right| = \frac{q^2 f}{4\epsilon m_0 V} \end{aligned} \tag{7.5}$$

For the Rabi frequency to be purely real, the term under the square root in Eq. 7.8 must be greater than or equal to zero. This places the following requirement for the cavity Q and modal volume (V) given in Eq. 7.6, assuming an infinitely sharp emitter

linewidth ($\delta\omega_0$=0) and zero detuning of the cavity mode.

$$\begin{aligned} \frac{q^2 f}{4\epsilon m_0 V} &\geq \left(\frac{\omega}{4Q}\right)^2 \\ \frac{Q^2}{V} &\geq \frac{\epsilon m_0 \omega^2}{4 f q^2} \\ \frac{Q^2}{V} &\geq 2.96 \times 10^{24} \end{aligned} \tag{7.6}$$

Where in the last equation we have inserted the following values for the InGaN QD oscillator strength, $\tau = 1$ ns, $n = 2.51$, $\omega = 4.15 \times 10^{15}$ 1/s, $a_b = 3.4$ nm, $a = 0.33$ nm, yielding $f = 4068$.

For a GaN PCC with a modal volume $V = 1.5(\frac{\lambda}{n})^3 = 9 \times 10^{-21}$ m^3, the Eq. 7.6, suggests that $Q \geq 163$. Similarly for a 1 μm GaN microdisk with a modal volume of $V = 5.6 \times 10^{-20}$ m^3 Eq. 7.6 yeilds $Q \geq 409$. While our devices surpass these constraints, it is important to note that these values represent a best case scenario. Linewidth broadening of the QD in addition to a non-ideal spatial overlap or dipole orientation between the QD and cavity mode could necessitate much higher Q values for our microcavity devices.

In order to determine if the QD-cavity systems is coupled, it is necessary to spectrally tune the system in and out of resonance. If the system is in the weak coupling regime, in resonance the change in the photonic density of states due to the presence of the cavity mode will cause an increase in the radiative litetime (τ_0) of the QD exciton. If the system is in the strong coupling regime, an anti-crossing of the exciton and cavity mode will occur. Furthermore, as discussed in Section 2.2.2, a strongly coupled exciton-cavity mode can exhibit thresholdless polariton lasing. Therefore once the exciton and cavity mode are in resonance we can attempt to observe effects similar to those in reference [134], where polariton lasing of a single InAs QD within a GaAs PCC mode

was observed. Another example of a strongly coupled InAs QD embedded within a GaAs PCC exhibiting an anti-crossing is demonstrated in reference [135].

In order to tune the system into and out of resonance, we employ a nitrogen gas tuning technique. The full experimental setup and procedure is given in Appendix A, however in brief, the system is cooled to 4K and then nitrogen gas is flowed into the cryostat. As the temperature is below the freezing point of nitrogen, the nitrogen condenses on the surface of the PCC. The refractive index of the condensed nitrogen causes the cavity mode to red-shift. This process is entirely reversible by heating the system and allowing the nitrogen to evaporate.

To test for the presence of weak coupling, the QD exciton is first identified, using the same technique described in Figure 6.12 and then spectrally filtered using a tunable filter. After filtering, a time resolved photoluminescence measurement is performed and the lifetime is obtained via a least squares fitting algorithm. Figure 7.9 a) and b) show an unfiltered and filtered PL spectrum and lifetime of an InGaN QD embedded within a GaN PCC. The device design is the same as in Section 7.2, however the active medium is three layers of InGaN QDs instead of FQW. Next, the cavity mode is red-shifted into

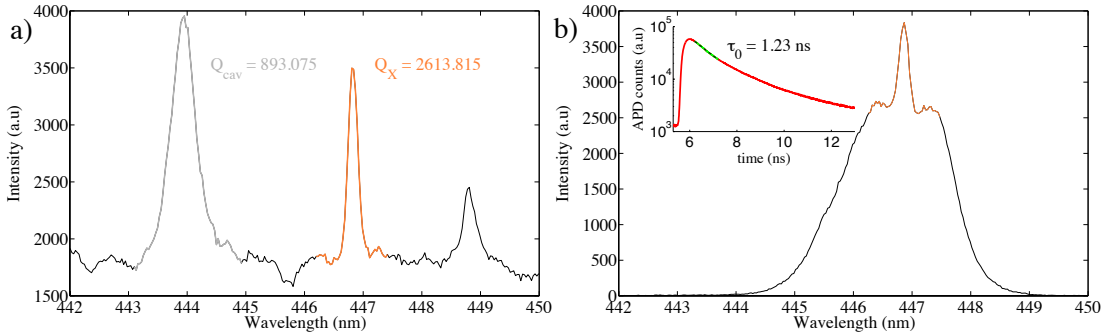

FIGURE 7.9: a) PL spectrum of a InGaN QD embedded in a GaN PCC. The exciton and cavity mode are denoted in orange and gray respectively, with annotated Q values. b) After filtering only the desired exciton emission remains, and a lifetime measurement is performed. For clarity we have only shown the fastest decay component in green (inset).

resonance with the exciton and the same procedure outlined above is repeated. Figure

7.10 shows a series of PL spectrum, where the mode is tuned into resonance with the QD exciton. The accompanying lifetime traces show no evidence of weak coupling, or strong coupling for that matter.

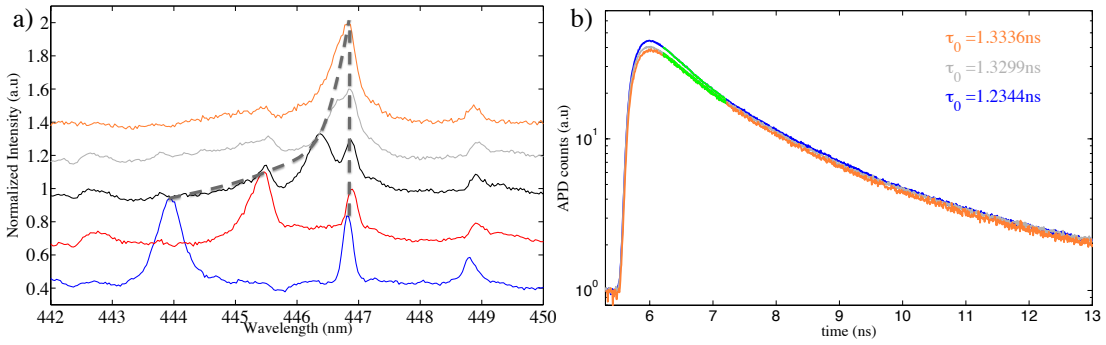

FIGURE 7.10: a) PL spectra showing the tuning of the PCC mode (left dotted line) into spectral resonance with the QD exciton (right dotted line). b) corresponding lifetime traces color coded to a), no significant change in lifetime is observed. For clarity we have only shown the fastest decay component in green (inset).

There may be a variety of reasons why no lifetime modification was observed. Our current hypothesis is that the QD exciton was not spatially located in the region of high field of the PCC. As the beam spot is 2.6 μm^2 in size, it is possible that the exciton emission could be collected from a region of the beam where there is negligible electric field intensity from the cavity mode, which can be seen in Figure 7.4 a).

There are three main options to overcome these challenges in the future. First, the QD could be located in the PCC, using an optical or CL technique. This would require a great deal of work, but eliminate the possibility that the QD is not located in the high field region of the PCC. The second option is to increase the Q of the the PCC in order to increase the coupling between the PCC and the cavity mode. The final option is to further decrease the linewidth of the QD exciton, however this will only be necessary if the Q of the PCC can be increased to values higher than the currently achievable QD linewidths.

In the next sections, we focus specifically on the issue of low Q in GaN-based optical microcavities. Using the techniques of cathodoluminescence and tapered fiber evanescent coupling we can gain further insights into what mechanism is limiting the cavity Q.

7.4 Dislocation dependent quality factors in GaN-based microdisk cavities

The following authors contributed to the work presented in this section Tim Puchtler, Alexander Woolf, Dr. Tongtong Zhu, Prof. Rachel A. Oliver, and Prof. Evelyn L. Hu. My contribution to this work included fabrication, PL measurement and FDTD simulations of the microdisk devices. Tim also fabricated and conducted PL as well as cathodoluminescence (CL) measurements, and data analysis. Tongtong grew the material and performed the high resolution CL measurements of the microdisk devices. Rachel and Evelyn led the Cambridge and Harvard teams respectively.

While the GaN materials system is notable for both strong internal fields [136] and dislocation densities which would be expected to destroy device performance in other materials systems, some nitride devices, such as light emitting diodes, nevertheless demonstrate high efficiencies and robust performance. However the mechanism underlying this is still debated [131]. In previous work, statistical analysis of a score of microdisk devices found an anti-correlation between the quality factor (Q) of those devices and the overall dislocation density of the material comprising the sample. However, the reasons underlying that anti-correlation were not fully discussed, nor were the dislocation densities of individual disks measured [2]. Here we expand upon such work by the novel exploitation of CL techniques to help make correlations between the locations of TDs in individual

microdisks with the Q of that specific device, allowing unprecedented understanding of the effect of TDs in these devices.

The material design and growth was identical to the devices presented in Chapter 6, with the exception that these structures were grown atop n-doped c-plane GaN/Al_2O_3 pseudosubstrates which have been deliberately grown to achieve different densities of threading dislocations (3.0 $\times 10^8$, 5.6 $\times 10^8$ and 5.3 $\times 10^9$ cm^{-2}) measured by AFM scans of silane treated pseudosubstrates [137]. Microdisk cavities were formed concurrently from each sample using techniques that have been previously described in Chapter 6. Figure 7.11

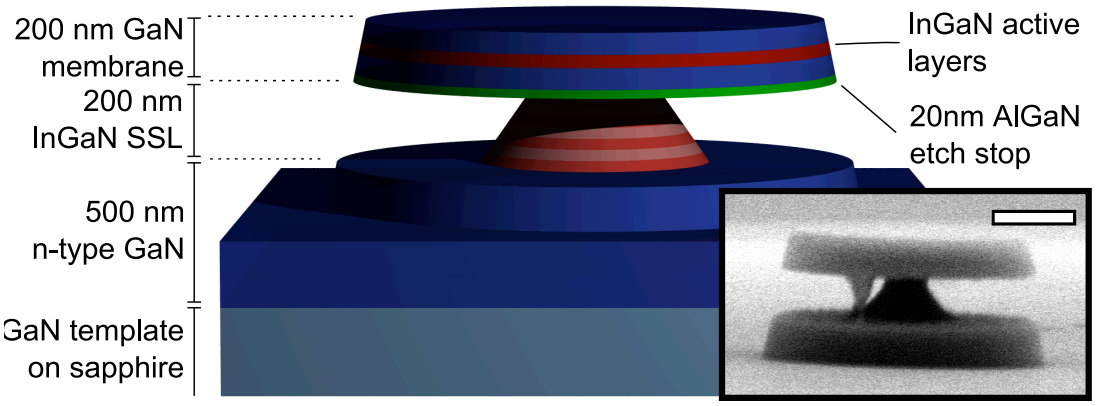

FIGURE 7.11: Schematic of GaN microdisk with its respective epilayers (created by Tim Pultcher). The suspended disk membrane has a thickness of 200 nm and diameter of 1.2 um, containing either three QD or QW active layers. (Inset) SEM image of a completed microdisk from the side. Scale bar represents 400 nm.

Six samples with differing InGaN active regions were investigated, separated into two sets: three samples contained QDs formed by "droplet epitaxy" grown on pseudosubstrates of varying dislocation density [32, 99]. Three QW samples with differing growth conditions were grown on low dislocation templates (approximate density 3.0 $\pm$ 0.3 $\times 10^8$ cm^{-2}). The QW samples were selected to investigate whether InGaN quantity or defect inclusion would affect cavity quality factors, consisting of QWs with: GaN capping layers grown at a single temperature (740 degrees Celcius); capping layers which

were temperature ramped during growth (725-860 degrees Celcius) to reduce defect incorporation; a post-growth NH_3 anneal, causing fragmented QWs (FQWs). A student's t-test comparing the mean quality factors of the different QW samples suggests that there is no statistically significant effect ($p = 0.78$) of the different growth treatments on the analysis presented in this work.

Microdisk resonators were investigated using separate microphotoluminescence (μ-PL) and CL setups. Markers on the fabricated samples were used to identify the same disk in both setups. μ-PL measurements were made using a pulsed frequency-doubled titanium-sapphire laser emitting at 380 nm (76 MHz repetition rate, 200 ps pulse duration) through a high (0.90) numerical aperture (NA) objective normal to the surface of the microdisk. We estimate the pump laser spot size to be 500 nm^2. The collection path was through the same objective. A long pass filter was placed before the spectrometer to remove any signal from the pump laser. All μ-PL measurements were performed at room temperature, with almost all ($> 95\%$) of the measured disks demonstrating whispering gallery modes (WGM) superimposed on the inhomogeneously broadened QD or QW emission. CL measurements were obtained with a Philips XL30 SEM, equipped with a Gatan MonoCL4 using a low accelerating voltage (3 kV) and operating at room temperature, with the exception of the data in Figure 3. This was obtained on an Attolight CL system at 3kV and a temperature of 15 K [138].

μ-PL and corresponding CL spectra were taken from the microdisks by use of markers to identify individual cavities and subsequent imaging of the disks was performed by SEM-CL (Figure 7.12). Threading dislocations act as non-radiative recombination centers, and hence emission from the QWs in their vicinity is reduced [139]. This causes the appearance of dark spots in the CL images (Figure 7.12 a)), allowing the number and position of individual dislocations to be recorded for each microdisk examined. It

should be noted there may be other causes of dark spots in CL imaging, such as dirt and InGaN composition fluctuations in QD samples. Careful sample preparation, consistent imaging conditions and plasma cleaning of samples reduces the incidence of misidentification of dislocations, although may not eliminate it completely. The presence of dislocations also leads to deformations referred to as "whiskers" which decorate the underside of the cavity [2] as can be seen in Figure 7.12 b). The whiskers arise from the PEC etch technique which is employed to undercut the cavity membrane. The threading dislocations act as charge trapping sites which inhibit photogenerated electron-hole pair separation and subsequent removal of the sacrificial region around the defect [83]. The number of whiskers and dark spots in CL have been counted for a range of disks to assess the strength of correlation between presence of a dislocation and formation of a whisker. The relationship appears linear, giving a best fit with gradient of 0.94 and an R^2 of 0.53 (Figure 2d).

The Q value for each mode was determined by calculating $\lambda_{cav}/\Delta\lambda_{cav}$, where λ_{cav} is the cavity mode wavelength and $\Delta\lambda_{cav}$ is the full width at half maximum (FWHM) of the resonance. We define the Q of a microdisk to be the maximum Q obtained from any mode. The CL spectra confirmed the frequency of the WGMs, however the measured quality factors were systematically lower than corresponding PL results. Such a discrepancy is expected, due to both the carbon contamination deposited on the sample surface from the electron beam, and the increased spectral jitter due to the changing electronic environment in the disk as the beam position is rastered across the surface. Therefore, the Q values reported in this work were obtained using PL.

As expected, Finite-difference time-domain (FDTD) simulations of a 1.2 μm GaN microdisk cavity suggest that the highest Q modes, the WGMs, are confined to the periphery of the disk membrane (Figure 7.13a)). To confirm that this modal pattern

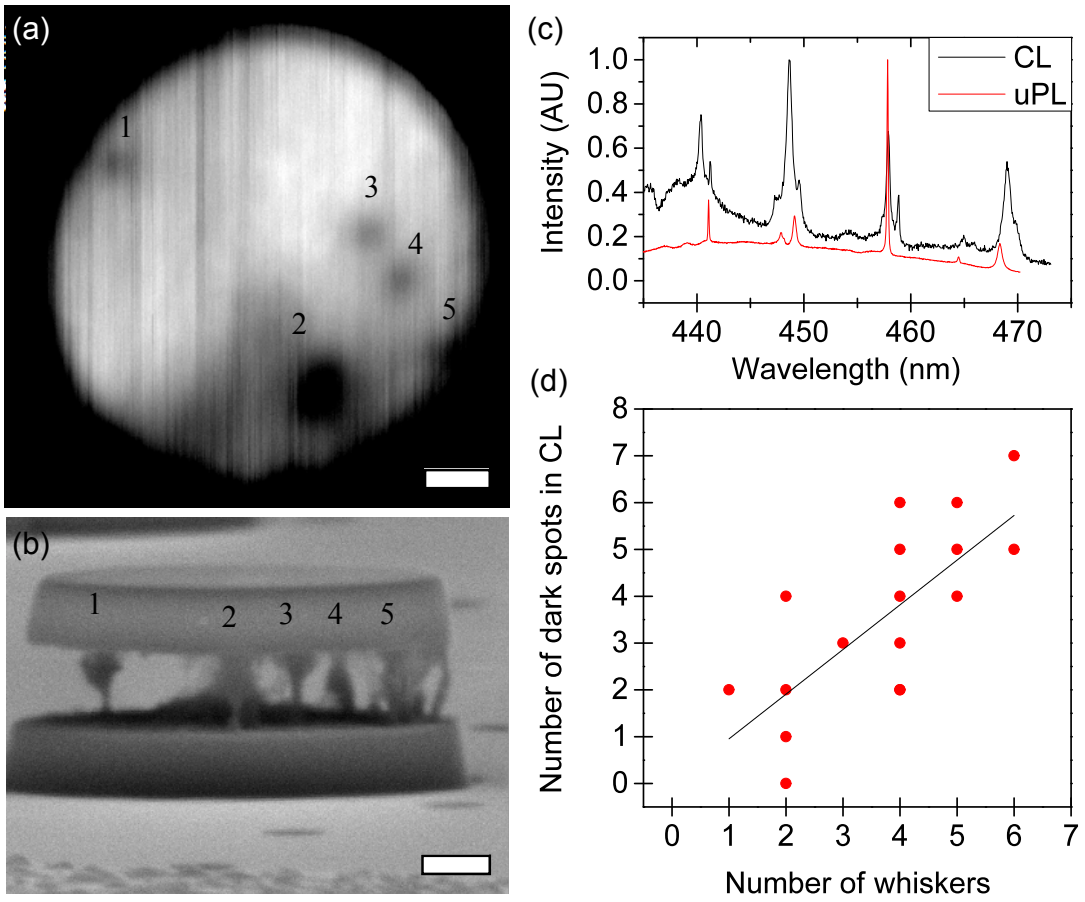

FIGURE 7.12: a) Example plan-view CL and b) Corresponding side-view SEM images of a highly undercut microdisk. Dark spots in CL are attributed to dislocations, and have had their positions marked. The central pillar is visible behind dislocation 2. Note that dislocation size can vary significantly. Scale bar represents 200 nm. c) Overlayed μ-PL and CL spectra obtained from the same microdisk at room temperature showing WGM peaks. d) The relationship between number of dark spots counted in CL and number of whiskers counted in SEM for 18 samples (several data points are superimposed). This has been fitted to $y = m \cdot x$, giving a value of m = 0.94, with $R^2 = 0.53$.

exists in the fabricated cavities, CL emission spectra were taken at each beam position during SEM imaging of a disk. The hyperspectral image created contains the emission spectra of the disk for each position of e-beam excitation, hence allowing comparison of the spectra caused by excitation in the periphery of the disk relative to those excited at the center (Figure 7.13b), c)). Images suggest that first-order WGMs are located at positions greater than 0.4 μm from the center of the disk, consistent with the results of the model. We define this part of the disk as the "outer region" and contrast it with the inner region (material less than 0.4 μm from the center of the disk) in the analysis

below.

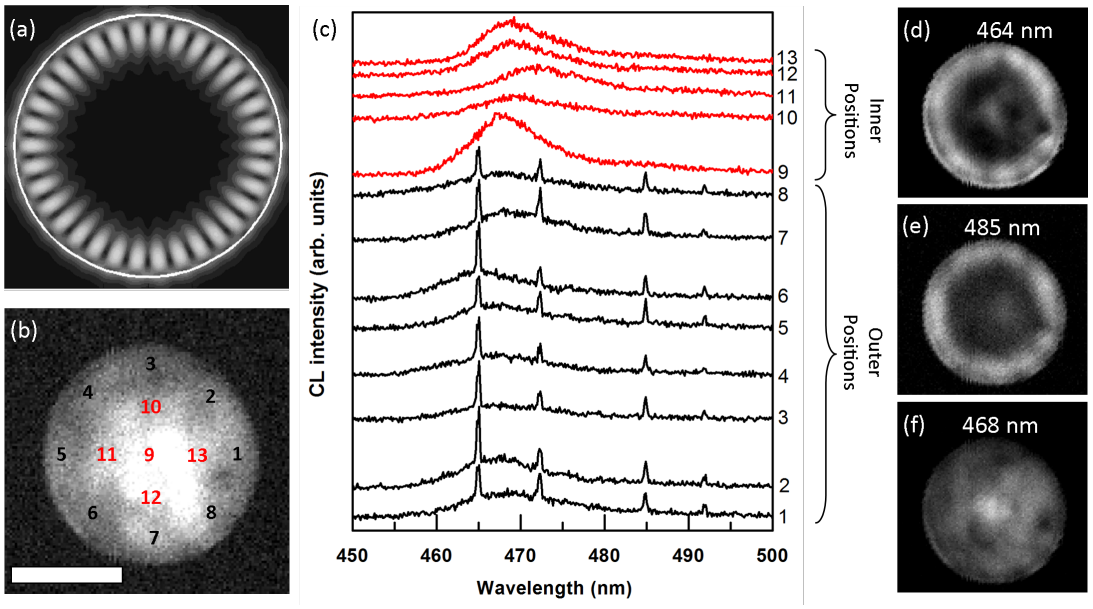

FIGURE 7.13: a) FDTD simulation of a first order WGM in a 1.2 μm diameter GaN microdisk, showing high intensity in the outer 200 nm of the cavity. b) Pan-chromatic intensity map of an imaged QW disk taken with the Attolight CL system operating with 3 kV at 15 K. Scale bar represents 500 nm. Several positions have been marked, with c) corresponding CL spectra in which we can see WGM peaks in all positions at the periphery of the disk, but only background emission when imaging the center of the disk. Example mono-chromatic CL images taken at WGM wavelengths, d) 464 nm and e) 485 nm, show greatest optical intensity when scanning in the WGM volume, validating the FDTD shown in a). By comparison an image taken at a typical background wavelength f), 468 nm, shows near uniform emission across the disk.

Using the CL-imaging technique described previously in Figure 7.12 a), the position of threading dislocations in individual disks was recorded for 35 disks (13 disks with QW active regions and 22 disks with QD active regions). Disks grown on lower defect material exhibit higher Qs. Those grown on high dislocation density material (5.3×10^9 cm^{-2}) have too low a quality to observe WGMs.

The difference between the Q-factors of disks containing QW and those containing QDs is statistically insignificant (t-test value $p = 0.44$) if made from samples of the same dislocation density. Figure 7.14 is a plot of the microdisk Q against the number of threading dislocations in specific regions of the disk. We can see that there is an anti-correlation observed between Q-factor and dislocation density when considering either

the whole disk (Figure 7.14 a)) or just the outer region (Figure 7.14 c)). The correlation is stronger for TDs located in the outer region alone, although it should be noted that the size of etching residues caused by TDs (discussed later) is variable so that TDs which cause dark spots within the center region may still affect the outer modal region of the disk, smearing out this trend. There is no correlation of Q-factor with the dislocations located only in the inner region (Figure 7.14 b)). These correlations suggest that the dislocations, especially those located in the WGM region, play an important role in limiting quality factors. Thus, we believe that the dislocations play a more influential role on Q than the composition of the active layer itself, whether QW, fractured QW or QD.

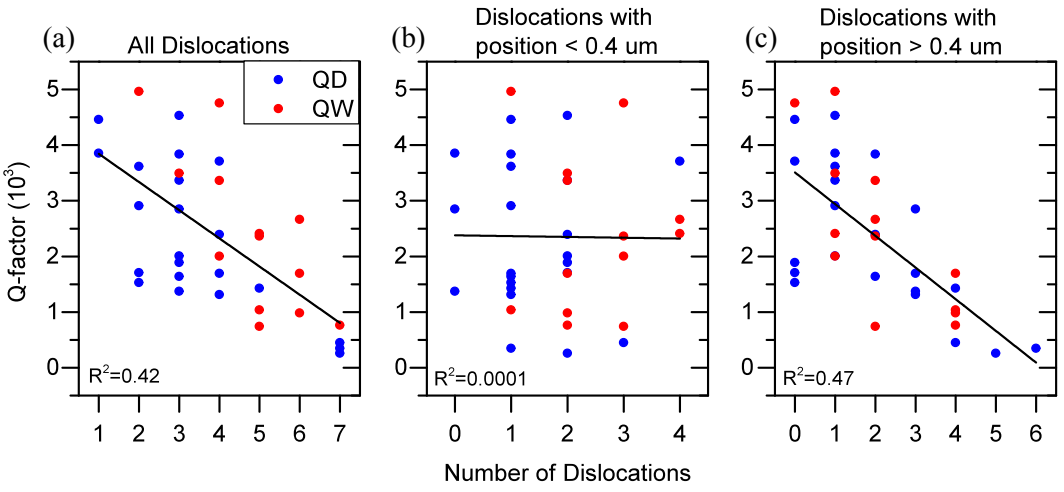

FIGURE 7.14: Graphs of microdisk Q vs. number of threading dislocations with radial position a) 0 - 0.6 μm, b) < 0.4 μm, and c) > 0.4 μm.

The spatial resolution of CL, leading to the data displayed in Figure 7.14, allows us to focus our experiments and simulations on the regions of the microdisks where Q demonstrates the greatest sensitivity to dislocations. As stated earlier, the value of Q used in the plots of Figure 7.14 are the maximum Q of the disk, for any mode. Since the highest Qs pertain to the WGMs at the periphery of the disk, it is not surprising

that the maximum Q is insensitive to dislocation in the center of the disk, (r < 0.4 μm), where there is little overlap between the dislocation and the mode.

We investigate the mechanisms by which the presence of threading dislocations could negatively influence the microdisk Q. We first consider the existence of whiskers caused by the presence of dislocations. FDTD simulations of a microdisk cavity with a pyramidal whisker with a range of sizes (height of 150 nm, base widths of 100 nm, 150 nm and 200 nm) located on the underside of the cavity membrane have been performed, in which the position of the whisker has been varied, from the center towards the edge of the disk. The simulation results suggest that the whisker creates a radiative pathway for light escape and shows that the Q factor of a first-order WGM decreases as the whisker approaches the edge of the microdisk cavity where the mode is confined. Furthermore, the azimuthal position of the pyramid affects the degree to which the Q decreases. The Q value decreases more if the whisker is centered at the WGM anti-node (i.e. high optical intensity) as opposed to on the node. Larger whiskers cause a larger effect. Figure 7.15 summarizes the results of the FDTD simulations. Such simulations corroborate our experimental observations that defects located in the high-field regions at the edge of the disk can be responsible for lowering the Q. Furthermore the magnitude of the Q-factor decrease we observe experimentally can be explained by the formation of even small whiskers, if located in the WGM volume.

It is also possible for TDs to increase the impurity level, both into the dislocation cores and into regions affected by the strain fields around the dislocation. Hence have an increased absorption coefficient relative to bulk GaN. Whilef the strain fields associated with TDs can extend over a >10 nm scale, significant increases in doping occur over a scale of a few nm [140]. Using FDTD simulation in which dislocations are modelled as approximately 4 nm in radius with extinction coefficients up to $\kappa = 50$, showed no

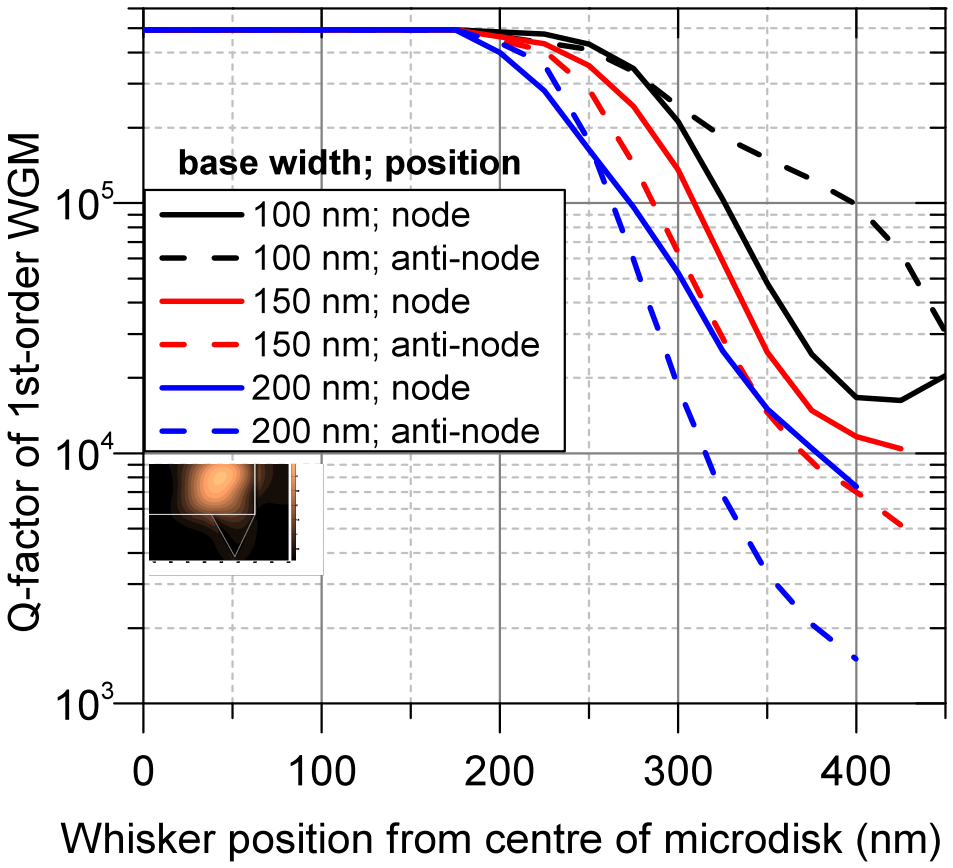

FIGURE 7.15: Q vs radial position of a pyramidal defect for 3 sizes of whisker (with a height of 150nm and base widths of 100 nm, 150 nm, and 200 nm). Each size has a plot value for azimuthal position corresponding to a node and another for positioning on an anti-node. (inset) side view of the field profile for a pyramid located at the edge of the disk (r=375 nm) centered on the antinode of a 1st order WGM. Light leaks into the whisker region and is subsequently radiated, lowering the Q.

significant effect on device Q. Such a coefficient is several orders of magnitude greater than values expected from highly doped GaN [141]. As such, we conclude that the small size of the dislocation removes any significant effect its optical absorption may have on the cavity Q.

It should be noted that TDs cause other effects, such as causing a shift in the absorption edge of bulk material through strain, having their own energy levels associated with defect and vacancy states at the TD core, and acting as non-radiative recombination centers [81, 142]. However, the magnitude of the shift in optical absorption spectra relative to the bulk is largely insignificant [143] and the energy levels associated with TD

cores is outside of the wavelength range used in these cavities [144, 145]. The whiskers formed during PEC etching confirm the role of TDs as carrier traps, thus non-radiative recombination centers. Therefore while they do directly affect internal quantum efficiency, they do not lead to a loss of photons and hence do not affect cavity quality factor. Our conclusion is that the limitations to Q posed by the TDs is through the whiskers formed during PEC etching, rather than any inherent property of the TDs themselves.

While we observe an anti-correlation between Q-factor and dislocation counts in the modal volume, we also see an upper limit of Q-factors for these cavities. Subsequent Q-measurements on dislocation-free cavities grown on samples with substrates fabricated using epitaxial lateral overgrowth give a Q-factor of 4800 ±600, supporting this limit. For future application to cQED, such as strong coupling, the causes of this limit must be understood. The quality factor of a cavity may be described as:

$$Q_{-1} = Q_{ia}^{-1} + Q_{r}^{-1} + Q_{scat}^{-1} \tag{7.7}$$

Where Q_{ia} denotes internal absorption losses, Q_r denotes intrinsic radiative losses and Q_{scat} denotes surface scattering losses.

Intrinsic radiative losses are determined by cavity design, decreasing with increasing disk radius [146]. In this regard, it is important to note that the highest value of Q is not necessarily the ultimate goal of the cavity design. The quality factor of the cavity should serve to facilitate the ultimate device application. For example, low-threshold laser designs typically use smaller cavities to increase the spontaneous emission factor and will therefore have greater intrinsic radiative loss [12]. While Q_r can be easily increased by changes in cavity design, this would be counterproductive to the intended

purpose of the cavity and would not affect the total quality factor as it is orders of magnitude larger than the other values. The value of Q_r can be approximated, as given in Eq. 7.8 [147, 148].

$$\begin{aligned} Q_r &\simeq e^{2M \cdot J} \\ J &= tanh[(1 - n_{eff}^{-2})^{1/2}] - (1 - n_{eff}^{-2})^{1/2} \end{aligned} \tag{7.8}$$

Where M is the azimuthal mode number and n_{eff} is the refractive index. For our microdisks emitting at the observed wavelengths, this gives a value of Qr of $\sim 3{\times}10^6$. FDTD simulations of such cavities with low absorption constants give a value of Q of $8{\times}10^5$ (Figure 7.16). The difference between these calculated and simulated results is explained by the simulation, including loss from horizontal surfaces and meshing errors.

Surface scattering depends on both disk morphology and surface roughness developed during fabrication. In turn, these depend not only on etching conditions but also on the quality of the etch mask used. AFM measurements of sidewall roughnesses in similar cavities have given values of approximately 2 nm [149]. ICP etching is capable of creating < 2 nm surfaces [150], should the mask be adequately smooth. Our cavities were produced using silica masks with < 0.2 nm surface roughness and as such, we believe that our cavities should be similarly smooth. Although AFM measurements of the sidewalls have not been performed. It should also be noted that samples previously produced by our group using the same methods have shown a measurable increase in sidewall roughness identifiable in a SEM, with no negative effect on cavity Q. As such we believe that the roughness is low enough not to limit cavity Q-factors. FDTD simulations were performed with a range of edge-wall roughnesses, with sidewall geometries modeled on those typically observed in fabricated devices as taken from SEM images.

The correlation length in the radial and vertical dimensions is 30 nm and 300 nm, respectively. The relation of edge roughness to simulated Q_{scat} is given in Figure 7.16, in which no absorption effects were included in the simulation and the top horizontal surfaces of the disk were assumed to be smooth.

Q_{abs} can be approximated as $Q_{abs} = 2\pi n_{eff}\alpha\lambda$, where α is the attenuation coefficient, n_{eff} is the effective refractive index of the medium, and λ is the wavelength of the mode considered [151]. Internal absorption can be significant in the nitrides for emission below the band-edge of GaN, due to moderate unintentional doping. This leads to increased electronic transitions between donor-acceptor levels and structural defects [141]. For the wavelength of modes observed 460 nm ± 14 nm, absorption coefficients have been stated in the range of 30 - 350 cm^{-1} [22, 23, 141, 152] depending on growth conditions, dopant levels and the substrate used, leading to approximate Q_{abs} values between 10^3 and 10^4. Such a wide range may be explained by the variation in dopants and structural defects between the samples in these studies, leading to a wide variety of absorption in both the Urbach tail and free carrier absorption regions [152]. It is also possible, given the modes' locations at the edge of the cavity, that there is a small contribution to the absorption coefficient from surface-state absorption. As such, the extinction coefficient used here represents an effective value which includes this component.

It should be noted for comparison that similar structures in other materials systems have achieved significantly higher Q-factors($\sim 5 \times 10^5$ and $\sim 10^5$ for silicon and GaAs [153, 154]), where the absorption coefficients are $\sim 10^{-4}$ and 1 cm^{-1}, respectively [155, 156]. Q factors in these devices are limited by intrinsic radiative and scattering losses, rather than absorption losses.

To further consider the limitations from internal absorption, the cavity structures were simulated with a range of absorption coefficients.

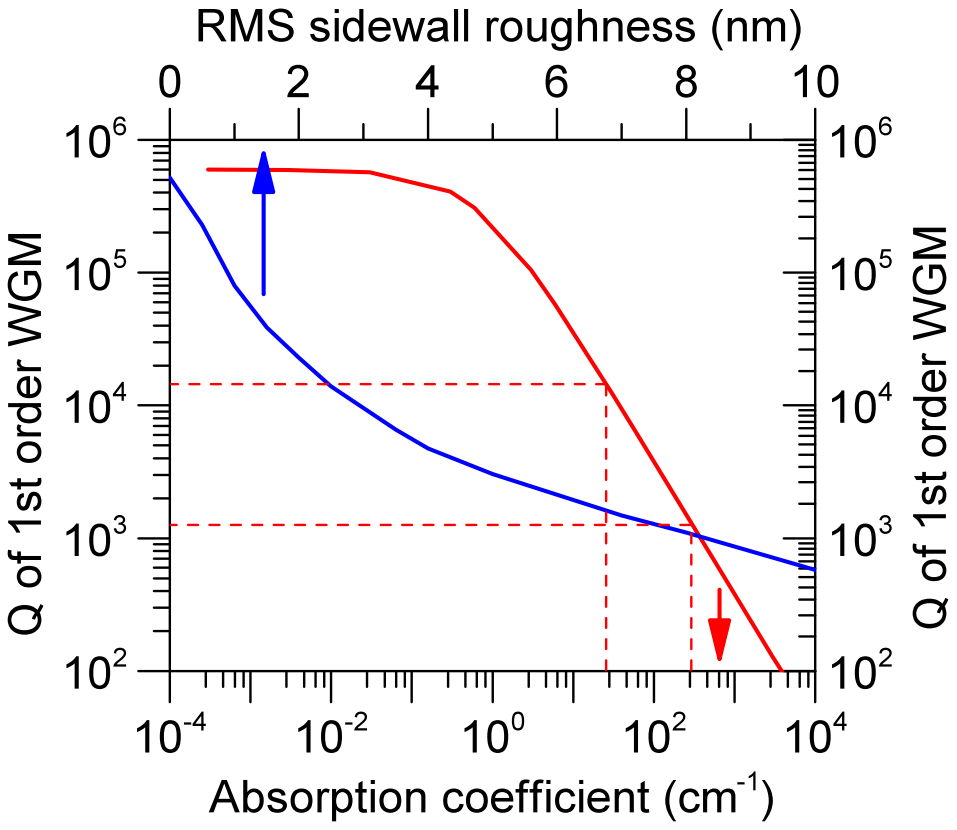

FIGURE 7.16: (Black trace) Simulated Q vs RMS roughness at the periphery of a 1 μm GaN microdisk. (Red trace) Q vs absorption coefficient, in which the disks are modeled as having no surface roughness. (Dashed line) outer limits of absorption coefficients for GaN from literature and corresponding cavity Q factors [22, 23].

We see in Figure 7.16 not only the relationship between the absorption coefficient and cavity Q, but also the point at which the internal absorption of the cavity becomes insignificant. For coefficients less than 1 cm^{-1}, the intrinsic radiative loss of the cavity dominates the absorption loss and hence sets the limit of Q for cavities of these dimensions at $\sim 10^6$. Using previously stated values for the absorption coefficient of MOCVD grown GaN give the simulated Q_{abs} between 10^3 and 10^4, in agreement with calculated values. Therefore, we can use the simulations and measurements of Q to examine the limitations of the nitride cavities and the limitations of the nitride material system itself.

While scattering losses may be reduced by refinement of the plasma etching technique, the absorption losses pose a more difficult challenge to increasing nitride cavity Q-factor. Slight reduction of the free carrier absorption may be achievable by alteration of material growth conditions, although the sub-bandgap absorption in the wavelength range used for this study is significant at all achievable dopant levels [141]. It may therefore be more tractable to alter the wavelength of emission from the InGaN active layers to a lower energy, where the GaN absorption would be reduced. This decrease in absorption would, however, be small over the range of achievable wavelengths of the active layer, determined by the maximum indium percentage possible for growth of QD and QWs.

To conclude, we have shown that we are able to identify the position of individual TDs in microcavities using CL. Using this method to map dislocation position across microdisks with a range of active layers, we observed an anti-correlation of the number of dislocations in a specific cavity with the cavity Q-factor. Simulations and SEM-CL spectra confirm that, as expected, the whispering gallery modes exist in the periphery of the microdisk cavities, and it is the dislocations in this region specifically which affect cavity Q. We suggest that the presence of TDs do not inherently cause a significant reduction in the Q factor of the microcavities, but that they do cause the formation of unetched material during PEC etching which subsequently causes optical leakage from the cavity. This loss may be avoided by alternative fabrication methods. The limitations of the GaN system have been investigated, and internal absorption has been shown to be the significant factor in limiting cavity Q. Overall, our investigations here demonstrate the utility of a powerful new approach to the characterization of semiconductor microdevices, whereby rather than examining the general characteristics of the material from which the devices are made, we assess the specific micro and/or nanostructure of individual devices

and compare this information to the device properties. This approach has allowed us to directly link micro-structural features (in this case whiskers relating to dislocations) to specific changes in performance, providing new and powerful insights, which a more global methodology could not achieve. Other semiconductor micro- and nano-devices, particularly in complex or highly defected materials systems, could profitably be assessed in the same manner.

The next section discusses tapered fiber experiments which have the potential to conclusively test our hypothesis that absorption is limiting the Q of GaN-based devices.

7.5 Tapered fiber measurements on GaN microdisks

The following authors contributed to the work conducted in this section: Alexander Woolf, Xingyu Zhang, Aun Zaidi, Phillip Frick, Jon Snyder, Andrew Magyar, Katherine Pooley, Christine Zgrabik, Tongtong Zhu, Rachel A. Oliver and Evelyn Hu. Alex, Xingyu, Aun, Phillip, Jon, Andrew, Katherine, and Christine all worked to optimize the fiber pulling conditions as well as coupling setup. Tongtong grew the material wafers and Alex processed the devices. Alex, Xingyu, and Aun collected and analyzed the data.

As discussed in Section 7.4, the quality factors (Q-factors) of GaN based microcavities remains low when compared to similar devices fabricated from the arsenide or phosphide material systems. While the current working hypothesis is that the Q is limited by material absorption and not the cavity roughness, experiments are necessary to confirm this. A tapered fiber measurement, while arduous offers the potential to deconvolve the effects of material absorption from cavity roughness. In traditional PL measurements the signal from the microcavity device is only collected at wavelengths where the gain material luminesces. However, these are the same wavelengths where

material absorption is present, therefore the lifetime of the observed modes in PL is reduced by both material absorption and the cavity geometry/roughness. In a tapered fiber measurement, light of any desired wavelength is guided through an optical fiber which is placed in close proximity to a microcavity device. The transmission of the fiber is observed and the wavelengths of light that are resonant with the microcavity modes will couple to the device. As the device is inherently lossy, this leads to dips in the transmission through the optical fiber, as not all the light at the resonant wavelengths gets coupled back into the optical fiber. Figure 7.19 shows a schematic of the coupling between the optical fiber and micro cavity (in this case a microsphere) as well as the corresponding dips in transmission, from [24].

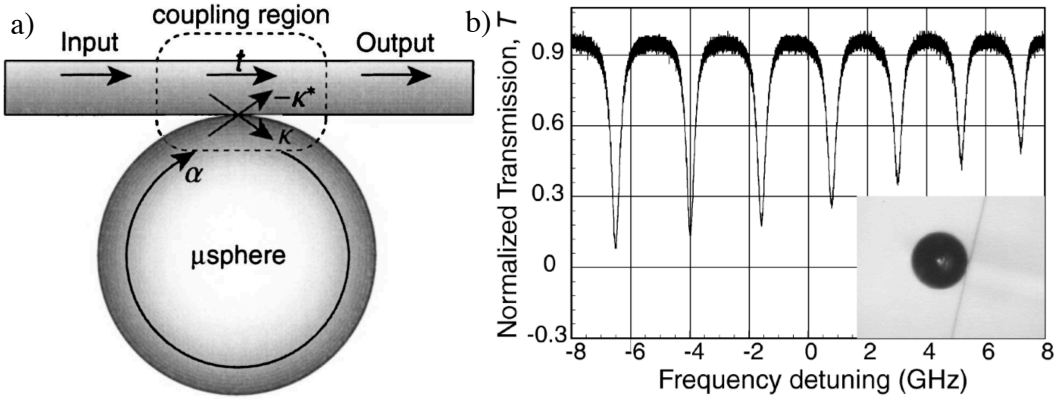

FIGURE 7.17: a) schematic of a tapered fiber near an optical microcavity. If the two are in close proximity then light at wavelengths corresponding to cavity resonances will couple to the microcavity device and appear as dips in the transmitted signal. b) example measurement showing the dips in transmission through the fiber due to coupling, from [24]

Similar to PL experiments one can fit the resonances of the transmission dips in order to calculate a cavity Q. Since the measurement is passive compared to PL, where a tremendous amount of carriers are excited in order to achieve appreciable luminescence, the Q obtained using tapered fiber is often referred to as a "cold-Q". For our GaN microcavities the comparison between the PL Q and the cold-Q at longer wavelengths will allow us to identify if material absorption plays an significant role towards limiting

the PL Q. If the cold-Q is appreciable higher at telecom wavelengths compared the Q at visible wavelengths observed in PL, then it suggests that material absorption is responsible for a majority of the photon loss within the device. If cold-Q and PL Q are similar then it suggests that the cavity design and or roughness is non-ideal and therefore the major cause of photon loss. As a note there are a few caveats which must be addressed. The effect of surface roughness is reduced as the wavelength of light is increased, therefore the PL Q at wavelengths near 450 nm is inherently more sensitive to cavity roughness than at infrared ($\sim$1360 nm) wavelengths. However, this effect can be accounted for with simulations or by working at wavelengths just past the absorption wavelengths of the material in order to reduce the effect.

To summarize, the goal of this experiment is to compare the Q of a GaN-based microcavity in measured in PL to that of the cold-Q measured using tapered fiber. Furthermore, one could envision experiments where the PL and tapered fiber setups are incorporated into one, and the cold-Q is measured as a function of the excitation laser pump power. This could offer additional information in regards to heating and non-radiative recombination effects which are currently not quantified for our devices.

While this technique can provide a great deal of insight into the properties of the microcavity device there are a multitude of challenges which must be overcome in order to realize a successful measurement. First, the fiber must be adiabatically tapered down to thickness on the order of the wavelengths which will be transmitted through it. This is necessarily in order to allow the transmitted light to evanescently leak from the fiber into the microcavity device. Figure 7.20 is a schematic from [25] of a tapered fiber, the coupling between the fiber and the device must take place in the waist region.

There are a variety of different methods utilized to taper fibers, including laser

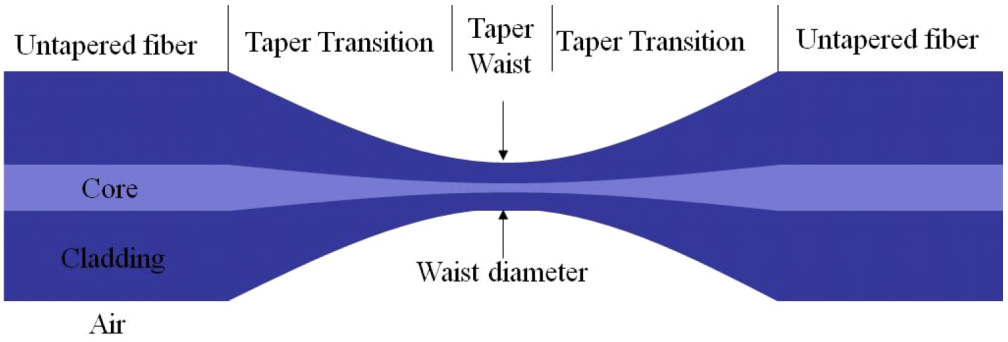

FIGURE 7.18: Schematic of a fiber after tapering. The small diameter of the waist allow light to evanescently leak from the fiber and couple into into a microcavity device, from [25]

heating [157, 158], chemical etching [159], and flame heating [160] which is used in this work. In brief, the flame heating technique works by heating the fiber with a flame while simultaneously pulling the fiber with mechanical motors. The transmission through the fiber is also monitored during this process in order to ensure that the fiber reaches the single mode condition and maintains a high level of light transmission after thinning. High transmission is indicative of an adiabatically tapered fiber and is necessary in order to realize coupling to a microcavity device. Once the ideal temperature and pulling conditions for the fiber are identified, a fiber can be tapered with transmission values as high as to 99% of the pre-pull transmission in a matter of minutes. Figure 7.19 shows a schematic of the tapered fiber setup implemented in this work, courtesy of Phillip Frick. A detailed description of the experimental setup as well as pulling conditions will be published elsewhere.

Another challenge related to the tapered fiber technique is that the fiber must only come into close proximity with the microcavity device. If the fiber touches the substrate, the light will leak from the fiber and no dips will be apparent in the transmission. This is overcome by using a piezo controlled stage and goniometer. When the fiber is correctly aligned if visible light is transmitted through the fiber one can see the microcavity device light up and dips will be present in the measured spectra.

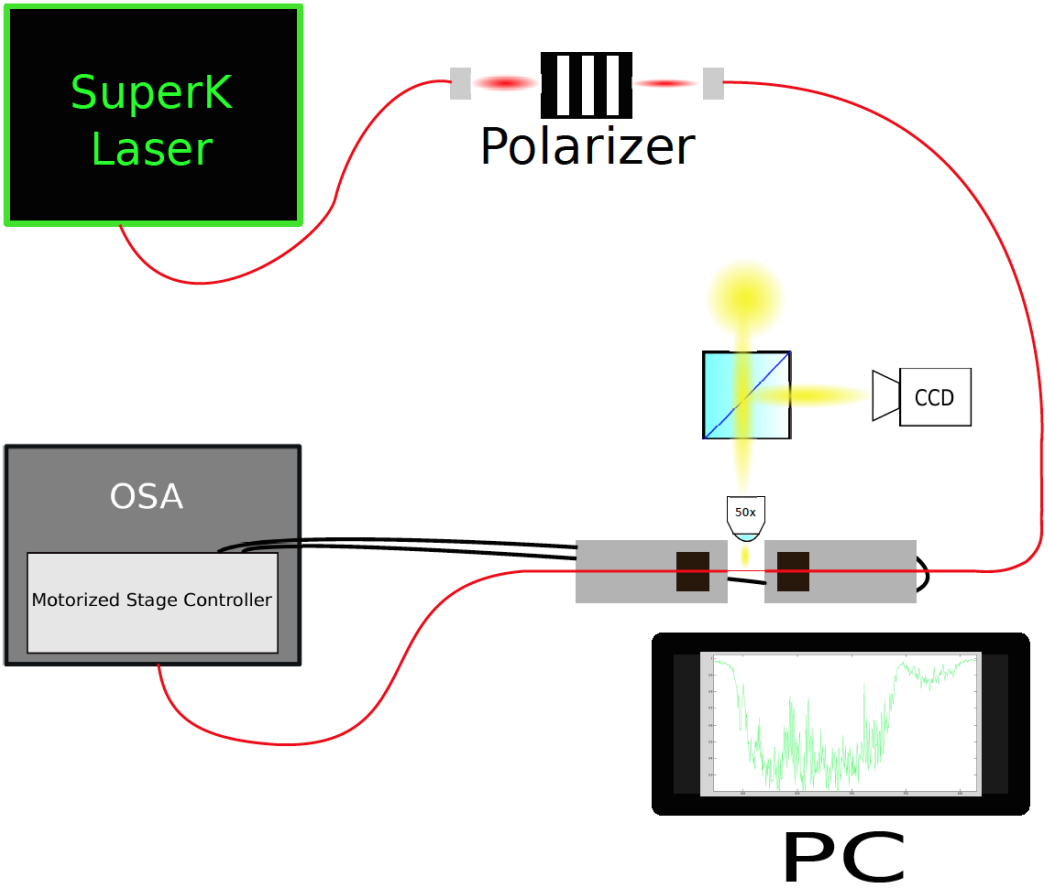

FIGURE 7.19: Schematic (courtesy of Phillip Frick) of the essential components of the tapered fiber setup used in this work. The optical fiber is denoted in red and the transmission is monitored using an Optical Spectrum Analyzer (OSA).

We will now present preliminary data obtained from a 3μm GaN microdisk cavity. The cavity contains three layers of InGaN QDs and are identical to those shown in Figure 6.3. PL measurements give Q values as high as 9100 as shown in Figure 6.4 f). As the tapered fiber is brought into proximity with the microdisk cavity, dips are clearly apparent in the transmitted signal which can be seen in Figure 7.20, for clarity one such dip is labeled "Cavity Mode." This is to our knowledge the first demonstration of tapered fiber measurements from GaN based microcavities.

Unfortunately, the linewidth of the mode is resolution limited to a value of $Q_{measured} = 3300$, therefore at this point we can only identify a lower bound for the cold-Q of these devices. Before doing so however, there is an adjustment factor which accounts for the

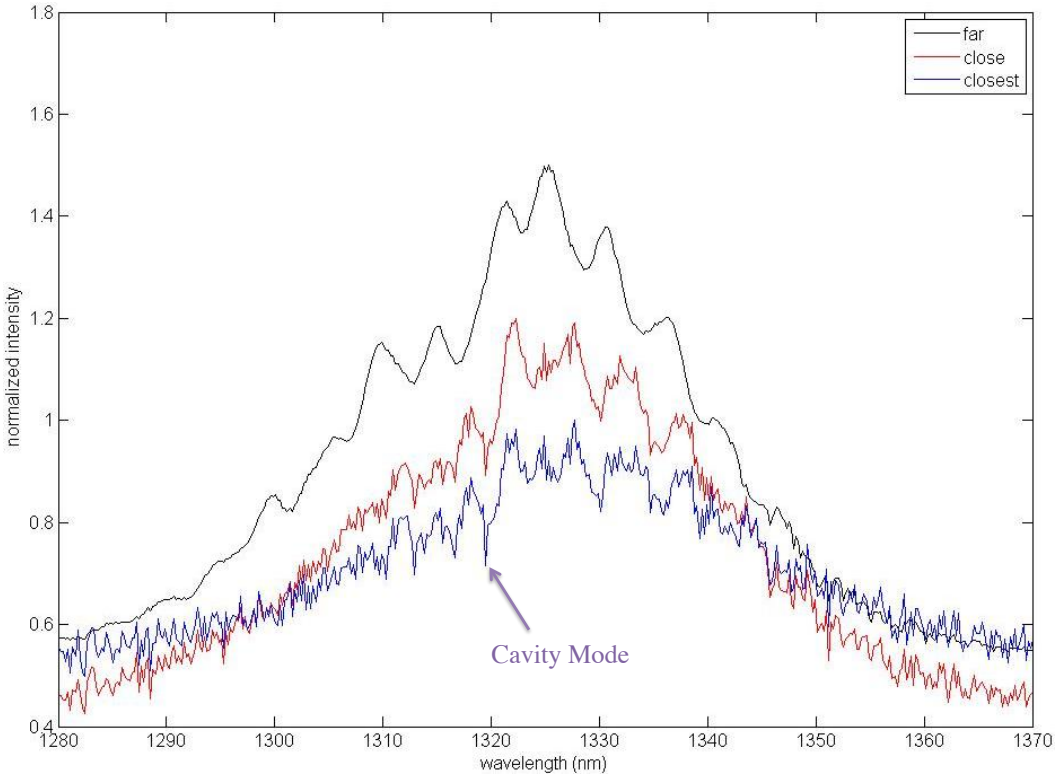

FIGURE 7.20: Transmission measurement of the tapered fiber at various distances from the microcavity device. As the fiber gets in close proximity to the microdisk, dips in the transmission are clearly apparent which is indicative of coupling to microdisk WGM modes. One such dip is labeled for clarity.

fact that our fiber-cavity system is not optimally or critically coupled, which can be seen from the fact that the transmission dips do not go down to a value of 0%. Details related to this adjustment factor are given in reference [161], we therefore use Eq. 7.9 to convert the Q of the measured transmission dips to the "real Q" of the device.

$$Q_{real} = \frac{2Q_{Measured}}{1 \pm \sqrt{1 - |\delta T|}} \tag{7.9}$$

Entering the values for our collected data of $\delta T = 0.1$, and $Q_{measured} = 3300$ we have a maximum cold-Q value as high as $Q = 64306$. As the data is currently resolution limited, I will refrain from making comments with regards to the implications of this measurement and instead request the reader to view this as a proof of principle. Future experiments should seek to repeat this measurement with a higher resolution OSA and

work is already underway in the Hu lab to do so.

Chapter 8

Conclusion

8.1 Summary

Part I outlined the key advantages and challenges regarding InGaN QDs as a gain medium within photonic microcavities. The high optical efficiency and exciton-binding energy of InGaN QDs make them ideal candidates as light emitters within photonic devices. Furthermore, emission at visible wavelengths allows for their use as coherent light sources in practical applications such as lighting and on-chip photonic integrated circuits. We also discussed the accompanying challenges related to InGaN QDs that include the presence of internal fields in the c-plane, the lack of a selective room temperature wet etch, threading dislocations and the absence of a controlled and reproducible QD growth mechanism. Part I concluded with previous work on GaN microdisk cavities with embedded InGaN QDs, whose limitations served as a driving motivation at the onset of this thesis.

Part II discussed the principles of laser operation, including the derivation of the laser rate equations. Analysis of the rate equations suggests that InGaN QDs embedded

within high spontaneous emission factor optical cavities theoretically yields lasers with low-thresholds. The principles of microdisk and photonic crystal cavity operation show that these two systems serve as promising cavity designs for low-threshold lasers. Finally, the enhanced carrier localization within QDs theoretically suggests that they have higher gain than bulk or QW emitters. Previous work in the arsenide and phosphide systems confirm that QDs within microcavities are the lowest lasing threshold semiconductor devices to date.

Part III discussed experimental results on InGaN QDs and FQWs within microcavities. Initial experiments on 3 μm diameter microdisk cavities demonstrated the highest quality factor GaN-based microcavites to date ($Q \sim 9100$). However, the 3 μm devices did not exhibit laser oscillation and 1 μm diameter were fabricated because of their higher spontaneous emission factors. The 1 μm diameter microdisks with three layers of embedded InGaN QDs served as the first demonstration of InGaN QD lasing within a microcavity. Subsequent experiments were conducted to deconvolve the emission of the QD from the FQW and a distinctive lasing signature of QDs, in the form of a blue-detuned lasing peak, was identified. This work conclusively demonstrated that the QDs not the FQWs facilitate lasing within the microdisk device. Part III continued with further experiments on Gan-based microcavities. This serves as a critical step towards the realization of next generation photonic devices. Photonic crystal nanobeam cavities with embedded FQW exhibited more than an order of magnitude lower lasing thresholds than similar fabricated QW devices. We ascribed the enhanced performance to the enhanced spatial localization of the photo-induced carriers, as compared to QWs, in addition to the large capture cross section of the FQW active layer compared to QDs.

Cavity QED experiments on InGaN QDs within GaN photonic crystal cavities were performed. These experiments attempted to demonstrate the first evidence of weak or

strong coupling within a nitride-based device, a critical step towards quantum computation and polariton lasing. No evidence of weak or strong coupling was observed, which then served as the motivating principle for cathodoluminesence and tapered fiber experiments. These experiments suggested that material absorption within the microcavity devices is responsible for the relatively lower Q, compared to similar arsenide or phosphide-based devices.

8.2 Future directions

For better or worse this thesis has raised more questions than it has answered. While the Q is only a figure of merit and device performance should be the ultimate objective, the low quality factor of GaN based microcavity devices must be addressed in order to realize further advances of the material system. It is currently unclear if the predominant photon absorption mechanism originates in the bulk or at the surface of the microcavity device. It seems most likely that the cause is the surface and it may be possible to eliminate the unwanted absorption by altering the dry etching process. The lack of any observed weak or strong coupling between the InGaN QD is also puzzling and future work should attempt to identify the position of the QD within the cavity to ensure that poor spatial overlap is not the problem. In regards to QD lasers, it appears that the devices with QW active layers will continue to outperform those with QDs until the QD density can be increased. Alternatively, preliminary results on non-polar a-plane QDs show significantly shorter radiative lifetimes which should lead to improved device performance compared to c-plane emitters. Perhaps the efficiency of the a-plane QDs is high enough to facilitate lower lasing thresholds than similar fabricated a-plane

QW devices. Additional, FQW PCC experiments should be conducted to evaluate the morphology of the confinement potential of the FQW.

It is still an open question as to why the lasers with FQWs exhibited higher thresholds than QWs in microdisks while the opposite was true in PCCs. Perhaps the carrier confinement in the FQW compared to QWs leads to a greater immunity to the large surface area of the PCC. Finally, PCC lasers with embedded InGaN QDs should be fabricated. While we were unable to fabricate any PCCs that exhibited modes at the blue end of the emission spectrum ($\lambda = 425$ nm), as the QDs are known to lase at these wavelengths, it is possible that the QD PCC lasers may even out perform the FQW devices.

Appendix A

Gas tuning setup

Dr. Kasey Russel and Alex Woolf designed and built this setup. As discussed in Section 7.3 the purpose of the gas tuning setup is to reversibly tune the spectral resonance of the photonic microcavity. In brief, nitrogen or xenon gas is flowed into a helium-cooled cryostat. The gas condenses on the sample that rests on the cold finger and the conformal layer of solid nitrogen shifts the resonance of the optical cavity. The wavelength shift is due to the fact that the index of refraction of the solid nitrogen effectively adds material to the optical cavity. As the cavity volume is increased, this leads to a red-shift of the resonance. Therefore, gas tuning can only tune the resonance of a cavity mode to longer wavelengths. For the purpose of the thesis, the setup was necessary in order to match the wavelength of the cavity mode to the emission wavelength of the InGaN QD exciton. Figure A.1 shows a schematic of the gas tuning setup.

The setup is designed to a flow a well defined amount of gas into the chamber in controlled bursts or "shots." The setup was designed this way because for the Purcell effect experiment a lifetime measurement must be made at discrete positions of the cavity mode. Therefore the tuning must done in digital steps instead of continuously.

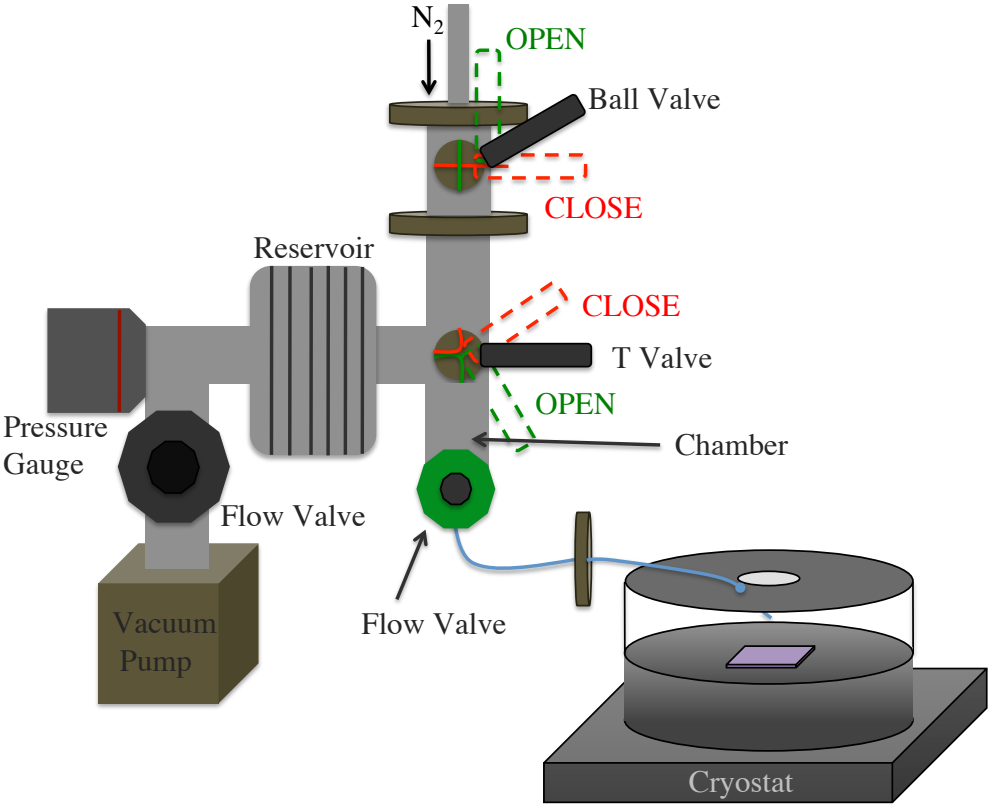

FIGURE A.1: Schematic of the gas tuning setup.

It is desirable to control the amount of tuning per burst. This necessitates control over the amount of gas injected into the cryostat per shot. The combination of the T valve, reservoir, and Flow valves allow for the control of the nitrogen pressure (and therefore number of molecules) per shot.

The procedure for tuning is as follows:

1. The cryostat evacuated and cooled to liquid helium temperatures.
2. The ball valve and green flow valve is closed.
3. Vacuum is pulled with the T-valve in both the OPEN and CLOSE positions.
4. Both flow valves are closed.
5. The T-valve is moved to CLOSE position, so chamber is isolated from the reservoir.
6. The ball valve is moved to the OPEN position and the reservoir is filled with a small amount of nitrogen from a regulated source.

7. The ball valve is moved to the CLOSE position.

8. The vacuum pump is turned on and the black flow valve is slowly opened until the desired pressure is attained ($\sim 10^{-1}$ ATM for our specific setup).

9. The black flow valve is closed.

10. The T-valve is moved to the OPEN position in order to load the chamber with one shot of nitrogen.

11. The T-valved is moved to the CLOSE position in order to isolate the chamber from the reservoir.

12. The green flow valve is opened allowing the nitrogen from the chamber to enter the cryostat.

13. The green flow valve is shut. Thus completing one shot.

14. PL or lifetime measurements are made.

For subsequent shots steps 10-14 are repeated.

Figures A.2 and A.3 show the top and bottom view of the custom made cryostat top-plate. The cryostat with top-plate and flow tubing in place is shown in Figure A.4. The components for regulating the pressure of the reservoir is shown in Figure A.6.

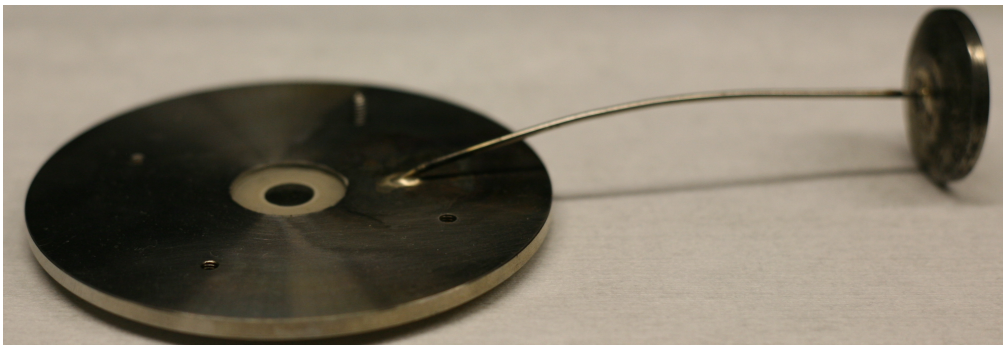

FIGURE A.2: Top view of the custom made cryostat top-plate.

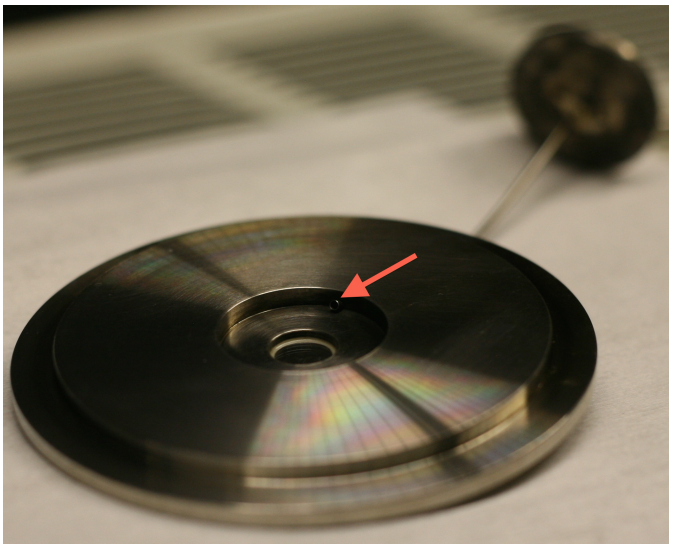

FIGURE A.3: Bottom view of the custom made cryostat top-plate. The flow tube is denoted with an arrow.

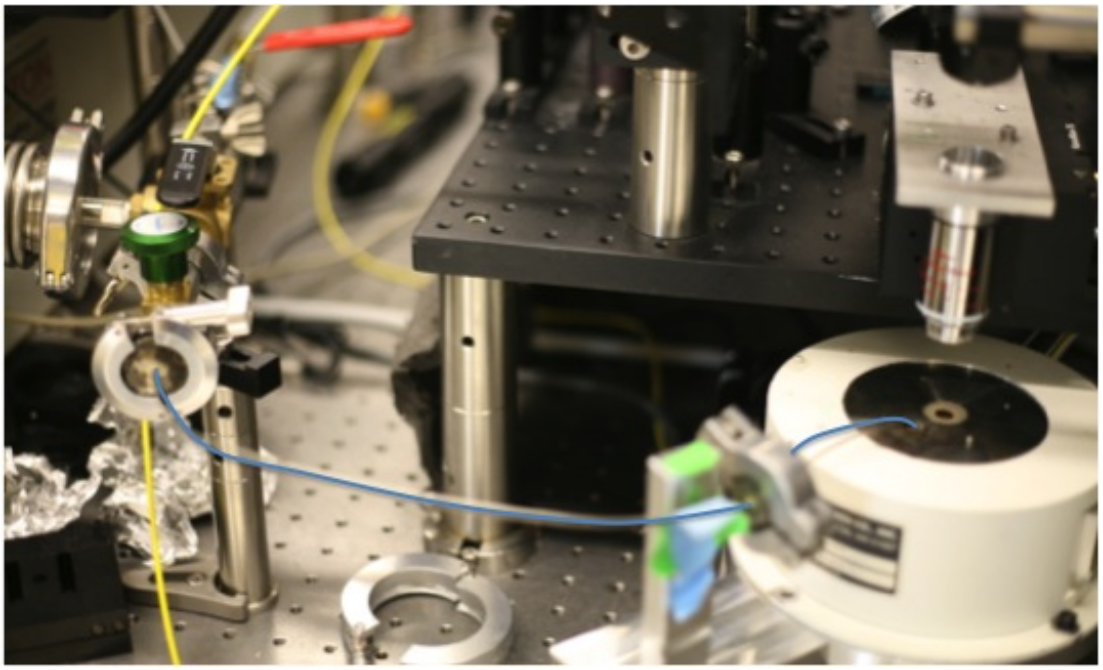

FIGURE A.4: Cryostat with custom top-plate and flow tubing in place. The flow tubing is outlined with a blue line for clarity. The pressure regulation valves are visible in the top left of the figure.

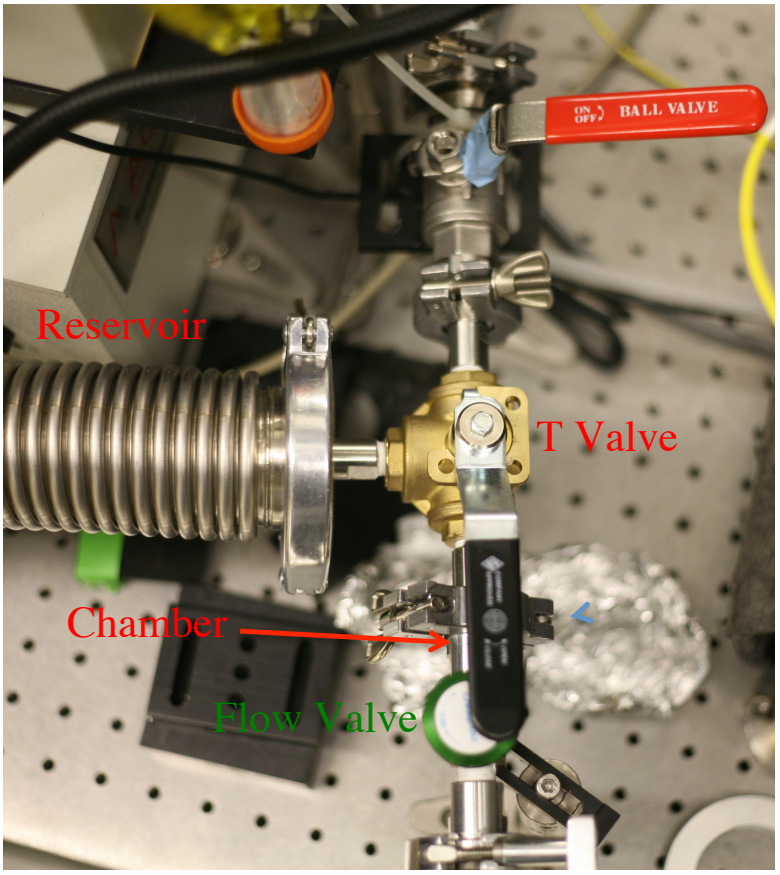

FIGURE A.5: Chamber loading and unloading mechanism.

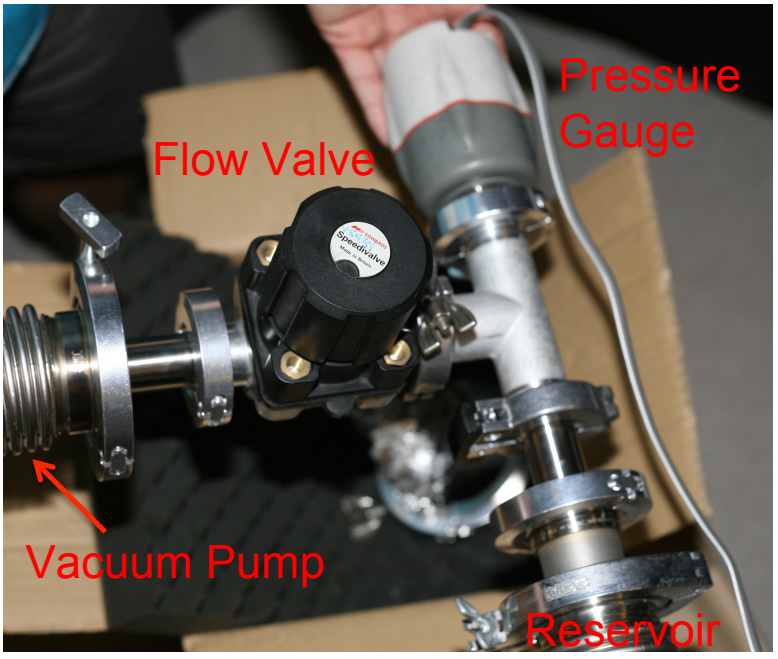

FIGURE A.6: Pressure regulation and measurement mechanism.

Bibliography

[1] Professor Xie Group UCLA. Energy Band Gap and Lattice Constant of Various Semiconductors at Room Temperature. URL `http://www.seas.ucla.edu/smrl/GaN.html`.

[2] HAR El-Ella, F Rol, and MJ Kappers. Dislocation density-dependent quality factors in InGaN quantum dot containing microdisks. *Applied Physics ...*, 2011.

[3] Masakatsu Suzuki, Takeshi Uenoyama, and Akira Yanase. First-principles calculations of effective-mass parameters of AlN and GaN. *Physical Review B*, 52(11): 8132–8139, September 1995.

[4] Antony Ingram. 2015 BMW i8 To Feature World's First Laser Headlights. *Green Car Reports*, 2013.

[5] Alexey Kavokin, Jeremy J. Baumberg, Guillaume Malpuech, and Fabrice P. Laussy. *Microcavities*. Oxford University Press, 2007. ISBN 0191620734. URL `http://books.google.com/books?hl=en&lr=&id=9Jr1uvqguEEC&pgis=1`.

[6] Haitham A.R El-ella. *III-Nitride Optical Resonators and InGaN Quantum Dots*. Dissertation, Cambridge University, 2012.

[7] Kevin Hennessy. *Photonic Crystal Nanocavities Positioned and Tuned for Cavity-QED*. Dissertation, University of California at Santa Barbara, 2006.

[8] Adele Tamboli. *Photoelectrochemical Etching of GaN for High Quality Optical Devices*. Dissertation, University of California at Santa Barbara, 2009.

[9] P Gibart. Metal organic vapour phase epitaxy of GaN and lateral overgrowth. *Reports on Progress in Physics*, 2004.

[10] N N Ledentsov. Quantum dot laser. *Semiconductor Science and Technology*, 26 (1):014001, January 2011.

[11] Adele C. Tamboli, Elaine D. Haberer, Rajat Sharma, Kwan H. Lee, Shuji Nakamura, and Evelyn L. Hu. Room-temperature continuous-wave lasing in GaN/InGaN microdisks. *Nature Photonics*, 1(1):61–64, January 2007.

[12] Mee Koy Chin, Daniel Y. Chu, and Seng-Tiong Ho. Estimation of the spontaneous emission factor for microdisk lasers via the approximation of whispering gallery modes. *Journal of Applied Physics*, 75(7):3302, April 1994.

[13] JD Joannopoulos, SG Johnson, JN Winn, and RD Meade. *Photonic crystals: molding the flow of light*. Princeton university press, 2011. URL `http://books.google.com/books?hl=en&lr=&id=owhE36qiTP8C&oi=`

fnd&pg=PP2&dq=Photonic+crystals:+molding+the+flow+of+light&ots=6YewoddRnK&sig=wEitz2np7swj08H0ojLzGgXrHJY.

[14] E Yeganegi, A Lagendijk, AP Mosk, and WL Vos. Local density of optical states in the band gap of a finite one-dimensional photonic crystal. *Physical Review B*, 2014.

[15] S Strauf, K Hennessy, and MT Rakher. Self-tuned quantum dot gain in photonic crystal lasers. *Physical review ...*, 2006.

[16] K Nozaki, S Kita, and T Baba. Room temperature continuous wave operation and controlled spontaneous emission in ultrasmall photonic crystal nanolaser. *Optics express*, 2007.

[17] MW McCutcheon and PB Deotare. High-Q transverse-electric/transverse-magnetic photonic crystal nanobeam cavities. *Applied Physics ...*, 2011.

[18] M Asada. Gain and the threshold of three-dimensional quantum-box lasers. *Quantum Electronics, IEEE ...*, 1986.

[19] B Ellis, MA Mayer, G Shambat, and T Sarmiento. Ultralow-threshold electrically pumped quantum-dot photonic-crystal nanocavity laser. *Nature ...*, 2011.

[20] K Srinivasan, M Borselli, and O Painter. Cavity Q, mode volume, and lasing threshold in small diameter AlGaAs microdisks with embedded quantum dots. *Optics ...*, 2006.

[21] M. Witzany, R. Roß bach, W.-M. Schulz, M. Jetter, P. Michler, T.-L. Liu, E. Hu, J. Wiersig, and F. Jahnke. Lasing properties of InP/(Ga_{0.51}In_{0.49})P quantum dots in microdisk cavities. *Physical Review B*, 83(20):205305, May 2011.

[22] F. Omnes, N. Marenco, B. Beaumont, Ph. de Mierry, E. Monroy, F. Calle, and E. Munoz. Metalorganic vapor-phase epitaxy-grown AlGaN materials for visible-blind ultraviolet photodetector applications. *Journal of Applied Physics*, 86(9): 5286, November 1999.

[23] S. Strite. GaN, AlN, and InN: A review. *Journal of Vacuum Science & Technology B: Microelectronics and Nanometer Structures*, 10(4):1237, July 1992.

[24] Ming Cai, Oskar Painter, and Kerry Vahala. Observation of Critical Coupling in a Fiber Taper to a Silica-Microsphere Whispering-Gallery Mode System. *Physical Review Letters*, 85(1):74–77, July 2000.

[25] Ye Tian, Wenhui Wang, Nan Wu, Xiaotian Zou, and Xingwei Wang. Tapered optical fiber sensor for label-free detection of biomolecules. *Sensors (Basel, Switzerland)*, 11(4):3780–90, January 2011.

[26] Gordon E. Moore. Cramming more components onto integrated circuits, Reprinted from Electronics, volume 38, number 8, April 19, 1965, pp.114 ff. *IEEE Solid-State Circuits Newsletter*, 20(3):33–35, September 2006.

[27] OTRC. Overall Technolog Roadmap Characteristics. Technical report, International Technologu Roadmap for Semiconductors, 2010.

[28] Pat Gelsinger. Moore's Law: We See no End in Sight. In *SYS-CON*, 2008.

[29] AEO. AEO2014 EARLY RELEASE OVERVIEW. Technical report, 2014.

[30] Jun-jie Shi and Zi-zhao Gan. Effects of piezoelectricity and spontaneous polarization on localized excitons in self-formed InGaN quantum dots. *Journal of Applied Physics*, 94(1):407, June 2003.

[31] Nicolas GRANDJEAN and Marc ILEGEMS. Visible InGaN/GaN Quantum-Dot Materials and Devices : There has been rapid progress in light emitting diodes and lasers based on nitride semiconductors, with the development of nitride quantum-dot lasers as the next challenge. *Proceedings of the IEEE*, 95(9):1853–1865.

[32] Rachel A. Oliver, G. Andrew D. Briggs, Menno J. Kappers, Colin J. Humphreys, Shazia Yasin, James H. Rice, Jonathon D Smith, and Robert A. Taylor. InGaN quantum dots grown by metalorganic vapor phase epitaxy employing a post-growth nitrogen anneal. *Applied Physics Letters*, 83(4):755, July 2003.

[33] R Johne. *Strong light matter coupling in semiconductor nanostructures - Nonlinear %effects and applications*. Dissertation, Universite Blaise Pascal, 2009.

[34] Anas F. Jarjour. *Optical Studies of Single InGaN/GaN Quantum Dots*. Dissertation, Oxford University, 2007.

[35] Levinshtein, Michael E., Sergey L. Rumyantsev and Michael S. Shur. *Properties of Advanced Semiconductor Materials: GaN, AIN, InN, BN, SiC, SiGe*. John Wiley and Sons, 2001.

[36] Michael Kunzer. LED lamps: less energy, more light. *Fraunhofer Research News*, (March, 2014), 2014.

[37] Shuji Nakamura. GaN Growth Using GaN Buffer Layer. *Japanese Journal of Applied Physics*, 30(Part 2, No. 10A):L1705–L1707, October 1991.

[38] Shuji Nakamura, Takashi Mukai, and Masayuki Senoh. High-Power GaN P-N Junction Blue-Light-Emitting Diodes. *Japanese Journal of Applied Physics*, 30 (Part 2, No. 12A):L1998–L2001, December 1991.

[39] Jamie Fox. LED Supply and Demand Market Tracker - Q2 2014. *LED Supply and Demand Market Tracker*, 2014.

[40] David Shiller. Beyond LED: The laser vs. LED. *Enlightenment Magazine*, 2014.

[41] S. B. Nam, D. C. Reynolds, C. W. Litton, R. J. Almassy, and T. C. Collins. Free-exciton energy spectrum in GaAs. *Physical Review B*, 13(2):761–767, January 1976.

[42] S. Chichibu, T. Azuhata, T. Sota, and S. Nakamura. Spontaneous emission of localized excitons in InGaN single and multiquantum well structures. *Applied Physics Letters*, 69(27):4188, December 1996.

[43] Jun-Jie Shi. Exciton states and interband optical transitions in InGaN quantum dots. *Solid State Communications*, 124(9):341–345, November 2002.

[44] P Michler, A Kiraz, C Becher, W V Schoenfeld, P M Petroff, L Zhang, E Hu, and A Imamoglu. A quantum dot single-photon turnstile device. *Science (New York, N.Y.)*, 290(5500):2282–5, December 2000.

[45] S Kako, C Santori, and K Hoshino. A gallium nitride single-photon source operating at 200 K. *Nature materials*, 2006.

[46] MJ Holmes, K Choi, S Kako, M Arita, and Y Arakawa. Room-temperature triggered single photon emission from a III-nitride site-controlled nanowire quantum dot. *Nano letters*, 2014.

[47] S Kako, M Holmes, and S Sergent. Single-photon emission from cubic GaN quantum dots. *Applied Physics ...*, 2014.

[48] T G Tiecke, J D Thompson, N P de Leon, L R Liu, V Vuletić, and M D Lukin. Nanophotonic quantum phase switch with a single atom. *Nature*, 508(7495):241–4, April 2014.

[49] C. Monroe, R. Raussendorf, A. Ruthven, K. R. Brown, P. Maunz, L.-M. Duan, and J. Kim. Large-scale modular quantum-computer architecture with atomic memory and photonic interconnects. *Physical Review A*, 89(2):022317, February 2014.

[50] E Peter, P Senellart, D Martrou, and A Lemaître. Exciton-photon strong-coupling regime for a single quantum dot embedded in a microcavity. *Physical review ...*, 2005.

[51] JP Reithmaier, G Sk, A Löffler, and C Hofmann. Strong coupling in a single quantum dotsemiconductor microcavity system. *Nature*, 2004.

[52] BPL Reid, C Kocher, and T Zhu. Observations of Rabi oscillations in a non-polar InGaN quantum dot. *Applied Physics ...*, 2014.

[53] A Wallraff, D I Schuster, A Blais, L Frunzio, R-S Huang, J Majer, S Kumar, S M Girvin, and R J Schoelkopf. Strong coupling of a single photon to a superconducting qubit using circuit quantum electrodynamics. *Nature*, 431(7005):162–7, September 2004.

[54] D Leibfried, B DeMarco, V Meyer, D Lucas, M Barrett, J Britton, W M Itano, B Jelenković, C Langer, T Rosenband, and D J Wineland. Experimental demonstration of a robust, high-fidelity geometric two ion-qubit phase gate. *Nature*, 422 (6930):412–5, March 2003.

[55] Thomas Volz, Andreas Reinhard, Martin Winger, Antonio Badolato, Kevin J. Hennessy, Evelyn L. Hu, and Ataç Imamolu. Ultrafast all-optical switching by single photons. *Nature Photonics*, 6(9):607–611, August 2012.

[56] I. Yonenaga. Thermo-mechanical stability of wide-bandgap semiconductors: high temperature hardness of SiC, AlN, GaN, ZnO and ZnSe. *Physica B: Condensed Matter*, 308-310:1150–1152, December 2001.

[57] M. D. Drory, J. W. Ager, T. Suski, I. Grzegory, and S. Porowski. Hardness and fracture toughness of bulk single crystal gallium nitride. *Applied Physics Letters*, 69(26):4044, December 1996.

[58] Alexey Kavokin, Guillaume Malpuech, and Fabrice P. Laussy. Polariton laser and polariton superfluidity in microcavities. *Physics Letters A*, 306(4):187–199, January 2003.

[59] Christian Schneider, Arash Rahimi-Iman, Na Young Kim, Julian Fischer, Ivan G Savenko, Matthias Amthor, Matthias Lermer, Adriana Wolf, Lukas Worschech, Vladimir D Kulakovskii, Ivan A Shelykh, Martin Kamp, Stephan Reitzenstein, Alfred Forchel, Yoshihisa Yamamoto, and Sven Höfling. An electrically pumped polariton laser. *Nature*, 497(7449):348–52, May 2013.

[60] L. Sapienza, A. Vasanelli, R. Colombelli, C. Ciuti, Y. Chassagneux, C. Manquest, U. Gennser, and C. Sirtori. Electrically Injected Cavity Polaritons. *Physical Review Letters*, 100(13):136806, April 2008.

[61] Pallab Bhattacharya, Bo Xiao, Ayan Das, Sishir Bhowmick, and Junseok Heo. Solid State Electrically Injected Exciton-Polariton Laser. *Physical Review Letters*, 110(20):206403, May 2013.

[62] Lucio Andreani, Giovanna Panzarini, and Jean-Michel Gérard. Strong-coupling regime for quantum boxes in pillar microcavities: Theory. *Physical Review B*, 60 (19):13276–13279, November 1999.

[63] G. pt Hooft, W. van der Poel, L. Molenkamp, and C. Foxon. Giant oscillator strength of free excitons in GaAs. *Physical Review B*, 35(15):8281–8284, May 1987.

[64] M. Glauser, G. Rossbach, G. Cosendey, J. Levrat, M. Cobet, J.-F. Carlin, J. Besbas, M. Gallart, P. Gilliot, R. Butté, and N. Grandjean. Investigation of InGaN/-GaN quantum wells for polariton laser diodes. *physica status solidi (c)*, 9(5): 1325–1329, May 2012.

[65] Daniele Bajoni, Pascale Senellart, Esther Wertz, Isabelle Sagnes, Audrey Miard, Aristide Lemaître, and Jacqueline Bloch. Polariton Laser Using Single Micropillar GaAs-GaAlAs Semiconductor Cavities. *Physical Review Letters*, 100(4):047401, January 2008.

[66] Giovanna Panzarini and Lucio Andreani. Quantum theory of exciton polaritons in cylindrical semiconductor microcavities. *Physical Review B*, 60(24):16799–16806, December 1999.

[67] M Nomura, N Kumagai, S Iwamoto, Y Ota, and Y Arakawa. Laser oscillation in a strongly coupled single-quantum-dotnanocavity system. *Nature Physics*, 2010.

[68] Mathew C. Schmidt, Kwang-Choong Kim, Robert M. Farrell, Daniel F. Feezell, Daniel A. Cohen, Makoto Saito, Kenji Fujito, James S. Speck, Steven P. DenBaars, and Shuji Nakamura. Demonstration of Nonpolar m -Plane InGaN/GaN Laser Diodes. *Japanese Journal of Applied Physics*, 46(No. 9):L190–L191, February 2007.

[69] M Kneissl, J Rass, L Schade, and UT Schwarz. Growth and Optical Properties of GaN-Based Non-and Semipolar LEDs. *III-Nitride Based Light Emitting ...*, 2013.

[70] M. Burger, M. Ruth, S. Declair, J. Forstner, C. Meier, and D. J. As. Whispering gallery modes in zinc-blende AlN microdisks containing non-polar GaN quantum dots. *Applied Physics Letters*, 102(8):081105, February 2013.

[71] RM Farrell, PS Hsu, and DA Haeger. Low-threshold-current-density AlGaN-cladding-free m-plane InGaN/GaN laser diodes. *Applied Physics ...*, 2010.

[72] C Holder and D Feezell. Demonstration of nonpolar GaN-based vertical-cavity surface-emitting lasers. *.... of SPIE Vol*, 2013.

[73] Tongtong Zhu, Fabrice Oehler, Benjamin P. L. Reid, Robert M. Emery, Robert A. Taylor, Menno J. Kappers, and Rachel A. Oliver. Non-polar (11-20) InGaN quantum dots with short exciton lifetimes grown by metal-organic vapor phase epitaxy. *Applied Physics Letters*, 102(25):251905, June 2013.

[74] AF Jarjour, RA Oliver, and A Tahraoui. Control of the oscillator strength of the exciton in a single InGaN-GaN quantum dot. *Physical review ...*, 2007.

[75] J. Dorsaz, H.-J. Buhlmann, J.-F. Carlin, N. Grandjean, and M. Ilegems. Selective oxidation of AlInN layers for current confinement in IIInitride devices. *Applied Physics Letters*, 87(7):072102, August 2005.

[76] R Butté, J-F Carlin, E Feltin, M Gonschorek, S Nicolay, G Christmann, D Simeonov, A Castiglia, J Dorsaz, H J Buehlmann, S Christopoulos, G Baldassarri Höger von Hög, A J D Grundy, M Mosca, C Pinquier, M A Py, F Demangeot, J Frandon, P G Lagoudakis, J J Baumberg, and N Grandjean. Current status of AlInN layers lattice-matched to GaN for photonics and electronics. *Journal of Physics D: Applied Physics*, 40(20):6328–6344, October 2007.

[77] D. Neel, S. Sergent, M. Mexis, D. Sam-Giao, T. Guillet, C. Brimont, T. Bretagnon, F. Semond, B. Gayral, S. David, X. Checoury, and P. Boucaud. AlN photonic crystal nanocavities realized by epitaxial conformal growth on nanopatterned silicon substrate. *Applied Physics Letters*, 98(26):261106, June 2011.

[78] A. Rosenberg, K. Bussmann, Mijin Kim, Michael W. Carter, M. A. Mastro, Ronald T. Holm, Richard L. Henry, Joshua D. Caldwell, and Charles R. Eddy. Fabrication of GaN suspended photonic crystal membranes and resonant nanocavities on Si(111). *Journal of Vacuum Science & Technology B: Microelectronics and Nanometer Structures*, 25(3):721, April 2007.

[79] E. D. Haberer, R. Sharma, C. Meier, A. R. Stonas, S. Nakamura, S. P. DenBaars, and E. L. Hu. Free-standing, optically pumped, GaNInGaN microdisk lasers fabricated by photoelectrochemical etching. *Applied Physics Letters*, 85(22):5179, December 2004.

[80] Y Hou, P Renwick, B Liu, J Bai, and T Wang. Room temperature plasmonic lasing in a continuous wave operation mode from an InGaN/GaN single nanorod with a low threshold. *Scientific reports*, 4:5014, January 2014.

[81] T. Hino, S. Tomiya, T. Miyajima, K. Yanashima, S. Hashimoto, and M. Ikeda. Characterization of threading dislocations in GaN epitaxial layers. *Applied Physics Letters*, 76(23):3421, June 2000.

[82] X. J. Ning, F. R. Chien, P. Pirouz, J. W. Yang, and M. Asif Khan. Growth defects in GaN films on sapphire: The probable origin of threading dislocations. *Journal of Materials Research*, 11(03):580–592, January 2011.

[83] Nils G. Weimann, Lester F. Eastman, Dharanipal Doppalapudi, Hock M. Ng, and Theodore D. Moustakas. Scattering of electrons at threading dislocations in GaN. *Journal of Applied Physics*, 83(7):3656, April 1998.

[84] P Kozodoy and JP Ibbetson. Electrical characterization of GaN pn junctions with and without threading dislocations. *Applied physics ...*, 1998.

[85] T Hashimoto, F Wu, JS Speck, and S Nakamura. A GaN bulk crystal with improved structural quality grown by the ammonothermal method. *Nature materials*, 2007.

[86] C Teichert. Self-organization of nanostructures in semiconductor heteroepitaxy. *Physics Reports*, 365(5-6):335–432, August 2002.

[87] Koichi Yamaguchi, Kunihiko Yujobo, and Toshiyuki Kaizu. Stranski-Krastanov Growth of InAs Quantum Dots with Narrow Size Distribution. *Japanese Journal of Applied Physics*, 39(Part 2, No. 12A):L1245–L1248, December 2000.

[88] C.M. Reaves, V. Bressler-Hill, S. Varma, W.H. Weinberg, and S.P. DenBaars. Characterization of MOCVD-grown InP on. *Surface Science*, 326(3):209–217, March 1995.

[89] Benjamin P. L. Reid, Tongtong Zhu, Timothy J. Puchtler, Luke J. Fletcher, Christopher C. S. Chan, Rachel A. Oliver, and Robert A. Taylor. Origins of Spectral Diffusion in the Micro-Photoluminescence of Single InGaN Quantum Dots. *Japanese Journal of Applied Physics*, 52(8S):08JE01, August 2013.

[90] Justin Iveland, Lucio Martinelli, Jacques Peretti, James S. Speck, and Claude Weisbuch. Direct Measurement of Auger Electrons Emitted from a Semiconductor Light-Emitting Diode under Electrical Injection: Identification of the Dominant Mechanism for Efficiency Droop. *Physical Review Letters*, 110(17):177406, April 2013.

[91] GC Righini, Y Dumeige, and P Féron. Whispering gallery mode microresonators: fundamentals and applications. *Rivista del Nuovo ...*, 2011.

[92] J Vučković, M Lončar, H Mabuchi, and A Scherer. Design of photonic crystal microcavities for cavity QED. *Physical Review E*, 2001.

[93] Q Quan and M Loncar. Deterministic design of wavelength scale, ultra-high Q photonic crystal nanobeam cavities. *Optics express*, 2011.

[94] PB Deotare and MW McCutcheon. High quality factor photonic crystal nanobeam cavities. *Applied Physics ...*, 2009.

[95] A Tandaechanurat, S Ishida, and D Guimard. Lasing oscillation in a three-dimensional photonic crystal nanocavity with a complete bandgap. *... Photonics*, 2011.

[96] Larry A. Coldren, Scott W. Corzine, and Milan L. Mashanovitch. *Diode lasers and photonic integrated circuits*. John Wiley and Sons, vol. 218 edition, 2012.

[97] N. Vico Trivino, G. Rossbach, U. Dharanipathy, J. Levrat, A. Castiglia, J.-F. Carlin, K. A. Atlasov, R. Butte, R. Houdre, and N. Grandjean. High quality factor two dimensional GaN photonic crystal cavity membranes grown on silicon substrate. *Applied Physics Letters*, 100(7):071103, February 2012.

[98] T. Guillet, M. Mexis, S. Sergent, D. Néel, S. Rennesson, C. Brimont, T. Bretagnon, B. Gil, D. Sam-Giao, B. Gayral, F. Semond, M. Leroux, S. David, X. Checoury, and P. Boucaud. High quality factor photonic resonators for nitride quantum dots. *physica status solidi (b)*, 249(3):449–454, March 2012.

[99] Tongtong Zhu, Haitham A.R. El-Ella, Benjamin Reid, Mark J. Holmes, Robert A. Taylor, Menno J. Kappers, and Rachel A. Oliver. Growth and optical characterisation of multilayers of InGaN quantum dots. *Journal of Crystal Growth*, 338(1): 262–266, January 2012.

[100] H.A.R. El-Ella, F. Rol, D.P. Collins, M.J. Kappers, R.A. Taylor, E.L. Hu, and R.A. Oliver. InGaN super-lattice growth for fabrication of quantum dot containing microdisks. *Journal of Crystal Growth*, 321(1):113–119, April 2011.

[101] AR Stonas and T Margalith. Development of selective lateral photoelectrochemical etching of InGaN/GaN for lift-off applications. *Applied Physics ...*, 2001.

[102] P.D. Yoder, Z. Lochner, and R.D. Dupuis. Control of Quantum-Confined Stark Effect in InGaN-Based Quantum Wells. *IEEE Journal of Selected Topics in Quantum Electronics*, 15(4):1080–1091, July 2009.

[103] TT Wu, PH Weng, YJ Hou, and TC Lu. GaN-based photonic crystal surface emitting lasers with central defects. *Applied Physics Letters*, 2011.

[104] D. Simeonov, E. Feltin, A. Altoukhov, A. Castiglia, J.-F. Carlin, R. Butte, and N. Grandjean. High quality nitride based microdisks obtained via selective wet etching of AlInN sacrificial layers. *Applied Physics Letters*, 92(17):171102, April 2008.

[105] SC Hagness and D Rafizadeh. FDTD microcavity simulations: design and experimental realization of waveguide-coupled single-mode ring and whispering-gallery-mode disk resonators. *Lightwave Technology, ...*, 1997.

[106] AE Siegman. Lasers University Science Books. *Mill Valley, CA*, 1986.

[107] D. Bimberg, N. Kirstaedter, N.N. Ledentsov, Zh.I. Alferov, P.S. Kop'ev, and V.M. Ustinov. InGaAs-GaAs quantum-dot lasers. *IEEE Journal of Selected Topics in Quantum Electronics*, 3(2):196–205, April 1997.

[108] Koichi Tachibana, Takao Someya, Yasuhiko Arakawa, Ralph Werner, and Alfred Forchel. Room-temperature lasing oscillation in an InGaN self-assembled quantum dot laser. *Applied Physics Letters*, 75(17):2605, October 1999.

[109] Animesh Banerjee, Thomas Frost, Ethan Stark, and Pallab Bhattacharya. Continuous-wave operation and differential gain of InGaN/GaN quantum dot ridge waveguide lasers (λ=420nm) on c-plane GaN substrate. *Applied Physics Letters*, 101(4):041108, July 2012.

[110] Meng Zhang, Animesh Banerjee, Chi-Sen Lee, John M. Hinckley, and Pallab Bhattacharya. A InGaN/GaN quantum dot green (λ=524nm) laser. *Applied Physics Letters*, 98(22):221104, June 2011.

[111] Seongsik Chang, Nathan B. Rex, Richard K. Chang, Gabel Chong, and Louis J. Guido. Stimulated emission and lasing in whispering-gallery modes of GaN microdisk cavities. *Applied Physics Letters*, 75(2):166, July 1999.

[112] D. Young. *PhD Thesis*. PhD thesis, University of California, Santa Barbara, 2002.

[113] Justin C Johnson, Heon-Jin Choi, Kelly P Knutsen, Richard D Schaller, Peidong Yang, and Richard J Saykally. Single gallium nitride nanowire lasers. *Nature materials*, 1(2):106–10, October 2002.

[114] Chih-Yen Chen, Guang Zhu, Youfan Hu, Jeng-Wei Yu, Jinghui Song, Kai-Yuan Cheng, Lung-Han Peng, Li-Jen Chou, and Zhong Lin Wang. Gallium nitride nanowire based nanogenerators and light-emitting diodes. *ACS nano*, 6(6):5687–92, June 2012.

[115] T. Someya. Room Temperature Lasing at Blue Wavelengths in Gallium Nitride Microcavities. *Science*, 285(5435):1905–1906, September 1999.

[116] Igor Aharonovich, Alexander Woolf, Kasey J. Russell, Tongtong Zhu, Nan Niu, Menno J. Kappers, Rachel A. Oliver, and Evelyn L. Hu. Low threshold, room-temperature microdisk lasers in the blue spectral range. *Applied Physics Letters*, 103(2):021112, July 2013.

[117] P. Michler, A. Kiraz, Lidong Zhang, C. Becher, E. Hu, and A. Imamoglu. Laser emission from quantum dots in microdisk structures. *Applied Physics Letters*, 77 (2):184, July 2000.

[118] Alexander I. Nosich, Elena I. Smotrova, Svetlana V. Boriskina, Trevor M. Benson, and Phillip Sewell. Trends in microdisk laser research and linear optical modelling. *Optical and Quantum Electronics*, 39(15):1253–1272, April 2008.

[119] Toshihide Ide, Toshihiko Baba, Jun Tatebayashi, Satoshi Iwamoto, Toshihiro Nakaoka, and Yasuhiko Arakawa. Room temperature continuous wave lasing in InAs quantum-dot microdisks with air cladding. *Optics Express*, 13(5):1615, 2005.

[120] I. Krestnikov, N. Ledentsov, A. Hoffmann, D. Bimberg, A. Sakharov, W. Lundin, A. Tsatsulnikov, A. Usikov, Zh. Alferov, Yu. Musikhin, and D. Gerthsen. Quantum dot origin of luminescence in InGaN-GaN structures. *Physical Review B*, 66(15): 155310, October 2002.

[121] R. A. Oliver, F. C.-P. Massabuau, M. J. Kappers, W. A. Phillips, E. J. Thrush, C. C. Tartan, W. E. Blenkhorn, T. J. Badcock, P. Dawson, M. A. Hopkins, D. W. E. Allsopp, and C. J. Humphreys. The impact of gross well width fluctuations on the efficiency of GaN-based light emitting diodes. *Applied Physics Letters*, 103(14):141114, October 2013.

[122] Nicole K. van der Laak, Rachel A. Oliver, Menno J. Kappers, and Colin J. Humphreys. Role of gross well-width fluctuations in bright, green-emitting single InGaNGaN quantum well structures. *Applied Physics Letters*, 90(12):121911, March 2007.

[123] M Mexis, S Sergent, T Guillet, C Brimont, T Bretagnon, B Gil, F Semond, M Leroux, D Néel, S David, X Chécoury, and P Boucaud. High quality factor nitride-based optical cavities: microdisks with embedded GaN/Al(Ga)N quantum dots. *Optics letters*, 36(12):2203–5, June 2011.

[124] R.A. Oliver, A.F. Jarjour, R.A. Taylor, A. Tahraoui, Y. Zhang, M.J. Kappers, and C.J. Humphreys. Growth and assessment of InGaN quantum dots in a microcavity: A blue single photon source. *Materials Science and Engineering: B*, 147(2-3):108–113, February 2008.

[125] Yukio Narukawa, Yoichi Kawakami, Mitsuru Funato, Shizuo Fujita, Shigeo Fujita, and Shuji Nakamura. Role of self-formed InGaN quantum dots for exciton localization in the purple laser diode emitting at 420 nm. *Applied Physics Letters*, 70 (8):981, February 1997.

[126] Anas F. Jarjour, Rachel A. Oliver, and Robert A. Taylor. Nitride-based quantum dots for single photon source applications. *physica status solidi (a)*, 206(11):2510–2523, November 2009.

[127] J. Christen, D. Bimberg, A. Steckenborn, and G. Weimann. Localization induced electron-hole transition rate enhancement in GaAs quantum wells. *Applied Physics Letters*, 44(1):84, January 1984.

[128] Qimin Quan, Parag B. Deotare, and Marko Loncar. Photonic crystal nanobeam cavity strongly coupled to the feeding waveguide. *Applied Physics Letters*, 96(20): 203102, May 2010.

[129] Qimin Quan and Marko Loncar. Deterministic design of wavelength scale, ultrahigh Q photonic crystal nanobeam cavities. *Optics express*, 19(19):18529–42, September 2011.

[130] M Kuball, ES Jeon, and YK Song. Gain spectroscopy on InGaN/GaN quantum well diodes. *Applied physics . . .*, 1997.

[131] R A Oliver, S E Bennett, T Zhu, D J Beesley, M J Kappers, D W Saxey, A Cerezo, and C J Humphreys. Microstructural origins of localization in InGaN quantum wells. *Journal of Physics D: Applied Physics*, 43(35):354003, September 2010.

[132] Gunnar Bjork and Yoshihisa Yamamoto. Analysis of Semiconductor Microcavity Lasers Using Rate Equations. 27(11):2386–2396, 1991.

[133] M. Boroditsky, I. Gontijo, M. Jackson, R. Vrijen, E. Yablonovitch, T. Krauss, Chuan-Cheng Cheng, A. Scherer, R. Bhat, and M. Krames. Surface recombination measurements on IIIV candidate materials for nanostructure light-emitting diodes. *Journal of Applied Physics*, 87(7):3497, April 2000.

[134] M. Nomura, N. Kumagai, S. Iwamoto, Y. Ota, and Y. Arakawa. Laser oscillation in a strongly coupled single-quantum-dotnanocavity system. *Nature Physics*, 6(4): 279–283, February 2010.

[135] K Hennessy, A Badolato, M Winger, D Gerace, M Atatüre, S Gulde, S Fält, E L Hu, and A Imamolu. Quantum nature of a strongly coupled single quantum dot-cavity system. *Nature*, 445(7130):896–9, February 2007.

[136] Fabio Bernardini, Vincenzo Fiorentini, and David Vanderbilt. Spontaneous polarization and piezoelectric constants of III-V nitrides. *Physical Review B*, 56(16): R10024–R10027, October 1997.

[137] R.A. Oliver, M.J. Kappers, J. Sumner, R. Datta, and C.J. Humphreys. Highlighting threading dislocations in MOVPE-grown GaN using an in situ treatment with SiH4 and NH3. *Journal of Crystal Growth*, 289(2):506–514, April 2006.

[138] Qi Zhang, Yih Hong Lee, In Yee Phang, Srikanth Pedireddy, Weng Weei Tjiu, and Xing Yi Ling. Bimetallic platonic Janus nanocrystals. *Langmuir : the ACS journal of surfaces and colloids*, 29(41):12844–51, October 2013.

[139] M Khoury, A Courville, B Poulet, M Teisseire, E Beraudo, M J Rashid, E Frayssinet, B Damilano, F Semond, O Tottereau, and P Vennéguès. Imaging and counting threading dislocations in c-oriented epitaxial GaN layers. *Semiconductor Science and Technology*, 28(3):035006, March 2013.

[140] S. K. Rhode, M. K. Horton, M. J. Kappers, S. Zhang, C. J. Humphreys, R. O. Dusane, S. L. Sahonta, and M. A. Moram. Mg Doping Affects Dislocation Core Structures in GaN. *Physical Review Letters*, 111(2):025502, July 2013.

[141] O. Ambacher, W. Rieger, P. Ansmann, H. Angerer, T.D. Moustakas, and M. Stutzmann. Sub-bandgap absorption of gallium nitride determined by Photothermal Deflection Spectroscopy. *Solid State Communications*, 97(5):365–370, February 1996.

[142] Takao Miyajima, Hino Tomonori, Shigetaka Tomiya, Satake Akihiro, Eiji Tokunagat, Yasuaki Masumoto, Takahiro Maruyama, Masako Ikeya, Sin-ichi Morishima, Katsuhiro Akimoto, Katsunori Yanashima, Shigeki Hashimoto, Toshimasa Kobayashi, and Masao Ikedai. TD_recombination.pdf, 2000.

[143] Hiroki Hasegawa, Yasushi Kamimura, Keiichi Edagawa, and Ichiro Yonenaga. Dislocation-related optical absorption in plastically deformed GaN. *Journal of Applied Physics*, 102(2):026103, July 2007.

[144] J. Elsner, R. Jones, M. Heggie, P. Sitch, M. Haugk, Th. Frauenheim, S. Öberg, and P. Briddon. Deep acceptors trapped at threading-edge dislocations in GaN. *Physical Review B*, 58(19):12571–12574, November 1998.

[145] Y. Xin, E. M. James, I. Arslan, S. Sivananthan, N. D. Browning, S. J. Pennycook, F. Omnes, B. Beaumont, J-P. Faurie, and P. Gibart. Direct experimental observation of the local electronic structure at threading dislocations in metalorganic vapor phase epitaxy grown wurtzite GaN thin films. *Applied Physics Letters*, 76 (4):466, January 2000.

[146] Matthew Borselli, Thomas J. Johnson, and Oskar Painter. Beyond the Rayleigh scattering limit in high-Q silicon microdisks: theory and experiment. *Optics Express*, 13(5):1515, 2005.

[147] S. L. McCall, A. F. J. Levi, R. E. Slusher, S. J. Pearton, and R. A. Logan. Whispering-gallery mode microdisk lasers. *Applied Physics Letters*, 60(3):289, January 1992.

[148] R. E. Slusher, A. F. J. Levi, U. Mohideen, S. L. McCall, S. J. Pearton, and R. A. Logan. Threshold characteristics of semiconductor microdisk lasers. *Applied Physics Letters*, 63(10):1310, September 1993.

[149] Jae-Soong Lee, Joonhee Lee, Sunghwan Kim, and Heonsu Jeon. Fabrication of reflective GaN mesa sidewalls for the application to high extraction efficiency LEDs. *physica status solidi (c)*, 4(7):2625–2628, June 2007.

[150] R. J. Shul, L. Zhang, A. G. Baca, C. G. Willison, J. Han, S. J. Pearton, and F. Ren. Inductively coupled plasma-induced etch damage of GaN p-n junctions. *Journal of Vacuum Science & Technology A: Vacuum, Surfaces, and Films*, 18(4): 1139, July 2000.

[151] D. Simeonov, E. Feltin, H.-J. Buhlmann, T. Zhu, A. Castiglia, M. Mosca, J.-F. Carlin, R. Butte, and N. Grandjean. Blue lasing at room temperature in high quality factor GaNAlInN microdisks with InGaN quantum wells. *Applied Physics Letters*, 90(6):061106, February 2007.

[152] G. Yu, G. Wang, H. Ishikawa, M. Umeno, T. Soga, T. Egawa, J. Watanabe, and T. Jimbo. Optical properties of wurtzite structure GaN on sapphire around fundamental absorption edge (0.784.77 eV) by spectroscopic ellipsometry and the optical transmission method. *Applied Physics Letters*, 70(24):3209, June 1997.

[153] Matthew Borselli, Kartik Srinivasan, Paul E. Barclay, and Oskar Painter. Rayleigh scattering, mode coupling, and optical loss in silicon microdisks. *Applied Physics Letters*, 85(17):3693, October 2004.

[154] Kartik Srinivasan and Oskar Painter. Linear and nonlinear optical spectroscopy of a strongly coupled microdisk-quantum dot system. *Nature*, 450(7171):862–5, December 2007.

[155] Martin A. Green. Self-consistent optical parameters of intrinsic silicon at 300K including temperature coefficients. *Solar Energy Materials and Solar Cells*, 92 (11):1305–1310, November 2008.

[156] M. Sturge. Optical Absorption of Gallium Arsenide between 0.6 and 2.75 eV. *Physical Review*, 127(3):768–773, August 1962.

[157] Timothy E. Dimmick, George Kakarantzas, Timothy A. Birks, and Philip St. J. Russell. Carbon Dioxide Laser Fabrication of Fused-Fiber Couplers and Tapers. *Applied Optics*, 38(33):6845, November 1999.

[158] Jonathan M. Ward, Danny G. OShea, Brian J. Shortt, Michael J. Morrissey, Kieran Deasy, and Sile G. Nic Chormaic. Heat-and-pull rig for fiber taper fabrication. *Review of Scientific Instruments*, 77(8):083105, August 2006.

[159] T. Alder, A. Stohr, R. Heinzelmann, and D. Jager. High-efficiency fiber-to-chip coupling using low-loss tapered single-mode fiber. *IEEE Photonics Technology Letters*, 12(8):1016–1018, August 2000.

[160] Joel Villatoro, David Monzón-Hernández, and Efrain Mejía. Fabrication and Modeling of Uniform-Waist Single-Mode Tapered Optical Fiber Sensors. *Applied Optics*, 42(13):2278, 2003.

[161] Paul E. Barclay, Kartik Srinivasan, and Oskar Painter. Nonlinear response of silicon photonic crystal micresonators excited via an integrated waveguide and fiber taper. *Optics Express*, 13(3):801, 2005.